PERFORMANCE LOSSES IN ADDITIVELY MANUFACTURED LOW THRUST NOZZLES

THESIS

Christopher D. Tommila, Captain, USAF

AFIT-ENY-MS-17-M-295

DEPARTMENT OF THE AIR FORCE
AIR UNIVERSITY

AIR FORCE INSTITUTE OF TECHNOLOGY

Wright-Patterson Air Force Base, Ohio

AFIT-ENY-MS-17-M-295

PERFORMANCE LOSSES IN ADDITIVELY MANUFACTURED LOW THRUST NOZZLES

THESIS

Presented to the Faculty

Department of Aeronautics and Astronautics

Graduate School of Engineering and Management

Air Force Institute of Technology

Air University

Air Education and Training Command

In Partial Fulfillment of the Requirements for the

Degree of Master of Science in Astronautical Engineering

Christopher D. Tommila, BS

Captain, USAF

March 2017

AFIT-ENY-MS-17-M-295

PERFORMANCE LOSSES IN ADDITIVELY MANUFACTURED LOW THRUST NOZZLES

Christopher D. Tommila, BS

Captain, USAF

Committee Membership:

Dr. Carl Hartsfield
Chair

Dr. William Hargus
Member

Dr. Mark Reeder
Member

Abstract

The goal of this research is to evaluate, both analytically and experimentally, the suitability of additive manufacturing in the production of small scale thruster nozzles for low thrust orbital propulsion applications. Current high temperature metallic additive manufacturing processes, like Direct Metal Laser Sintering, typically result in untreated part surfaces with higher roughness than traditional machining processes. For large scale rocket applications, nozzle wall roughness, and the associated boundary layer effects, may safely be ignored. However, in nozzles with throat diameters on the order of ten-thousandths of an inch, any viscous effects originating at the nozzle walls must be considered. Scaling laws suggest that, even at the low flow Reynolds numbers exhibited in low thrust applications, the effects of viscous losses at the nozzle walls are affected by an increase in nozzle surface roughness. The first phase of this research focuses on the design and implementation of an analytic model to predict losses in thrust coefficient due to viscous effects. During the second phase, a variety of nozzle configurations are tested in a laboratory environment to determine the accuracy of the analytic model and to identify additional modes of performance loss associated with increased surface roughness.

Acknowledgments

I would like to thank my research advisor, Dr. Carl Hartsfield, for his constant guidance and patience throughout this research. I'd especially like to thank him for working with me to create a topic and experiment that I am truly passionate about exploring. I am also indebted to Mr. Joshua Dewitt for the countless hours he spent lending his expertise and helping hand in the laboratory. This research would now have been possible without these individuals.

Additionally, I'd like to acknowledge the efforts of Mr. Jamie Smith, Mr. Randall Sharp, Mr. Phil Smith and the machine shop personnel of AFIT for providing invaluable help and hours of hard work at various stages of this experiment. I'd also like to thank Mr. James Deneault and AFRL for providing us with the opportunity to utilize their incredible resources and personnel.

Finally, I'd like to thank my wife for her unwavering support in all of my endeavors and for reminding me of what's truly important in trying times.

Christopher D. Tommila

Table of Contents

Page

List of Figures

Page

List of Tables

Page

List of Symbols

A_2	Exit Area
A_D	Area Change Coefficient
C_F	Thrust Coefficient
F	Thrust
I_{sp}	Specific Impulse
M	Mach Number
P_0	Stagnation Pressure
P_2	Exit Pressure
P_3	Ambient Pressure
P_{ch}	Static Chamber Pressure
P_T	Hydraulic Perimeter (Throat)
Re	Reynolds Number
T_0	Stagnation Temperature
T_{ch}	Chamber Temperature
f	Fanning Friction Factor
f_D	Darcy Friction Factor
g_0	Gravitational Constant
$\dot{m}$	Mass Flow
v_2	Exit Velocity
α	Nozzle Divergence Half Angle
γ	Ratio of Specific Heats

ε	Expansion Ratio
ϵ	Absolute Roughness
θ	Divergence Half Angle (alternative)
μ	Viscosity
τ	Shear Stress

List of Abbreviations

DMLS	Direct Metal Laser Sintering
EDM	Electrical Discharge Machining
NPT	National Pipe Threaded
ODE	Ordinary Differential Equation
SEM	Scanning Electron Microscope
STP	Standard Temperature and Pressure

PERFORMANCE LOSSES IN ADDITIVELY MANUFACTURED LOW THRUST NOZZLES

I. Introduction

1.1 Motivation

Low thrust propulsion systems have been incorporated in spacecraft design to accomplish attitude control and orbital maintenance maneuvers since the early days of spaceflight. Even in large spacecraft, care must be taken in the sizing of these thrusters because of the accuracy, precision, and scale of these applications. Oftentimes, these maneuvers require the generation of thrust on the order of 1 Newton or less. The rise in popularity of microsatellites, including CubeSats, has further increased the demand for smaller, lighter, more efficient propulsion techniques [1]. According to a 1999 study by the Air Force Research Laboratory (AFRL), "constellations or platoons of microspacecraft […] lend themselves to increased survivability, flexibility and functionality" [1]. Microsatellites offer clear advantages, but mass, volume and power are at a premium and thrust maneuvers must be accomplished on an even smaller, more accurate scale.

A wide variety of propulsion techniques have been developed to fill these low thrust roles. Many, including electrothermal thrusters, operate similarly to larger rocket engines by expanding hot gas through a converging-diverging nozzle to convert the potential energy of the gas into kinetic energy [2]. Unlike their larger counterparts, the high gas temperatures and low thrust levels typical of electrothermal thrusters result in low Reynolds number flow dominated by viscous forces [3]. In 1962, NASA began

experimental studies of thrusters in this flow regime to quantify the impacts of these viscous forces on thruster performance [4]. A second round of studies was accomplished in 1987 to improve understanding of low Reynolds number flow through micro-nozzles [5], [6]. In addition to the performance impacts explored by NASA, incorporation of these nozzles has been further complicated by traditional manufacturing processes that are often time consuming and costly.

Advances in modern manufacturing technology, including additive manufacturing, have demonstrated potential to significantly impact the production and integration of microsatellite propulsion systems. Additive manufacturing processes, known colloquially as 3-D printing, build parts layer by layer based on a computer model, allowing them to be manufactured rapidly while conserving material and minimizing human involvement in the manufacturing process. Direct Metal Laser Sintering (DMLS) is an additive manufacturing process that has matured steadily since its initial rise at the turn of the 21st century and can now print high temperature metallic alloys, including high-nickel superalloys such as Inconel and Hastelloy [7]. Therefore, it is a prime candidate for use in space propulsion applications. Researchers have already proven the feasibility of incorporating DMLS to ease the manufacturing process of microsatellite components, including propulsion systems [8].

1.2 Problem Statement

Additive manufacturing processes have the potential to alter the landscape of microsatellite design and manufacturing. However, one of the acknowledged faults of the DMLS process is that it results in higher untreated part surface roughness than

traditional machining operations [7]. This increased roughness may lead to an increase in viscous performance losses in micro-nozzles because, with throat diameters on the order of thousandths of an inch, the height of surface irregularities may be significant in comparison to flow diameter [9]. In 1987, NASA acknowledged the potential negative performance impacts of increased roughness of the flow surface in micro-nozzles [6]. However, those studies stopped short of investigating this relationship. The goal of this research is to experimentally quantify the impact of increased surface roughness on the performance of low thrust nozzles at throat Reynolds numbers between 500 and 10000.

1.3 Research Methodology

For this research, micro-propulsion nozzles were manufactured out of high temperature alloys using both traditional machining and DMLS processes. The machined nozzles were originally designed to match theoretically optimal expansion ratios as defined in the initial NASA research [4]. However, inability to meet manufacturing tolerances resulted in lower than expected expansion ratios. Additional nozzles were manufactured using the DMLS process to evaluate a larger range of Reynolds numbers and include geometries previously unattainable through conventional machining processes.

The experiment is conducted in a vacuum chamber where monatomic (helium), diatomic (nitrogen) and triatomic (carbon dioxide) gases are heated and expanded through the nozzle to simulate operational conditions on orbit. The volumetric flow rate and temperatures of the gases are varied to achieve a range of throat Reynolds numbers between 500 and 10000. Thrust, stagnation pressure and ambient pressure are measured

directly and used to calculate the thrust coefficient for each configuration. Following testing, multiple DMLS nozzles were sectioned and evaluated using a laser scanning microscope to quantify the surface roughness of the interior surface.

1.4 Research Objectives

Additive manufacturing processes, including DMLS, are becoming increasingly common in spacecraft manufacturing, especially in the microsatellite community. It is necessary to understand the impacts of surface roughness associated with this process prior to adaptation for micro-nozzle manufacturing. The following research objectives are intended to further this understanding:

1. Experimentally measure thrust and stagnation pressure of additively manufactured and machined micro-nozzles, with controlled mass flow.

2. Calculate thrust coefficients of both nozzle configurations using experimental measurements.

3. Develop an analytic model to predict the effects of surface roughness on viscous losses during thruster operation.

4. Compare experimental results to the analytic model to determine whether traditional viscous loss theory alone can accurately predict performance losses in machined and DMLS nozzles.

5. Compare thrust coefficients of additively manufactured nozzles against those of the machined nozzles to quantify performance impacts caused by surface roughness.

1.5 Assumptions, Limitations and Scope

Although performance losses can be attributed to both heat transfer and frictional effects, it is assumed that these mechanisms cannot be studied separately in this experiment because the gas must be heated to study the range of Reynolds numbers desired. This assumption was also made in the earliest NASA investigations [4]. The

goal of this research is to study the combined impact of the loss mechanisms. Identifying the contributions of the individual components is beyond the scope of the experiment.

The scope of the research is limited by both the heating and volumetric flow rates of the gases. Heating is limited by the power available from the power supply and the rated output of the heaters and volumetric flow rate is limited by the need to maintain near vacuum pressure in the chamber [10]. These factors directly impact the Reynolds numbers that can be achieved and the nozzle sizes that can be studied.

1.6 Preview

This section provides a summary of the remaining chapters. Chapter II is the Literature Review and summarizes the relevant theory and previous research in this area. Chapter III is the Methodology. It outlines the procedures and processes of the experiment. Chapter IV details the results of the experiment and includes analysis of all data collected. Chapter V lays out the conclusions of this research and includes recommendations for continued research.

II. Literature Review

Many forms of micro-propulsion are small scaled versions of rocket motors described by the ideal rocket equations. Therefore, investigation of the performance of micro-nozzles begins with the equations of an ideal rocket. These equations assume isentropic flow, or flow that is both adiabatic and frictionless [11]. However, these key assumptions are invalid at the mass flow rates and temperatures characteristic of low thrust propulsion devices. These conditions create low Reynolds number flow that is appreciably affected, if not dominated, by viscous forces forming in the laminar boundary layer of the flow field [4]. Additive manufacturing technologies, including DMLS, increase the surface roughness of the nozzle at the flow boundary and theoretically increase the magnitude of these viscous losses in turbulent flows. This research investigates the effects of surface roughness on viscous losses in compressible, low Reynolds number flow through a micro-nozzle. Furthermore, this research aims to quantify the performance impacts caused by these viscous loss terms.

2.1 Equations of an Ideal Rocket

Micro-thrusters are rocket motors and, as such, produce thrust by thermally expanding a propellant gas through a nozzle. The expansion of the propellant in these nozzles converts the thermal energy of the gas into kinetic energy as the exhaust gases are accelerated to high velocities at the exit plane of the nozzle [12]. This is commonly referred to as the momentum term of the thrust equation. This change in momentum of the exhaust particles coupled with pressure difference between the exhaust gas and the ambient atmosphere, known as the pressure term, produce the thrust required to propel

the spacecraft [2]. Figure 1 depicts a cross-sectional view of a converging-diverging micro-nozzle manufactured for this research.

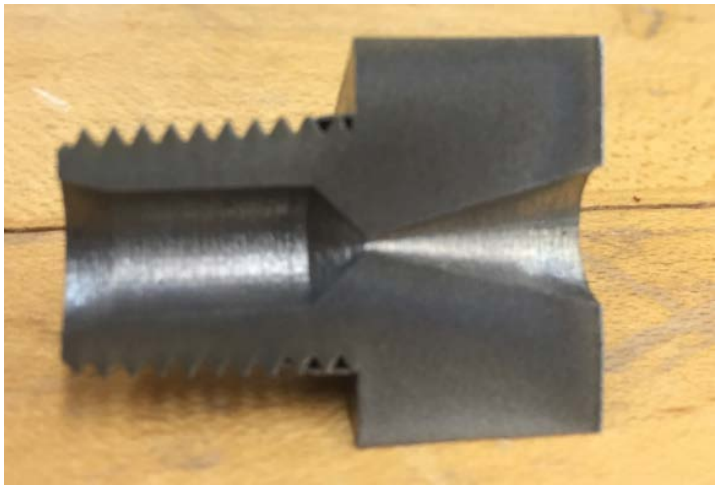

Figure 1: Conical Micro-Nozzle

Mathematically, this relationship between thrust, change in exhaust matter momentum and pressure gradient at the exit is represented in Equation 1 [2]. Furthermore, in the case of a rocket operating in an ambient vacuum, such as space, the thrust equation simplifies to the expression in Equation 2.

$$F = \dot{m}v_2 + (p_2 - p_3)A_2 \quad (1)$$

$$F = \dot{m}v_2 + p_2A_2 \quad (2)$$

While thrust is expressed in units of mass times acceleration, it is often desirable to express a non-dimensional quantity instead. The thrust coefficient is non-dimensional and, more importantly, is a convenient performance measure that can be determined experimentally, given only the measured thrust, throat area, and chamber pressure of the rocket [2] [3] [4]. Equation 3 expresses this relationship mathematically [2].

$$C_F = \frac{F}{A_tP_1} \quad (3)$$

The thrust coefficient can also be calculated analytically for an ideal rocket, assuming isentropic flow, using the ratio of specific heats of the propellant gas and the known geometry of the nozzle. This alternate expression allows for comparison between the theoretical and measured quantity and is expressed in Equation 4.

$$C_F = \sqrt{\frac{2\gamma^2}{\gamma-1}\left(\frac{2}{\gamma+1}\right)^{\frac{\gamma+1}{\gamma-1}}\left[1-\left(\frac{p_2}{p_1}\right)^{\frac{\gamma-1}{\gamma}}\right]} + \frac{p_2-p_3}{p_1}\frac{A_2}{A_t} \tag{4}$$

Thrust and thrust coefficient both illustrate the amount of force the rocket transfers to the spacecraft or test apparatus. The specific impulse, or I_{sp}, indicates how economically this force is produced; it is an important performance parameter of the rocket. While not technically an efficiency, the I_{sp} expresses the relationship between the thrust a rocket produces and the mass flow of propellant gas required to produce that thrust. Therefore, a higher I_{sp} for a given mass flow indicates that the rocket uses that propellant mass to greater effect. It is defined in Equation 5 as a function of the total thrust, gravitational constant, and the mass flow rate of the propellant through the nozzle [2]. The final simplification of Equation 5 is a common representation that assumes constant thrust and mass over the operation of the thruster. Conveniently, this expression is also a method of calculating the specific impulse directly when the thrust is measured experimentally and the mass flow is an experimental control.

$$I_{sp} = \frac{\int_0^t F dt}{g_0 \int \dot{m}\, dt} = \frac{F}{g_0 \dot{m}} \tag{5}$$

2.2 Ideal Rocket Limitations for Micro-Nozzles

While the ideal rocket equations form a starting point for the evaluation of thrusters and are often sufficient in describing the behavior of large-scale rocket motors, they are limited by a series of assumptions that are problematic for micro-thruster flow conditions. Most importantly, these ideal rocket equations assume the following about the flow of a homogeneous gas through a nozzle [2]:

1. The flow through the nozzle is adiabatic; no heat is transferred through the walls of the nozzle.
2. Boundary layer effects are marginal in comparison to the bulk flow of the propulsive gases through the nozzle.
3. The nozzle walls are frictionless or near frictionless.
4. Flow within the nozzle is free of any shock waves.

It has been shown both experimentally and analytically that these assumptions are invalid in the case of micro-scale rockets. First, per the NASA study performed by Spisz, "for low propellant flow rates, heat-transfer losses to the nozzle walls can be a significant portion of the total thermal energy available for conversion to kinetic energy" [4]. The propellant flow rates evaluated in the NASA study were on the order of 10^{-5} kilograms per second and are similar in scale to those evaluated in this study.

Because an adiabatic system does not lose heat to its surroundings during operation, and all energy in the form of heat is available for conversion to kinetic energy, the NASA study invalidates the adiabatic flow assumption when evaluating low Reynolds number thrusters [13]. However, this research must assume adiabatic flow due to experimental constraints. Thermal sensitivity of measurement instruments prevents heat soaking of the nozzles prior to testing to resolve thermal gradients in the nozzle,

thereby eliminating heat transfer to the nozzle walls. Additionally, room temperature gas cannot be used because of the risk of condensed phase flow in the nozzle. Therefore, flow conditions must be calculated under the assumption that heat transfer effects are negligible. Fortunately, the relatively low flow temperatures in this experiment and the low thermal conductivity of the nickel alloy investigated minimizes the impact of non-adiabatic behavior in this research.

The second assumption, that the behavior of the boundary layer has negligible effects on the behavior of the bulk flow of the propulsive gas through the nozzle, has been thoroughly rejected in micro-flow conditions. According to Murch, "the high temperatures and low thrust levels characteristic of these thrusters often result in low Reynolds number nozzle flow" [3]. In an analytical study published in 1962, Williams established that, when evaluating low Reynolds number compressible flow through a closed channel, boundary layer theory begins to break down. In this case, viscous effects are no longer constrained to the outer edges of the flow field [14]. Grisnik later showed experimentally that at sufficiently low Reynolds numbers, viscous boundary layer conditions likely fill the entire cross section of the nozzle [5]. For comparison, Figure 2 depicts flow conditions in which the boundary layer is constrained to a differential distance from the nozzle walls.

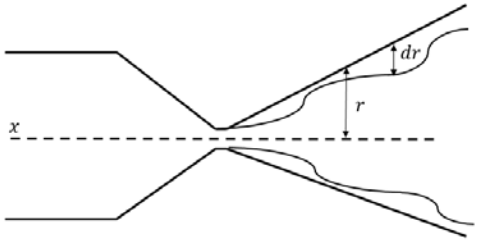

Figure 2: Typical Boundary Layer Configuration

The assumption that friction at the walls of the nozzle is negligible is closely related to the boundary layer theory (and will be investigated exhaustively in Section 2.6). In larger rocket nozzles, the surface roughness is minute in comparison to the hydraulic diameter of the exhaust gases within the nozzle. Therefore, its contribution to the overall flow behavior is considered negligible.

Finally, the ideal rocket equations assume that no shock waves exist within the nozzle itself [2]. However, work by Krishnamurty suggests that, for small converging-diverging nozzles with high relative roughness, shock waves not only form, but reflect, within the diverging area of the nozzle [15]. This suggests that the final assumption may be invalid for the additively manufactured nozzles investigated in this research.

2.3 Low Reynolds Number Flow

As asserted, assumptions in the ideal rocket equations prove to be problematic when considering the flow conditions in micro-nozzles. However, before investigating these shortcomings, it is necessary to introduce the concept of low Reynolds number flow. The Reynolds number of a flow is a ratio of the momentum forces to viscous

forces within a flow field [12]. Therefore, a low Reynolds number indicates that viscous forces contribute significantly to the behavior of the flow field, while high Reynolds numbers indicate the inverse. This study adopts the convention of Spisz, Grisnik and Whalen in defining low Reynolds number flow as flow in which this ratio falls below 10,000 at the throat of the nozzle [4] [5] [6]. This relationship between momentum and viscous forces is represented mathematically as a function of the mass flow of the propulsive gas, the flow diameter, and the viscosity of the gas in Equation 6 [6]. The equation is also simplified to a relationship between gas density, velocity at the throat, throat diameter, and viscosity:

$$Re_t = \frac{4\dot{m}}{\pi\mu d_t} = \frac{4\rho v_t A_t}{\pi\mu d_t} = \frac{\rho v_t d_t}{\mu} \tag{6}$$

Low Reynolds number flow is common in micro-thrusters on the scales investigated in this study. This is demonstrated mathematically using Equation 6 above to express proportionality between the flow Reynolds number, the temperature of the exhaust gas, and the diameter of the nozzle throat.

The density, velocity, and viscosity of the gas in Equation 6 are all dependent upon temperature. The independent proportionality of each must be established prior to determining their approximate net proportionality. According to the Ideal Gas Law, the density of a gas may be expressed as follows.

$$\rho = \frac{P}{RT} \tag{7}$$

Equation 7 shows that the density in an ideal gas is inversely proportional to the temperature of the gas. Next, the definition of the Mach number at the throat establishes

that the local velocity is proportional to the square root of the temperature of the propellant gas at the nozzle throat [2].

$$M = \frac{v}{\sqrt{\gamma R T}} \tag{8}$$

Per Spisz, the viscosity of hydrogen is inversely proportional to temperature raised to the two thirds power [4]. This assumption is sufficient for the purposes of establishing approximate proportionality for all three gases in this study. Combining this relationship with those established in Equations 7 and 8 yields the following approximation of the cumulative dependence of Reynolds number on temperature:

$$Re \propto \frac{1}{T} \times \frac{T^{\frac{1}{2}}}{1} \times \frac{1}{T^{\frac{2}{3}}} \approx \frac{1}{T} \tag{9}$$

Equations 6 and 9 combine to establish proportionality between the throat Reynolds number, gas temperature, and throat diameter as shown in Equation 10. Increasing the temperature of the gas or decreasing the throat diameter serves to decrease the Reynolds number of the flow.

$$Re \propto \frac{d_t}{T} \tag{10}$$

According to the proportionality established in Equation 10, micro-thrusters are especially susceptible to low Reynolds number flow. The throat diameters of the nozzles investigated in this study are between 0.015 and 0.035-inches. The high operating temperatures characteristic of electro-thermal thrusters combine with these throat diameters to reduce the Reynolds number [6].

2.4 Viscous Losses in Micro-Nozzle Flow

The low Reynolds number flow investigated in Section 2.3 leads to significant performance losses in micro-thrusters. These losses can be attributed to both heat transfer through the nozzle walls and viscous effects originating at the nozzle wall [4]. This research will focus on the viscous loss terms.

According to Spisz, the loss in thrust attributable to viscous effects in a micro-nozzle is determined analytically by integrating the local shear stress τ over the surface area of the diverging section of the nozzle represented in terms of the nozzle divergence half angle α and the nozzle area ratio as shown in Equation 11 [4].

$$F_v = \int_1^{\frac{A_e}{A_{th}}} \frac{\tau A_{th}}{tan\alpha} d\left(\frac{A}{A_{th}}\right) \tag{11}$$

Alternatively, the losses due to viscous drag can be characterized as an associated loss in thrust coefficient of the nozzle. Although this representation of the losses is laborious, it can be solved analytically given experimentally measurable quantities and approximations from the ideal rocket equations. The mathematical relationships for these viscous losses were derived by Spisz and are represented in Equations 12 through 15 [4].

$$C_{F_v} = \frac{0.64 f_0}{(Re_{th} tan\alpha)^{\frac{1}{2}}} \int_1^{\frac{A_e}{A_{th}}} f_1 f_2 d\left(\frac{A}{A_{th}}\right) \tag{12}$$

$$f_0 = \gamma \left(\frac{\left(\frac{\mu_w}{\mu_{th}}\left(\frac{\rho_0}{\rho_{th}}\right)\sqrt{\frac{T_{th}}{T_0}}\right)}{\frac{2T_w}{T_0}} \right)^{\frac{1}{2}} \tag{13}$$

$$f_1 = \left(\sqrt{\frac{A}{A_{th}}} - 1 \right)^{-\frac{1}{2}} \tag{14}$$

$$f_2 = M^{1.5} \left(\frac{T}{T_0} \right)^{\frac{5\gamma-3}{4(\gamma-1)}} \tag{15}$$

Although these equations form a basis for prediction of the viscous losses in micro-nozzles, they fail to consider the effects of nozzle surface roughness on the magnitudes of these losses. In subsequent research by NASA, Whalen suggested that additional analysis be performed to quantify these effects [6]. Therefore, this study establishes an alternate method of calculating viscous loss terms that includes a roughness contribution. This consideration becomes more important when nozzles are manufactured using additive manufacturing techniques that inherently increase the surface roughness of the nozzle.

2.5 Additive Manufacturing for Space Applications

Additive manufacturing has been gaining popularity across all fields during the past two decades. Often referred to colloquially as 3D printing, additive manufacturing refers to a variety of manufacturing techniques that operate by building, or printing, products one layer at a time. The method has been used historically as a rapid prototyping technique in part because it eliminates the need to design new tooling and processes prior to validation of the acceptability of the part design. This benefit, among others, leads to considerable cost and schedule savings. Advances in the quality of materials and the processes themselves have led to the evolution of additive

manufacturing from a prototyping process to an acceptable alternative to traditional manufacturing practices for functional parts [7].

The cost and schedule savings associated with additive manufacturing processes have been especially appealing to the budget and time constrained space industry. Metallic additive manufacturing processes, such as DMLS, enable the use of high temperature alloys suitable for spacecraft propulsion systems. Consequentially, researchers at universities and in government labs have begun to investigate the feasibility of utilizing these technologies in the production of space propulsion components. In its efforts to produce the first additively manufactured full scale rocket engine, NASA found that using a powder bed fusion additive manufacturing technique reduced part count by 80% and significantly reduced the requirements for configuration management and process workflows [16]. Figure 3 shows a fuel mixer manufactured for the NASA project, demonstrating the complexity and scale of components that can be additively manufactured for operational use.

Figure 3: Additively Manufactured Fuel Mixer [16]

While the NASA effort involved manufacturing a full scale liquid hydrogen engine, other researchers have focused on additive manufacturing's potential in the manufacturing of microsatellite and CubeSat propulsion systems. However, these studies have focused primarily on examining the cost and schedule implications of the process and the opportunity for seamless integration of the propulsion system into the microsatellite structure [17] [18].

Even with the recent advances in DMLS and related processes, part surface roughness associated with these processes frequently exceeds those characteristic of traditional manufacturing processes. Figure 4 compares micro-nozzles manufactured using the DMLS process to those manufactured by traditional machining. Even to the naked eye, the surface roughness of the DMLS nozzles clearly exceeds that of the machined nozzle. Quantifiable differences in roughness are presented in later chapters.

Figure 4: Machined Nozzle (Left) and DMLS Nozzle (Right)

The high surface-to-volume ratio characteristic of gas flow through micro-nozzles results in susceptibility to frictional losses when operating at low Reynolds numbers [9]. Presumably, the increased surface roughness introduced by additive manufacturing processes serves to increase friction at the nozzle walls. The goal of this research is to investigate the extent to which increased surface roughness at the boundary of a compressible micro flow contributes to viscous losses.

2.6 Surface Roughness and Viscous Losses

The effect of surface roughness on compressible flow through a closed channel is captured in the shear stress at the walls [19]. Section 2.4 characterized the viscous loss terms of the thrust and thrust coefficient as integrations of the local wall shear stress over the length of the nozzle. This shear stress is converted to a dimensionless form in Equation 16 [19].

$$f = \frac{2\tau}{\rho v^2} \tag{16}$$

This dimensionless shear stress is known as the Fanning friction factor. In the case of laminar compressible flow, at Reynolds numbers of approximately 2000 or less for pipe flow, the friction factor is independent of the roughness of the wall surface. In this case, the friction factor is dependent only upon Reynolds number as expressed in Equation 17 [19].

$$f = \frac{16}{Re} \tag{17}$$

In the case of turbulent flow and in the critical transition zone between laminar and turbulent flow beginning at flow Reynolds number of about 2500, this expression of

the Fanning friction factor begins to lose validity. The friction factor must account for the roughness of the wall ϵ. Adopting the method of Oosthuizen and Carscallen, the Fanning friction factor can be calculated using Equation 18 [19].

$$f = \frac{0.0625}{\left[\log\left(\frac{\epsilon}{3.7D_H} + \frac{5.74}{Re^{0.9}}\right)\right]^2} \tag{18}$$

It is often desirable to convert the Fanning friction factor into a Darcy friction factor, another dimensionless representation of wall shear stress. The use of the Darcy friction factor is explored in subsequent chapters. Equation 19 converts between the two factors [19].

$$f_D = 4f \tag{19}$$

While the equations for the friction factors discussed in this section apply specifically to compressible pipe flow, the correlation between surface roughness and magnitude of the wall shear stress also holds for variable area flows like those through a conical nozzle. In the case of variable area flow, the dimensionless shear stress, the Fanning friction factor, can be related to a change in in Mach number [19].

$$\frac{dM}{M} = -\left[\frac{1 + \frac{(\gamma-1)M^2}{2}}{1 - M^2}\right]\left(\frac{dA}{A}\right) + \left[\frac{1 + \frac{(\gamma-1)M^2}{2}}{1 - M^2}\right]\left(\frac{\gamma M^2}{2}\right)\left(\frac{4f\,dx}{D_H}\right) \tag{20}$$

Equation 20 shows that frictional effects introduce an additional loss term not present in the ideal rocket equations and that significant changes in roughness must be considered when analyzing the performance of micro-thrusters. The first term in the equation represents the isentropic flow conditions, while the second term introduces the non-isentropic friction term. Equation 20 can be solved analytically at all points in a

hypothetical thruster. This allows for calculation of key performance variables of interest as described in subsequent chapters.

2.7 Surface Roughness, Turbulence and Shock Formation

The equations of compressible flow with viscous losses presented by both Oosthuizen and Spisz draw a clear correlation between viscous losses and decreases in the thrust coefficient of a converging-diverging nozzle [4] [19]. Oosthuizen also acknowledges the causal relationship between surface roughness and viscous losses [19]. However, neither source accounts for the possibility that increased surface roughness at the nozzle wall may lead to changes in localized flow turbulence or shock wave formation and propagation in the exit cone of the nozzle. Per Krishnamurty, at elevated surface roughness, viscous losses, turbulence and shock-induced losses may not be decoupled [15].

Krishnamurty acknowledges that a roughness induced increase in the viscous boundary layer will result in a decrease in thrust coefficient. However, he argues that, for very rough surfaces, the sand-grain, or absolute, roughness traditionally used to calculate friction factor is insufficient in predicting the effects of roughness on viscous losses. In these cases, it is likely that turbulent effects, such as the formation of vortices at discrete surface protrusions, introduce a drag loss term not typically represented in the calculation of viscous losses [15].

Furthermore, Krishnamurty argues that, in the case of a very rough surface, protrusions cause both changes in the location of shock formation and reflections in the shock waves, weakening the shock-induced pressure-drop across the nozzle.

Unsurprisingly, his models also show that this behavior becomes more pronounced when the expansion half angle of the nozzle decreases, causing the nozzle walls to remain closer together during expansion [15].

Krishnamurty's research suggests that in the case of micro-nozzles, where the heights of discrete protrusions are significant in comparison to the hydraulic cross-section of the nozzle, traditional correlations between surface roughness and viscous losses may be invalid. In these cases, it is not possible to decouple the effects of viscous losses, drag losses and shock-induced losses [15]. Furthermore, depending upon the surface of the individual nozzle in question, the effects of roughness induced drag, shock translation and shock reflection may contribute significantly to the total loss in thrust coefficient. Unfortunately, interactions between these effects are difficult to model simultaneously and experimental validation is required to confirm these theories.

2.8 Literature Review Conclusions

Although the ideal rocket equations describe the fundamentals of the operation of micro-thrusters, they are inadequate in predicting the precise behavior of these thrusters. Low mass flow rates, high temperatures and small throat diameters create conditions for low Reynolds number flow that invalidates the basic assumptions of these equations. Thrusters operating at low Reynolds number flow conditions experience viscous effects that negatively impact their performance. As the use of additive manufacturing practices to manufacture spaceflight parts increases, the added surface roughness induced by these processes may exacerbate these viscous effects and lead to further performance losses. However, literature experimentally validating this hypothesis for micro-thruster

performance does not exist and presents a gap in knowledge in the study of micro-nozzle flow. The goal of this research is to provide experimental data to fill this gap.

III. Methodology

3.1 Introduction

Chapter 2 detailed the gap in understanding of the effects of wall roughness on micro-nozzle viscous performance losses. One of the most convenient means of quantifying these loss term is as a decrease in the thrust coefficient of the nozzle. The primary benefit of using the thrust coefficient is that it may be calculated directly from pressures, temperatures and forces measured experimentally during thruster operation.

In addition to the experiment, an analytic model was developed to predict the effects of viscosity on thrust coefficient. This model solves for the Mach number at all axial locations along the model thruster and uses these predictions to determine the thrust and thrust coefficient. The analytic model is more accurate than isentropic theory as a standard for comparison with experimental results. However, it is acknowledged that this model does not account for more complex mechanisms like protrusion induced drag and shock reflection.

3.2 Experimental Theory

Chapter 2 included a comprehensive review of the theory required for this research. One equation derived from the ideal rocket equations is of particular importance to the experimental phase of this research. The representation of thrust coefficient in Equation 3 is calculated directly from experimental data.

$$C_F = \frac{F}{A_t P_1}$$

The throat area of each nozzle is measured using a scanning electron microscope (SEM). The chamber pressure of the flow is measured using a pressure transducer situated at the junction of the propellant plumbing and the nozzle fitting. The thrust is also measured directly with a load cell mounted to the back of the thrust stand. These three measurements provide all data required to calculate the thrust coefficient. Specifics of the experimental setup are provided in later sections of this chapter. The experimentally calculated thrust coefficients of various nozzle and flow configurations are compared to theoretical expectations using the analytic model described in the next section of this chapter.

3.3 Analytic Model Theory

An analytic model was designed to provide a standard for comparison to the experimental results of this research. The analytic model described in this section is based upon the equations of generalized quasi-one-dimensional flow as presented by Oosthuizen and Carscallen [11]. This is a departure from the methodology used by Spisz and allows for the inclusion of surface roughness in the calculations. An additional goal of this method is to eliminate questionable assumptions used by Spisz in his analytic model. Specifically, although the laminar boundary layer theory for flat plates used by Spisz allowed for convenient algebraic calculation of loss terms, the applicability of this method is questionable for a radially symmetric enclosed passage [4].

These equations have been simplified from their original forms to assume adiabatic flow in accordance with the research objectives laid out in preceding chapters. The goal of this model is to solve for the nozzle exit conditions, and thrust coefficient, by

solving the ordinary differential equation (ODE) presented in Equation 21 for the Mach number (squared) at every axial location along the nozzle. The code employs ode45, one of the built-in Runge-Kutta method solvers in MATLAB to solve for the Mach number squared explicitly [20].

$$\frac{dM^2}{dx} = \left\{ \frac{M^2\left[1+\frac{(\gamma-1)M^2}{2}\right]}{1-M^2} \right\} \left(-\frac{2}{A}\frac{dA}{dx} + \gamma M^2 f \frac{P}{A} \right) \tag{21}$$

3.3.1 Initial Conditions

The analytic model begins with determination of the initial conditions of the ODE. First, initial guesses for the chamber pressure and mass flow rate must be calculated. These guesses are calculated using isentropic relations to achieve the desired throat Reynolds number at a given gas temperature. Manipulating Equation 6 to solve for the mass flow required at a given Reynolds number and chamber temperature yields the following equation. Note that, in this case, P_t is the hydraulic perimeter of the nozzle throat.

$$\dot{m} = \frac{\mu Re P_t}{4} \tag{22}$$

Although Equation 22 is not an explicit function of temperature, the gas temperature is required to determine the coefficient of viscosity. To establish viscosity as a function of temperature, a logarithmic least squares curve fit was applied to the experimental data tabulated by Incropera and DeWitt [21]. As an example, Figure 5 shows the curve fit applied to experimental data for helium. Each gas investigated has a unique viscosity-temperature relationship as tabulated in Table 1.

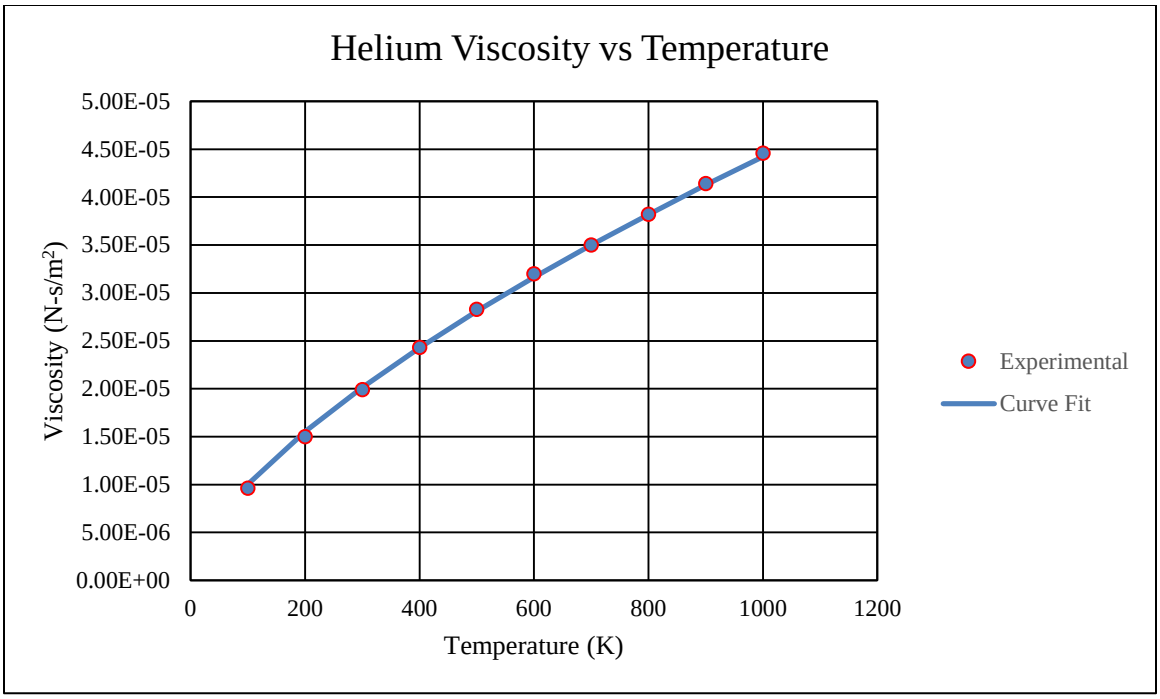

Figure 5: Helium Viscosity Curve Fit

Table 1: Temperature-Viscosity Relationships

Gas	Viscosity (N-s/m^2)
Nitrogen	$\mu = (3.20 \times 10^{-7})T^{0.699} + 4.28 \times 10^{-7}$
Helium	$\mu = (4.31 \times 10^{-7})T^{0.668} + 6.61 \times 10^{-7}$
Carbon Dioxide	$\mu = (1.322 \times 10^{-7})T^{0.829} + 1.57 \times 10^{-7}$

The second variable required to calculate the initial conditions is the chamber pressure associated with the desired throat Reynolds number. Once again, isentropic relationships are used to provide an initial guess at this chamber pressure. In accordance with Sutton and Biblarz, and with the simplification that for isentropic, adiabatic flow,

the chamber static pressure is essentially equal to the chamber stagnation pressure, the chamber pressure may be calculated as follows [2].

$$P_{ch} = \frac{\dot{m}\sqrt{\gamma R T_{ch}}}{A_t \gamma \sqrt{\left(\frac{2}{\gamma+1}\right)^{\frac{\gamma+1}{\gamma-1}}}} \tag{23}$$

It is important to note that, because both the initial mass flow and initial chamber pressure were calculated using isentropic relations, iteration is required within the analytic model to reach the desired throat Reynolds number and choked flow conditions when viscous effects are considered. The next step in determining the initial Mach number is to calculate the density of the gas in the chamber in accordance with the Ideal Gas Law.

$$\rho_{ch} = \frac{P_{ch}}{R_{spec} T_{ch}} \tag{24}$$

The velocity of the gas in the chamber is then calculated using the mass flow rate and area of the chamber.

$$v_{ch} = \frac{\dot{m}}{\rho_{ch} A_{ch}} \tag{25}$$

Finally, the prediction for the Mach number in the chamber is calculated using the local gas velocity in the chamber.

$$M_{ch} = \frac{v_{ch}}{\sqrt{\gamma R_{spec} T_{ch}}} \tag{26}$$

The initial conditions required to solve Equation 21 consist of the initial (chamber) Mach number and the starting axial location. The starting axial location is

defined as the entrance to the thruster chamber. These initial conditions are defined below.

$$M_0^2 = M_{ch}^2$$

$$x_0 = 0$$

3.3.2 Thruster Geometry

Prior to solving the ODE in Equation 21, the geometry of the model thruster must be established. The change in area with respect to axial position may be determined using the diameter of the nozzle at the current axial position and a non-dimensional diameter change coefficient (A_D) in accordance with the methods of Oosthuizen and Carscallen [11]. Because the diameter variation is linear for a conical nozzle, this coefficient is derived from the slope of the nozzle wall between two points as shown in Figure 6 for the divergent section of the nozzle.

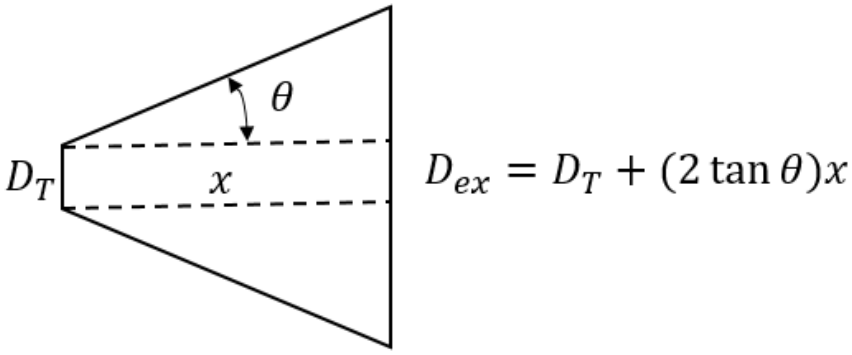

Figure 6: Diameter Variation in Divergent Nozzle

Using this method, the diameter change coefficient for any section of the thruster is defined below. The angle between the thruster wall and horizontal represents the expansion half angle of the nozzle section.

$$A_{D,i} = 2tan\theta_i \tag{27}$$

Each section of the thruster has a unique diameter change coefficient determined by its expansion half angle. Therefore, the solver is split into a series of statements specific to the current section of the thruster. Figure 7 is a cross-sectional view of the nozzle divided into four distinct chamber, convergent, throat and divergent sections.

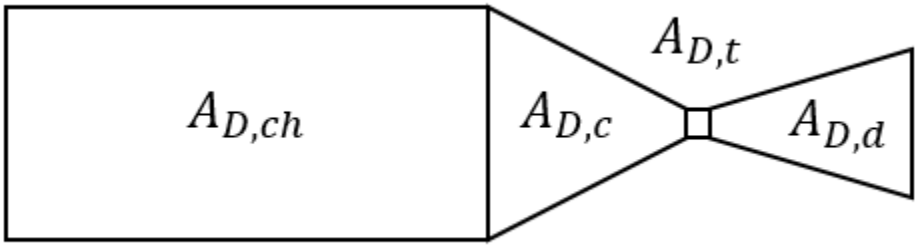

Figure 7: Model Thruster Geometry

Because the diameter is constant in the chamber and throat sections, the area change term in Equation 21 drops out and the change in Mach number in these sections is effected only by shear stress at the walls (friction). However, in the convergent and divergent sections, the diameter change coefficient must be used to calculate the diameter at the current axial location as shown in Equation 28.

$$D = D_{0,i} + A_{D,i}x \tag{28}$$

Knowledge of the diameter change coefficient and current diameter allows for calculation of the area change at this location as shown in Equation 29.

$$\frac{dA}{dx} = \frac{\pi D}{2}\frac{dD}{dx} = \frac{\pi D A_D}{2} \tag{29}$$

3.3.3 Solution to the ODE

Determination of the temperature, pressure and friction factor at all axial locations is necessary for the final solution to the ODE. Because temperature and pressure are explicit functions of the current Mach number, this series of equations must be solved for simultaneously with the Mach number when ode45 is called. First, the temperature is found by relating the current Mach number squared to the chamber Mach number squared and utilizing the chamber temperature.

$$T = T_0 \frac{\left[1 + \frac{(\gamma - 1)M_0^2}{2}\right]}{\left[1 + \frac{(\gamma - 1)M^2}{2}\right]} \tag{30}$$

Given the current temperature, the current (static) pressure is calculated by relating the current Mach number, cross sectional area and temperature to the initial conditions in the chamber and utilizing the initial pressure in the chamber.

$$P = P_{ch}\frac{M_0}{M}\frac{A_{ch}}{A}\sqrt{\frac{T}{T_0}} \tag{31}$$

Per the Ideal Gas Law, the density at the current position is a function of the current pressure and temperature calculated above.

$$\rho = \frac{P}{R_{spec}T} \tag{32}$$

The local gas velocity is calculated from the Mach number and static temperature using Equation 33.

$$v = M\sqrt{\gamma R_{spec}T} \tag{33}$$

In the case of nitrogen, the local viscosity is calculated using the following equation from Table 1.

$$\mu = (3.203 \times 10^{-7})T^{0.69898} + 4.28 \times 10^{-7}$$

The Reynolds number must be calculated in accordance with Equation 6 to determine the appropriate expression of the Fanning friction factor for use in Equation 21. In accordance with Oosthuizen and Carscallen, it is assumed that the flow is fully turbulent at Reynolds numbers greater than 2000 and fully laminar at Reynolds numbers below 2000 [11]. Depending upon the nature of the flow, the Fanning friction factor is calculated using the following equations. Note, in the turbulent case, the variable epsilon is the wall roughness as defined in Chapter 2.

$$f_{turbulent} = \frac{0.0625}{\left[\log\left(\frac{\epsilon}{3.7D_H} + \frac{5.74}{Re^{0.9}}\right)\right]^2} \tag{34}$$

$$f_{laminar} = \frac{16}{Re} \tag{35}$$

The differential equation for the variation of the Mach number squared with respect to axial distance as expressed in Equation 21 completes the system of equations passed to ode45. Table 2 summarizes the system of equations solved at every axial location in the nozzle by the function MachSolver.m.

Table 2: MachSolver.m Algorithm

$$D = D_{0,i} + A_{D,i}x$$

$$\frac{dA}{dx} = \frac{\pi D}{2}\frac{dD}{dx} = \frac{\pi D A_D}{2}$$

$$A = \frac{\pi D^2}{4}$$

$$T = T_0 \frac{\left[1 + \frac{(\gamma - 1)M_0^2}{2}\right]}{\left[1 + \frac{(\gamma - 1)M^2}{2}\right]}$$

$$P = P_{ch}\frac{M_0}{M}\frac{A_{ch}}{A}\sqrt{\frac{T}{T_0}}$$

$$\rho = \frac{P}{R_{spec}T}$$

$$v = M\sqrt{\gamma R_{spec}T}$$

$$\mu = (3.203 \times 10^{-7})T^{0.69898} + 4.28 \times 10^{-7}$$

$$Re = \frac{\rho v D}{\mu}$$

If Re>2000 (Turbulent):

$$f = \frac{0.0625}{\left[\log\left(\frac{\varepsilon}{3.7D_H} + \frac{5.74}{Re^{0.9}}\right)\right]^2}$$

If Re<2000 (Laminar):

$$f = \frac{16}{Re}$$

$$G = -\frac{2}{A}\frac{dA}{dx} + \gamma M^2 f\frac{P}{A}$$

$$\frac{dM^2}{dx} = \left\{\frac{M^2\left[1 + \frac{(\gamma-1)M^2}{2}\right]}{1 - M^2}\right\}G$$

3.3.4 Iteration and Discontinuity at the Sonic Point

Because the original estimates for the pressure and Mach number of the flow in the chamber were developed using isentropic relations, the initial iteration of the Mach number algorithm does not converge on the desired throat Reynolds number. Therefore, an iterative process is established to create a new estimate for the starting conditions.

Additionally, the computer model is designed to assume a choked flow condition in which the sonic point is reached at the throat exit plane. Oosthuizen and Carscallen establish that the sonic point in a quasi-one dimensional adiabatic flow with frictional losses will take place in the divergent section of the nozzle [11]. However, it is assumed that this sonic point will remain near the throat exit. Therefore, establishing a choked flow approximation eases the burden of calculation considerably without introducing large losses in fidelity. This is the second constraint to be met while iterating initial conditions.

Given the choked flow and throat Reynolds number constraints, the initial chamber pressure and Mach number are iterated until reaching the desired Reynolds number at the throat exit while the Mach number at that location approaches unity simultaneously. Equation 21 exhibits a discontinuity in the ODE at the sonic Mach. Therefore, iteration of the Mach number is halted just before a value of one at the throat exit and resumes after stepping across the discontinuity at a slightly supersonic Mach number in the divergent section of the nozzle. Figure 8 provides an example of the final, converged iteration. The two vertical lines represent the throat entrance and exit respectively.

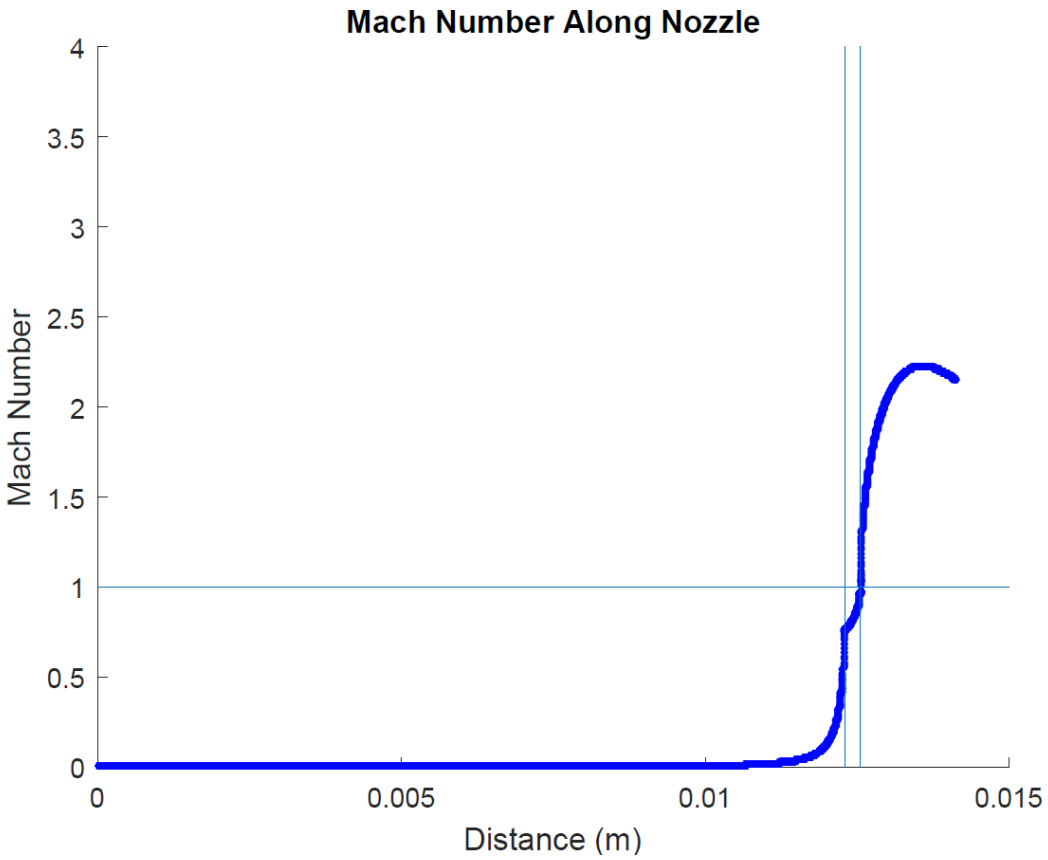

Figure 8: Mach Number vs Axial Thruster Location

The separate areas of the thruster are distinctly defined in Figure 8. There are minimal changes in Mach number in the chamber of the thruster followed by an exponential increase in Mach number in the convergent section. Although the throat section of the nozzle does not contain an area change term, the friction at the nozzle wall causes an increase in Mach number because the flow is still subsonic [11]. After jumping the transonic discontinuity at the throat, the Mach number continues to increase through the diverging nozzle section. Note that the Mach number begins to decrease prior to exiting the nozzle. This sign flip in the rate of change of the Mach number represents the point at which friction forces begin to dominate the ODE. Examination of Equation 21

shows that, once the frictional loss term begins to dominate, Mach number decreases with increase in flow area in supersonic flow.

3.3.5 Calculation of the Performance Characteristics of Interest

After performing the iterations above to determine the Mach number at every point in the thruster, the nozzle exit conditions are used to calculate the performance characteristics of interest. First, the thrust is calculated using the exit pressure, temperature and Mach number. Assuming vacuum ambient conditions, the thrust equation as presented by Sutton and Biblarz may be simplified [2].

$$F = \dot{m}\frac{M_{ex}}{\sqrt{\gamma R_{spec} T}} + (P_2 - P_3)A_{ex} \tag{36}$$

The thrust coefficient is then calculated using the throat area and stagnation pressure in the chamber. The stagnation temperature is calculated from the static pressure using the following relationship.

$$P_0 = P\left(\frac{T_0}{T}\right)^{\frac{\gamma}{\gamma-1}} \tag{37}$$

Although very nearly equal, the stagnation temperature and static temperature in the chamber are not identical in our situation because the initial Mach is non-zero. Therefore, the stagnation temperature in the chamber must be calculated using the following relationship.

$$T_0 = T_{ch}\left(1 + \frac{\gamma - 1}{2}M_0^2\right) \tag{38}$$

Solving for the stagnation pressure from the static and stagnation temperatures in the chamber allows for the final calculation of the thrust coefficient. The thrust

coefficient is the ultimate performance measure of interest and this step concludes the analytic process.

$$C_F = \frac{F}{P_0 A_t} \tag{39}$$

3.4 Experimental Materials and Equipment

This section details the materials and equipment required to implement the experimental portion of this research. Heated carbon dioxide, nitrogen and helium flow through a converging-diverging conical nozzle mounted to an inverted-pendulum thrust stand in a near vacuum environment. Nozzles were manufactured using both EDM and DMLS processes to provide a variety of geometries and roughness profiles. Thrust and stagnation pressure are measured directly using a load cell and pressure transducer. The data is collected using LabView, allowing for calculation of the thrust coefficient as presented in Equation 3. Figure 9 is a schematic of the experimental setup.

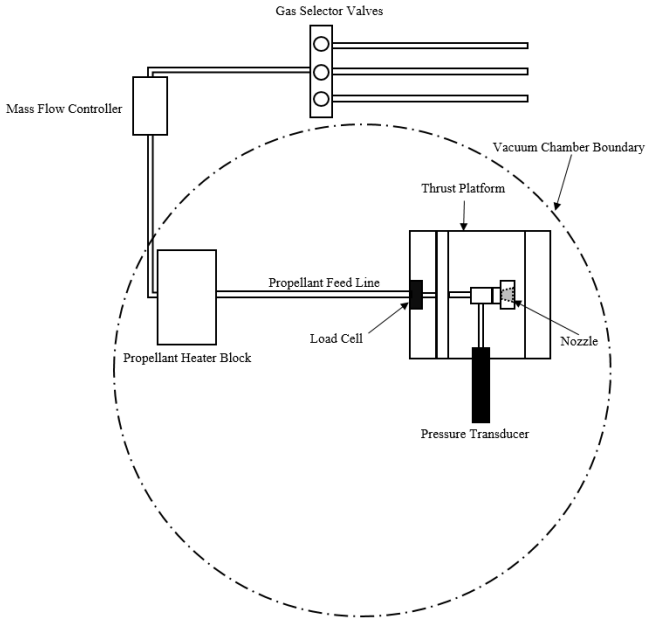

Figure 9: Experimental Setup

3.4.1 Nozzle Design

Micro-nozzles were designed to allow for testing across a variety of relative throat roughness values and expansion ratios. To facilitate ease of removal and installation, the nozzles in this experiment were designed with exterior threads compatible with national pipe threaded (NPT) Swagelok™ fittings. Additionally, the outer surface at the exit plane was designed as a hexagonal head compatible with traditional wrenches. Figure 10 depicts an additively manufactured nozzle mounted in the Swagelok™ fitting prior to testing.

Figure 10: Experimentally Mounted DMLS Nozzle

Variation of relative roughness was essential to providing unique nozzle geometries for testing. Relative roughness is defined by Moody as the ratio of the absolute, or sand-grain, roughness to the hydraulic diameter of the orifice as shown in Equation 40 [22].

$$\frac{\epsilon}{D_H} \tag{40}$$

From Equation 40, it follows that the relative roughness may be varied either by changing the absolute roughness of the material or by changing the throat diameter. Two nominal throat diameters of 0.015 and 0.030-inches were chosen to achieve hydraulic diameter variation.

To vary absolute roughness, nozzles were manufactured using two methods: traditional machining practices and DMLS. The first two nozzles, intended to exhibit lower absolute roughness, were manufactured using a combination of traditional machining practices. These nozzles were manufactured from hexagonal stainless steel bar stock. Primary shaping of the stock was accomplished by turning the bar on a lathe.

However, the divergent flow area of the nozzle between the throat and exit plane was formed using wire electrical discharge machining (EDM). Thirty-six additional nozzles were manufactured using DMLS processes out of Haynes 282 nickel alloy designed specifically for high temperature aerospace applications, with a thermal conductivity of approximately 16 W/m.^{o}C in the temperature ranges investigated in this study [23]. The images in Figures 11 and 12 were taken using a Scanning Electron Microscope (SEM) and provide a comparison between the surface profiles of the additively manufactured and EDM nozzle throats.

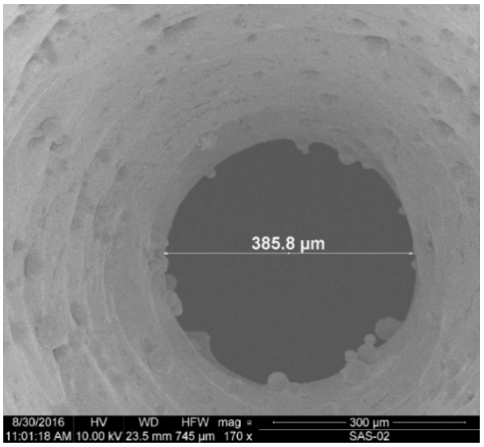

Figure 11: DMLS Nozzle Throat Roughness

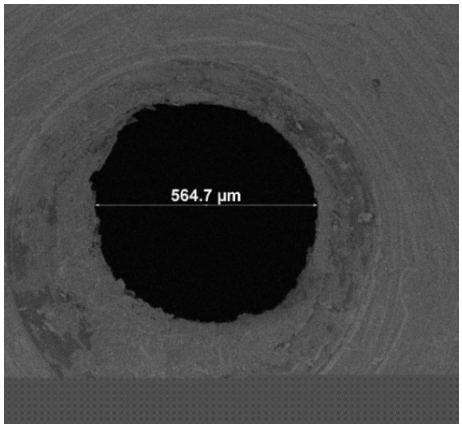

Figure 12: EDM Nozzle Throat Roughness

Figures 11 and 12 clearly show a substantial difference in surface profile between the EDM and DMLS nozzles. A laser scanning microscope was used to determine the average surface roughness of both the EDM and DMLS nozzles. This data was then used to determine the appropriate absolute roughness for use in the analytic model and to formulate additional performance loss theories. The results of the laser scan are discussed in detail in Chapter 4.

To increase the spread of data, nozzles were manufactured with a variety of expansion ratios. The expansion ratio of a nozzle is defined as the ratio between the area of the exit plane and the area of the throat plane as represented in Equation 41.

$$\varepsilon = \frac{A_e}{A_t} \tag{41}$$

Expansion ratios for the EDM nozzles were initially chosen to correspond closely to the optimal expansion ratios calculated by Spisz in his initial study [4]. However, inability to meet manufacturing tolerances resulted in larger throat diameters, and lower expansion ratios, than originally targeted. DMLS nozzles were manufactured to correspond closely with the expansion ratios of the EDM nozzles. Additionally, the DMLS group provides a variation of geometries that would require excessive time and cost to manufacture by traditional means. Table 3 provides a breakdown of the nominal nozzle sizes manufactured.

Table 3: Nominal Nozzle Dimensions

Throat Diameter (in)	Throat Area (in^2)	ε	Exit Area (in^2)	Exit Diameter (in)	Manufacturing Method
0.015	0.00018	20	0.00353	0.06708	EDM

0.015	0.00018	40	0.00707	0.09487	EDM
0.015	0.00018	5	0.00088	0.03354	DMLS
0.015	0.00018	10	0.00177	0.04743	DMLS
0.015	0.00018	20	0.00353	0.06708	DMLS
0.015	0.00018	30	0.00530	0.08216	DMLS
0.015	0.00018	40	0.00707	0.09487	DMLS
0.015	0.00018	50	0.00884	0.10607	DMLS
0.015	0.00018	80	0.01414	0.13416	DMLS
0.030	0.00071	20	0.01414	0.13416	DMLS
0.030	0.00071	30	0.02121	0.16432	DMLS
0.030	0.00071	40	0.02827	0.18974	DMLS
0.030	0.00071	50	0.03534	0.21213	DMLS
0.030	0.00071	100	0.07069	0.30000	DMLS

Discrepancies between the nominal and as-manufactured configurations due to manufacturing tolerances are unavoidable in nozzles on this scale. Deviations were documented to calculate the appropriate mass flow rate to produce the throat Reynolds numbers desired for each configuration as described later in this chapter. Additionally, the area of the throat must be accurately known to calculate the thrust coefficient experimentally using Equation 3.

A Zeiss stereomicroscope was used to measure the throat and exit diameters of each nozzle. Because the throat and exit planes are not perfect circles, the semi-major and semi-minor axes were measured. Then, the throat and exit areas were calculated as low-eccentricity ellipses using Equation 42.

$$A_{ellipse} = \pi ab \tag{42}$$

When viewed using the stereoscope, the hole diameters appear slightly elongated and distorted. To minimize these effects on measurement accuracy, a series of wedges ranging in elevation angle from 5^o to 15^o were additively manufactured to provide a platform for the nozzle to rest on during measurement. It was determined that at the magnification and light settings used for measurement that a 7.5^o wedge eliminated nearly all effects of stereoscopic distortion. Still, uncertainty resulting from this method is included in the uncertainty analysis detailed later in this chapter.

Figure 13 is a representative example of this measurement technique. All measurements of the as-manufactured configurations are included in the Appendix.

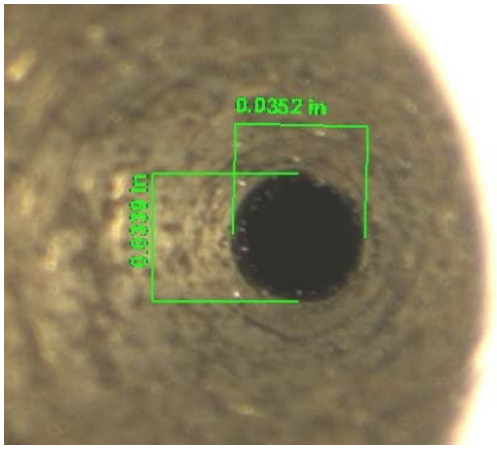

Figure 13: Microscopic Hole Measurement

3.4.2 Vacuum Chamber

To achieve the flow conditions desired, it was necessary to perform the experiment at near vacuum conditions. The bell vacuum chamber at AFIT provided a sufficient volume to house the experimental apparatus while minimizing the time required to reach the pressures necessary. Prior to every test, the chamber was pumped

down to a pressure of no greater than 80 mTorr to reduce the risk of separation of the flow in the diverging section of the nozzle. All chamber pumping was achieved using the chamber's roughing vacuum pump. Figure 14 is an image of the vacuum chamber during experimental operation.

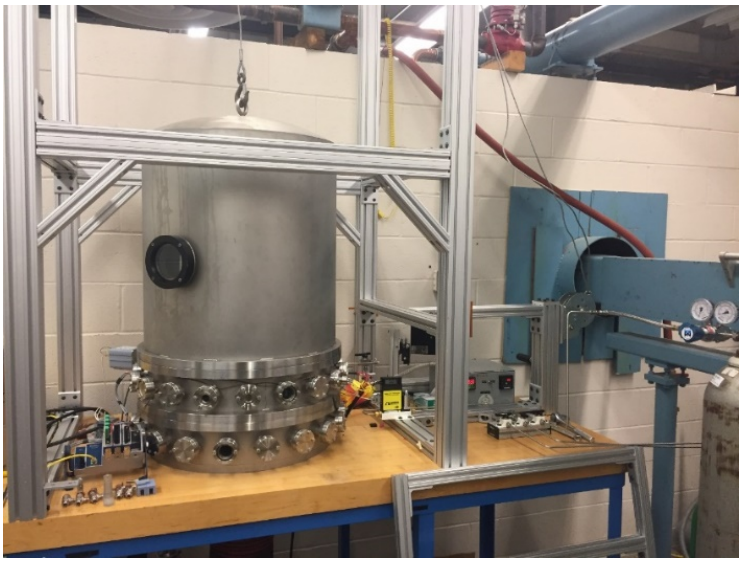

Figure 14: Vacuum Chamber in Operation

3.4.3 Thrust Stand

The thrust stand for this experiment was designed to allow for direct measurement of the thrust. It also provides a platform to connect the required plumbing and data collection instruments. Figure 15 shows the thrust stand mounted inside the vacuum chamber during experimental set up. To dampen vibrations induced by the roughing pump, lead and bronze weights were stacked in and around the thrust stand. Two of these weights are visible in the lower right hand corner of Figure 15.

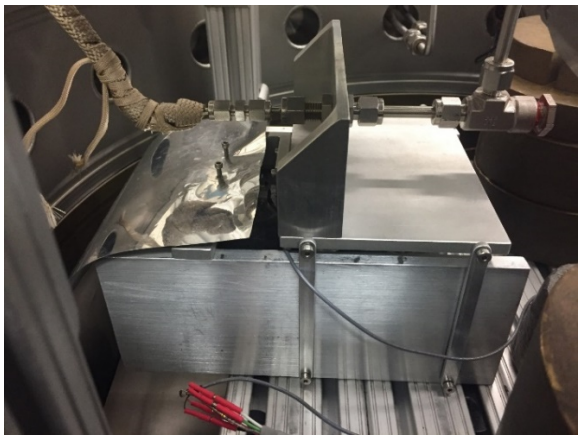

Figure 15: Inverted Double Pendulum Thrust Stand

During experimental operation, the force produced by the gas expanding through the nozzle is transferred through the bulkhead to the load cell rigidly mounted to the rear of the test stand as shown in Figure 16. Mounting the load cell directly to the thrust stand minimizes the deflection of the thrust bulkhead on the pendulum arms. In doing so, the effect of kinetic friction in the joints of the pendulum arms becomes negligible. Additional details for the load cell, including calibration methods, are included later in this chapter.

Figure 16: Load Cell Mounted in Thrust Stand

3.4.4 Mass Flow Controller

Control of the gas flow is achieved using an Omega FMA5400A Mass Flow Controller. The controller is set to a specific volumetric flow rate corresponding to the desired mass flow rate of the gas. Conversion from mass flow rate to volumetric flow rate is achieved using the density of the propellant gas at standard temperature and pressure (STP) conditions. The gas flows through the controller prior to being heated; therefore, STP conditions are suitable for this conversion.

Because this mass flow controller was calibrated for use with nitrogen, it is necessary to include a correction factor when setting the mass flow for use with helium and carbon dioxide [24]. The mass flow setting on the controller is calculated by scaling the mass flow calculated for the test condition by a correction factor as shown in Equation 43. The manufacturer lists the appropriate correction factors as shown in Table 4 [24]. Figure 18 depicts the mass flow controller as configured prior to a test.

$$\dot{m}_{actual} = K\dot{m}_{calc} \tag{43}$$

Table 4: Mass Flow Meter Correction Factor

Gas	K_c
Nitrogen	1
Carbon Dioxide	0.738
Helium	1.454

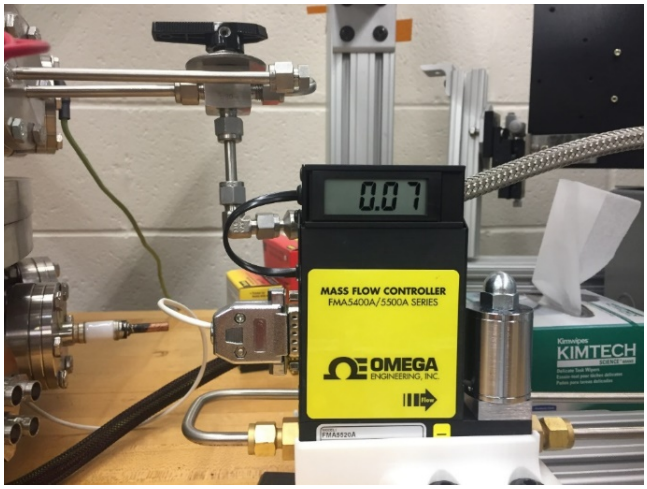

Figure 17: Mass Flow Controller Mounted

3.4.5 Heater Block and Thermocouple

To fully control the throat Reynolds number, the gas is heated to between 500 and 600 Kelvin after entering the vacuum chamber. The gas is heated by flowing through a stainless-steel heater block with an internally machined "s-curve" flow path. The fully assembled heater block in testing configuration is depicted in Figure 19.

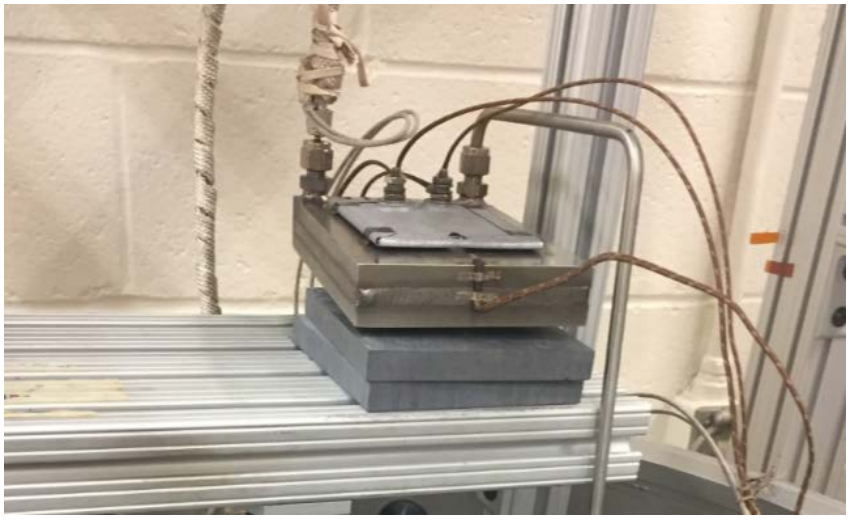

Figure 18: Heater Block Assembly

A uniform heater block temperature is achieved by applying resistance heaters to the upper and lower surfaces of the block. Original tests with one resistance heater proved insufficient to achieve the temperatures required to achieve the gas viscosities, and therefore Reynolds numbers, desired. The heater block platform is thermally protected from the temperatures of the heater block using two ceramic blocks as insulators. Temperature control is achieved by attaching a thermocouple to the heater block and outputting to an FE PXR-4 heater controller which relays the appropriate signal to the resistance heaters.

The temperature reading is collected in LabView to monitor during testing. This heater block temperature is assumed to be the steady state gas temperature at the chamber of the thruster. It is possible that heat dissipation in the plumbing between the heater block and the mounted nozzle results in a decrease in gas temperature. However, it is estimated that this dissipation is minimal. Additionally, small fluctuations in temperature drive minimal uncertainty in the throat Reynolds number.

3.4.6 Load Cell and Pressure Transducer

The thrust is measured using a Strain Measurement Devices (SMD) load cell. When the load cell is deflected by an applied load, the resistance of the embedded strain gauge is altered, as measured using the Wheatstone bridge, resulting in a change in output voltage. The load cell used in this research was rated to register up to 20 N of load.

Calibration was required to provide a correlation between output voltage and applied load. Because of load cell sensitivity to ambient vibrations and minor contact to the thrust stand, the load cell had to be calibrated outside of the experimental apparatus. Therefore, a custom calibration platform was built to ensure repeatability and accuracy of

load measurement. The load cell is mounted vertically in the test stand with the load applied at the tip of the cell as shown in Figure 19. Calibration was later verified inside of the experimental setup.

Figure 19: Load Cell Mounted for Calibration

Because the load cell is mounted vertically for calibration, the load cell weight is included in the load measured, and signal output, by the cell. To correct for this factor, this calibration was achieved using a three-step process. Prior to mounting in the calibration stand, the zero-load configuration was measured by laying the load cell flat on its side. Then, the load cell was mounted without an applied external load and the output voltage was noted. To determine and correct for the load cell weight, the difference between the flat zero load configuration and the mounted zero load configuration is taken as shown in Equation 44.

$$V_{cell} = V_{mounted} - V_{flat} \tag{44}$$

Finally, the voltage output is noted when applying a known external load applied using high accuracy test masses ranging between 1 and 50 grams. The voltage

corresponding to the weight of the load cell is then subtracted from this voltage to provide the true load voltage as shown in Equation 45. Finally, the calibration is fine tuned in LabView using a range of known test masses.

$$V_{load} = V_{measured} - V_{cell} \tag{45}$$

After the load cell was calibrated, it was installed into the experimental thrust stand and a calibration verification was performed. A test mass was suspended from the rear of the thrust platform in an orientation meant to minimize off-axis force application. The force applied was then measured in LabView and fell well within the bias uncertainty of the load cell as described later in this chapter.

The pressure transducer used to measure the stagnation pressure in the thruster "chamber" was a Honeywell A-105, 500 PSIG maximum pressure transducer with a stainless-steel extension added to reduce the gas temperature to within operational limits. Calibration of the pressure transducer was achieved directly using a Beta 150 PSI maximum pressure calibrator. The Beta tester's internal pump was used to vary the calibration pressures between 0 and 50 PSI gauge pressure. AFIT's weather system barometer was used to determine the ambient absolute pressure to correct the tester's gauge output. The output voltage of the pressure transducer was then converted to an associated pressure within LabView. Figure 20 shows the pressure transducer and heat dissipating extension as mounted for the experiment.

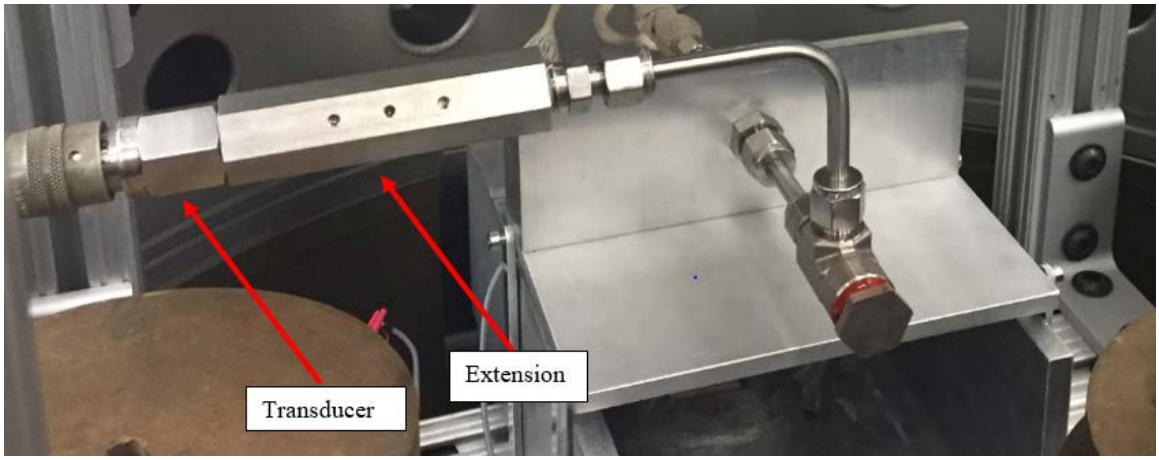

Figure 20: Mounted Pressure Transducer

3.4.7 Data Acquisition Hardware and Software

All experimental measurements are output as voltages from their respective measurement devices to a National Instruments NI cDAQ-9184, where the signal is directed to the desktop computer running LabView. Figure 21 provides a breakdown of all signals being tracked by LabView during testing. The raw data is collected by LabView and converted to the variables of interest as described in the calibration section earlier in this chapter.

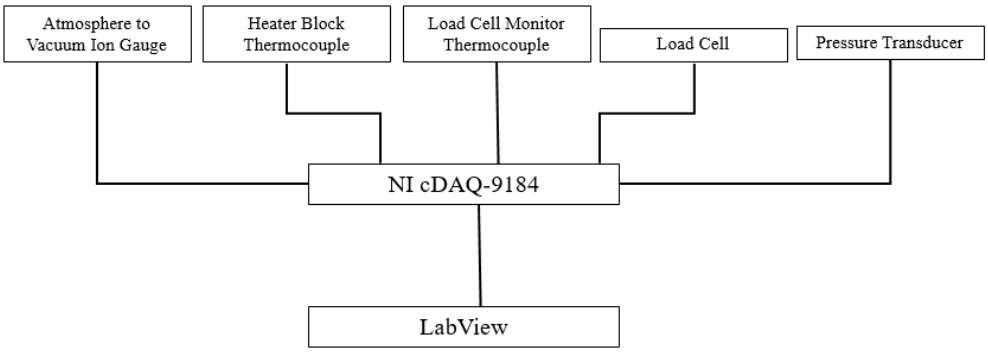

Figure 21: Signal Flow Chart

3.5 Experimental Procedures and Processes

This section provides an overview of the experimental procedure employed in this research. The procedure was developed to eliminate extraneous variables, allowing for accurate comparison between test cases. This section also details the process used to analyze the experimental data collected and the uncertainty analysis applied to that data.

3.5.1 Experimental Procedure Overview

A standard experimental methodology was developed to measure the performance characteristics of each manufactured nozzle over a variety of flow conditions. First, the vacuum chamber was pumped down to a maximum pressure of 80 mTorr and the heater block was preheated to between 530 and 616 Kelvin depending upon the flow conditions being targeted. Flow conditions were determined using the same isentropic flow calculations used to establish the initial conditions of the analytic model. Once the desired ambient pressure and heater block temperature had stabilized, the mass flow controller was set to the desired flow rate as described earlier in this chapter. A series of valves allowed for convenient selection of the desired test gas as shown in Figure 22.

Figure 22: Gas Selection Valves

Prior to initiating data collection in LabView and introducing gas flow, the roughing pump used to pull vacuum was shut down. In early test runs, it was determined that the vibration caused by the roughing pump resulted in sinusoidal oscillation of the load measurement. In many cases, the amplitude of this oscillation exceeded 100% of the expected measurement value. Figure 23 shows the variation in measured load with the pump running and turned off. In this case, there is no gas flow and the load cell should be reading zero applied load. This test drove the decision to cease pump operation during data collection. Fortunately, gas flow rates were sufficiently low such that, in most cases, ambient pressure within the vacuum chamber did not rise enough to present a risk of flow separation.

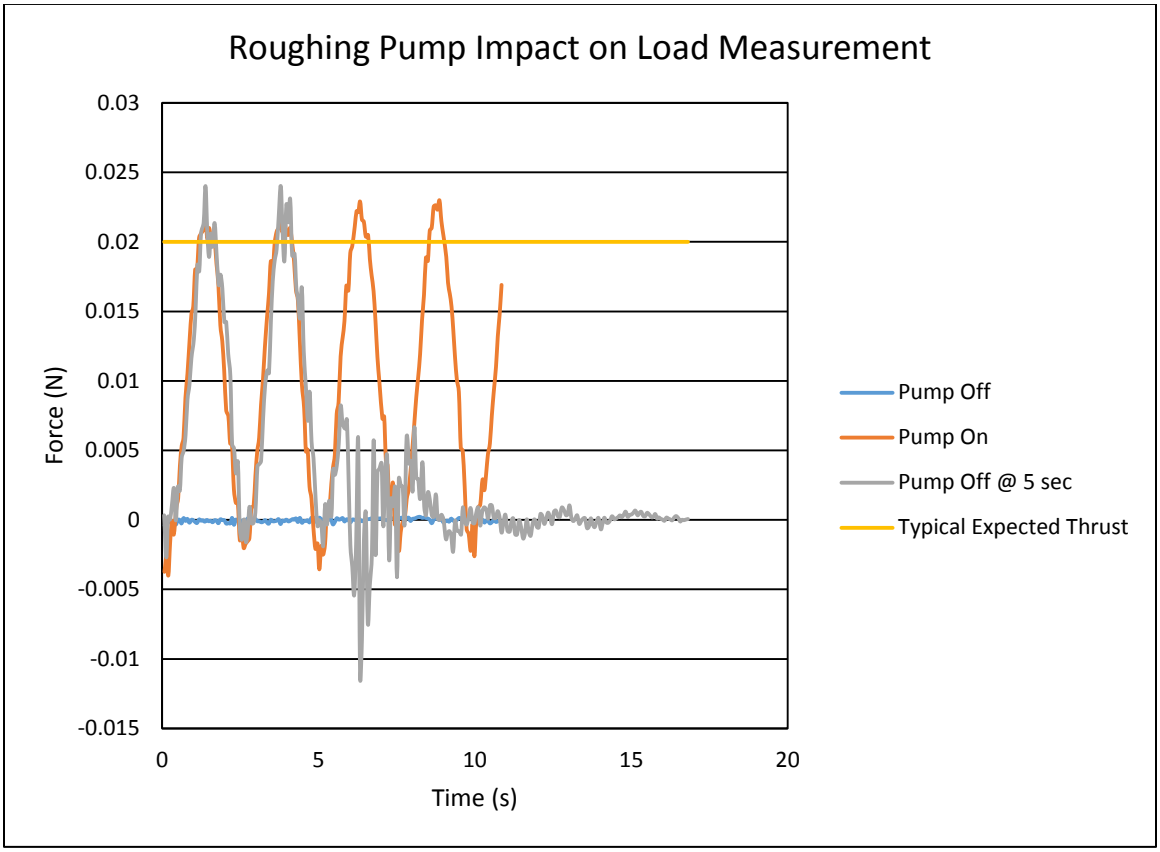

Figure 23: Impact of Roughing Pump on Load Measurement

Following shut down of the roughing pump, the current applied load was zeroed to remove any offset developed during the pumping process. Gas flow was initiated with the flow directed outside of the chamber to allow the mass flow controller to throttle down to the desired flow rate. This step was necessary because it was discovered that flowing directly through the nozzle during this throttling process introduced load cell hysteresis and an unknown offset to the steady state load data.

Once the mass flow reached its steady value, data collection was turned on in LabView and flow was redirected into the chamber. Load, thruster stagnation pressure, ambient chamber pressure and heater block temperature were tracked at all points during the run. Gas flow was shut down and data collection turned off once the measured thrust reached a steady state condition for approximately 5 seconds.

3.5.2 Data Analysis

For each test case, the raw data was exported to Microsoft Excel to be analyzed. The measured load and stagnation pressure were then plotted to identify the steady state conditions. Figure 24 depicts thrust and pressure data of a typical test with conditions set to achieve a throat Reynolds number of 5,000 with carbon dioxide.

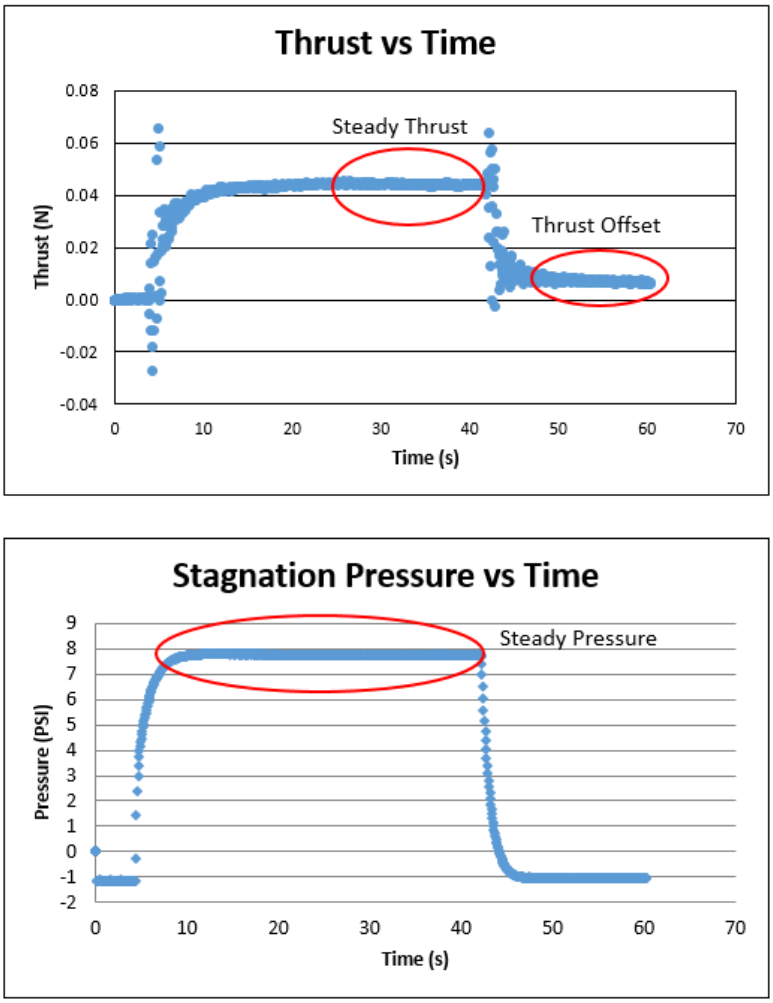

Figure 24: Experimental Thrust and Pressure Data

As indicated in Figure 24, a steady state load offset was also identified for the load cell. The load induced by flow initiation and shutoff, combined with the behavior of the load cell, resulted in an artificially high measurement of the applied load at the steady state condition. This behavior was later reproduced and validated during calibration verification. The actual applied load can be determined by subtracting the final steady state offset after flow shutoff. The uncertainty associated with this method is addressed

later in this chapter. Equation 46 describes the calculation of the actual steady state thrust based on experimental measurement.

$$F_{ss} = F_{ss,measured} - F_{offset} \tag{46}$$

Next, to provide a standard basis for comparison between tests, it is necessary to convert the measured load to an associated vacuum thrust by adding the product of the exit area and ambient vacuum chamber pressure to the measured thrust. The applicability of this method is best demonstrated by manipulating Equation 1 which provides the general thrust equation to obtain Equation 2, the vacuum thrust.

$$F_{vac} = \dot{m}v_{ex} + (P_2 - P_{ambient})A_{ex} + (P_{ambient}A_{ex}) = \dot{m}v_{ex} + P_2A_{ex}$$

Applying this methodology to the experimentally measured data, the equation for determining the vacuum thrust takes on the following form.

$$F_{vac} = F_{ss} + A_{ex}P_{vac}C \tag{47}$$

The constant trailing the vacuum pressure in Equation 47 is a correction factor designated by the manufacturer of the ion gauge used to take the ambient pressure. This correction factor accounts for the differences in thermal conductivity between the gases used in this research [25]. Table 5 provides the gas correction factors for the three gases.

Table 5: Vacuum Pressure Correction Factors

Gas	**C**
Nitrogen	1
Carbon Dioxide	1.42
Helium	0.18

Finally, the vacuum thrust coefficient is calculated from the steady state vacuum thrust, the steady state stagnation pressure and the throat area of the nozzle as follows.

$$C_F = \frac{F_{ss,vac}}{P_{ch}A_t} \tag{48}$$

3.5.3 Uncertainty Analysis

The uncertainty analysis is broken into two components: bias and precision uncertainty. In this case, the precision uncertainty is defined as the uncertainty resulting from the variation in experimental measurement in a finite sample population. The bias uncertainty takes into account the uncertainty inherent in the devices being used to collect this data [26]. Combination of the bias and precision uncertainty generates the total uncertainty. However, the variation in measurement of the sample population cannot be de-coupled from the bias error in the instrumentation. Therefore, it is likely that this method overestimates the error in the data.

The experimental thrust coefficient, as defined in Equation 48, is a function of three separate experimental variables: chamber pressure, throat area and thrust. These three variables have distinct uncertainties associated with the instrumentation used to collect the data. The uncertainty terms provided by the manufacturer are listed in the following tables. These terms are identified as either precision or bias in accordance with Wheeler and Ganji's definitions [26].

The following uncertainty terms are provided by the load cell manufacturer. The rated output of the load cell used is 2 kg.

Table 6: Load Cell Manufacturer Uncertainty

Uncertainty Term	Limit Value	Error Magnitude (N)	Uncertainty Type
Hysteresis	.02 (% Rated Output)	0.00392	Bias
Long Term Stability	.04 (% Rated Output)	N/A	N/A
Nonlinearity	.1 (% Rated Output)	0.0196122	Bias
Non-Repeatability	.01 (% Rated Output)	0.00196	Precision
Creep	.05 (% Rated Output)	N/A	N/A
Temperature Effect	.014 (% of Reading/^{o}F)	N/A	N/A

Experimental thrust measurements for the flow scenarios investigated in this study are typically on the order of tens of milliNewtons. Therefore, the combination of nonlinearity and hysteresis uncertainties provided by the manufacturer will result in an error of up to 100% of the expected output. Furthermore, the magnitude of the errors as predicted by the manufacturer far exceeded results as measured in the lab.

To more accurately predict the true bias uncertainty, the load cell was re-calibrated at low applied loads (1 to 50 grams) to ensure linearity and accuracy in the region of interest. Accuracy uncertainty was then calculated at 1 gram (~10 mN) of applied load after re-calibration. During calibration, hysteresis and non-repeatability were clearly visible in the load cell output as shown in Figure 25. This offset behavior is the same behavior observed experimentally and discussed in the previous section of this chapter. The total load is calculated by subtracting the non-zero bias after load removal

from the maximum registered force. The load cell bias error is then calculated as a percentage of applied load as follows.

$$U_{B,F} = \frac{F_{\max} - F_{offset}}{F_{test}} X\ 100 \tag{49}$$

This procedure was carried out three times to determine the spread of bias uncertainty at low applied loads. The mean error becomes the conservative load cell bias error. This method yields an approximate load cell accuracy error of 10% of the applied force. This error is most likely conservative and predicts load cell behavior in the laboratory environment more accurately than the manufacturer's specification.

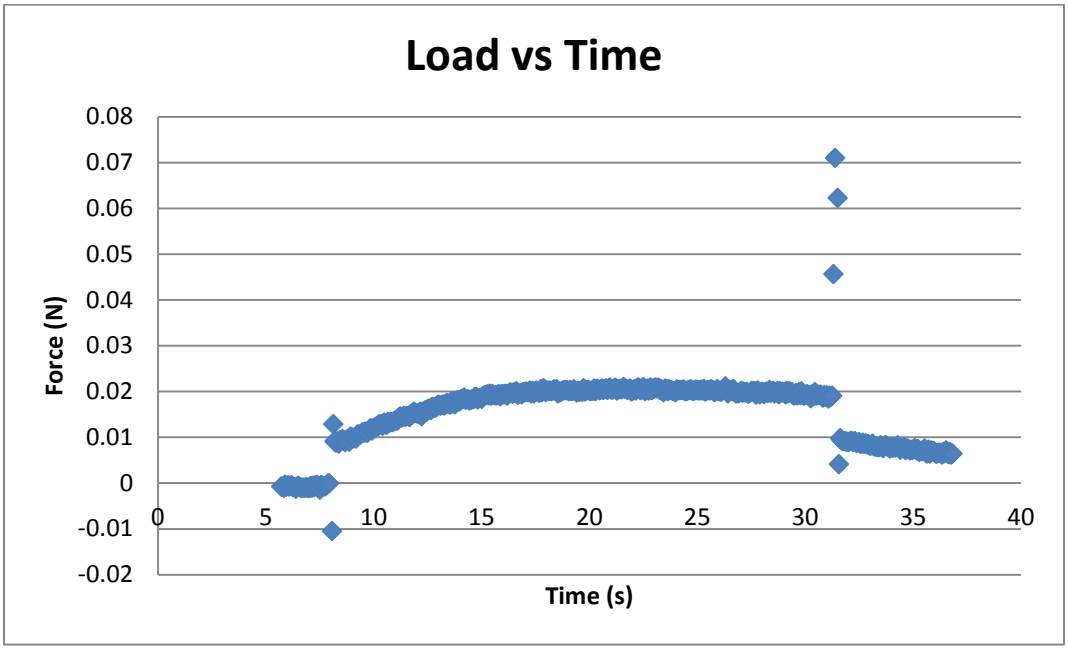

Figure 25: Load Cell Calibration Data

The following uncertainty terms are provided by the pressure transducer manufacturer. As stated in the previous section, the full-scale pressure of the transducer used is 500 psig.

Table 7: Manufacturer Pressure Transducer Uncertainty

Uncertainty Term	Limit Value	Error Magnitude (PSI)	Uncertainty Type
Accuracy	0.5 (% Full Scale)	2.5	Bias
Non-Linearity and Hysteresis	0.5 (% Full Scale)	2.5	Bias
Non-Repeatability	0.1 (% Full Scale)	0.5	Bias
Temperature Effect	.02 (% of Reading/^{o}F)	Reading Dependent	N/A

Like the load cell, the manufacturer's uncertainty in accuracy and non-linearity/hysteresis is too great a percentage of the expected measured pressure values. Therefore, the transducer was re-calibrated and linearity and accuracy were confirmed at pressures between 0 and 65 PSI. In this range, the maximum error was approximately 0.5 PSI. This error is used in place of the manufacturer's error because it more accurately reflects the behavior in the laboratory environment. Because the error offset is a constant magnitude, the error as a percentage of applied pressure is calculated individually for each run as follows.

$$U_{B,P} = \frac{0.5\ (PSI)}{P_{measured}\ (PSI)}\ X\ 100 \tag{50}$$

Like the load cell, it is assumed that this accuracy error is the sum of all bias errors associated with the pressure transducer. Therefore, it is used as the total accuracy error in the pressure transducer.

The error associated with measurement of the cross-sectional throat area is not provided by the manufacturer but is instead calculated based upon perceived uncertainty in the measurement process. During measurement, a repeatability error of approximately 0.0005-in was approximated. This is considered a bias error. The bias uncertainty in area is calculated from the perceived error in diameter measurement as follows where D_M is the measured diameter.

$$U_{B,A} = \frac{(D_M^2 + D_U^2) - D_M^2}{D_M^2} \times 100 \tag{51}$$

The total bias uncertainty is calculated by taking the root sum of the squares of the force, pressure and area bias uncertainties in accordance with the methods of Beckwith, Marangoni and Lienhard [27].

$$U_B = \sqrt{U_{B,F}^2 + U_{B,P}^2 + U_{B,A}^2} \tag{52}$$

In general, the experimental precision uncertainty is calculated using the methods of Beckwith, Marangoni and Lienhard [27]. The 95% precision uncertainty combines the standard deviation of the steady state sample size with the number of samples and a t-distribution factor to determine the uncertainty in the experimental mean as follows. Note that, by dividing by the mean value of the variable in question, the precision uncertainty, like the bias uncertainty, is a percentage of the measured value.

$$U_P = \frac{t_{\alpha/2}\ S_x}{\bar{x}\sqrt{n}} \times 100 \tag{53}$$

In this study, the sample size of all data populations in question is greater than thirty. Therefore, the t-distribution factor is a constant defined as follows.

$$t_{\alpha/2} = 1.96\ (95\%\ Confidence)$$

There are precision uncertainty terms associated with the measured load, measured pressure and measured load offset. Therefore, the total precision uncertainty is calculated as the root sum of the squares of these three terms. There is no precision uncertainty associated with the throat area measurement, as all uncertainty in this variable is captured in the bias.

$$U_P = \sqrt{U_{P,F}^2 + U_{P,P}^2 + U_{P,O}^2} \tag{54}$$

In accordance with the methods of Wheeler and Ganji, the total experimental uncertainty is determined by taking the root sum of the squares of the total bias and precision uncertainties [26]. This total uncertainty is a percentage of the total thrust coefficient.

$$U_T = \sqrt{U_P^2 + U_B^2} \tag{55}$$

As mentioned earlier, this is a conservative uncertainty. The bias errors contribute to the precision uncertainty in the sample population. Therefore, they are considered multiple times indirectly. Likewise, the sample mean is used to calculate the percent error in the bias uncertainty, propagating this uncertainty back into the bias. However, given that these error terms are not directly related, it is most appropriate to calculate the total error as though the bias and precision uncertainties are decoupled. This provides a conservative, yet reasonable error estimation.

It is important to note that, although Equation 47 includes the ion gauge pressure and measured exit area to calculate a correction to vacuum thrust, the magnitude of this correction, coupled with the low uncertainty magnitude of both of those measured

quantities make this error insignificant in comparison to the total uncertainty outlined in this section. Therefore, any uncertainty in vacuum chamber pressure and nozzle exit area is considered inconsequential and is compensated for in the conservative nature of these uncertainty calculations.

Additionally, there is undoubtedly an uncertainty associated with calculation of the throat Reynolds number based on the mass flow and gas temperature. In fact, the mass flow controller manufacturer claims that use of the gas correction factors outlined previously in this chapter limit the accuracy of the controller to 15% of the displayed flow rate [24]. This uncertainty dominates the uncertainty in Reynolds number. However, because exact knowledge of the Reynolds number is not necessary in investigating trends over the range investigated, error bars are not included for this variable and an exact uncertainty for each measurement is not necessary. Instead, it is assumed that all Reynolds numbers investigated carry an uncertainty of between 15 and 20%.

The remainder of this section outlines the calculation of the total error in the thrust coefficient associated with a test of the D15-20 nozzle at a Reynolds number of 5000. First, Table 8 outlines the bias uncertainties associated with the load cell, pressure transducer and throat area.

Table 8: Example Experimental Bias Uncertainty Terms

Bias Uncertainty Term	Max Error Magnitude (N)	Uncertainty (% Reading)
Load Cell Bias	N/A	10

Pressure Transducer Bias	0.5 (PSI)	2.84
Throat Area Uncertainty	N/A	5.65
Total Bias Uncertainty		11.83

The precision errors associated with the force, offset and pressure calculated from the standard deviation of the sample population are listed in the table below.

Table 9: Example Experimental Precision Uncertainties

Precision Uncertainty Term	Precision Uncertainty (% Reading)
Thrust Standard Error	0.42
Offset Standard Error	1.45
Pressure Standard Error	0.01
Total Precision Uncertainty	1.5

The total uncertainty in the calculated thrust coefficient combines the precision and bias uncertainties.

$$U_T = \sqrt{U_P^2 + U_B^2} = 11.92\% \ (95\% \ Confidence)$$

IV. Results

This chapter details the results of the analytic and experimental research phases described in Chapter 3. Results are broken down into four primary sections: roughness analysis, analytic model results, experimental results and implications. The roughness analysis was conducted to provide an accurate estimate for the roughness profiles used in the analytic model. The analytic model results provided a baseline for comparison to the experimental results.

4.1 Roughness Analysis

The roughness analysis was performed to objectively characterize the surface roughness variations between the DMLS and machined nozzles used in this research. Although there appears to be a large disparity between the surface finishes of the two nozzle varieties when viewed with the naked eye, further investigation shows a more ambiguous distinction. Figure 26 provides an exaggerated example roughness profile with major variables of interest labeled to aid in the objective comparison of the two surface finishes.

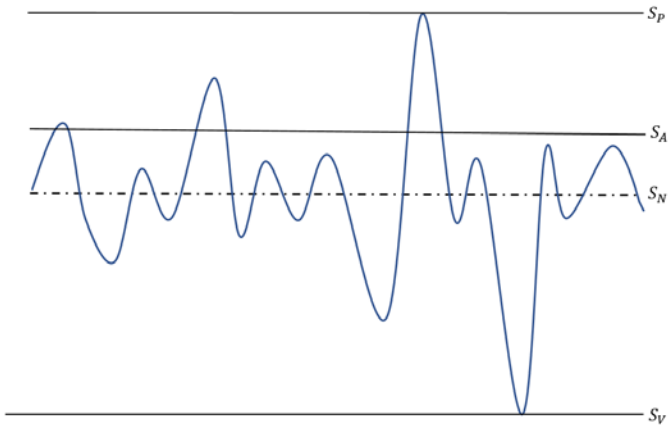

Figure 26: Roughness Parameter Example

First, it is important to define the various roughness values presented in this section. Referencing Figure 26, the mean, or nominal, surface height is represented by the symbol S_N. Meanwhile, the average surface roughness or S_A, represents the mean of the absolute value of the heights of individual surface points with respect to the nominal value. This definition adopts the convention of the manufacturer of the laser scanning microscope used to measure the roughness [28]. Finally, S_z is the maximum height, and is the sum of the absolute values of the maximum peak, S_P, and valley, S_V, in the measured area as shown in Equation 56.

$$S_Z = S_P + |S_V| \tag{56}$$

Often, when considering the roughness of a manufactured part, the variable R_A is used to represent the mean roughness of the material. However, R_A measurements are only taken over a straight line of the surface. Meanwhile, the average surface roughness, S_A, provides a more complete picture of the roughness by averaging multiple linear R_A measurements over a selected surface area [28].

Figure 27 is an image of a three-dimensional mapping of the cross-section of an additively manufactured nozzle. Large anomalies in the surface profile occur on irregular intervals as shown in the figure. Because of the spacing between anomalies, there is reasonable probability that any one profile measurement will miss an anomaly and underestimate the roughness of the area in question. Measuring S_A rather than R_A decreases the likelihood of a missed anomaly. Another important note in Figure 27 is that the three-dimensional surface mapping shows a significant difference between the

average surface roughness and the maximum roughness height. The implications of this difference are discussed later in this section.

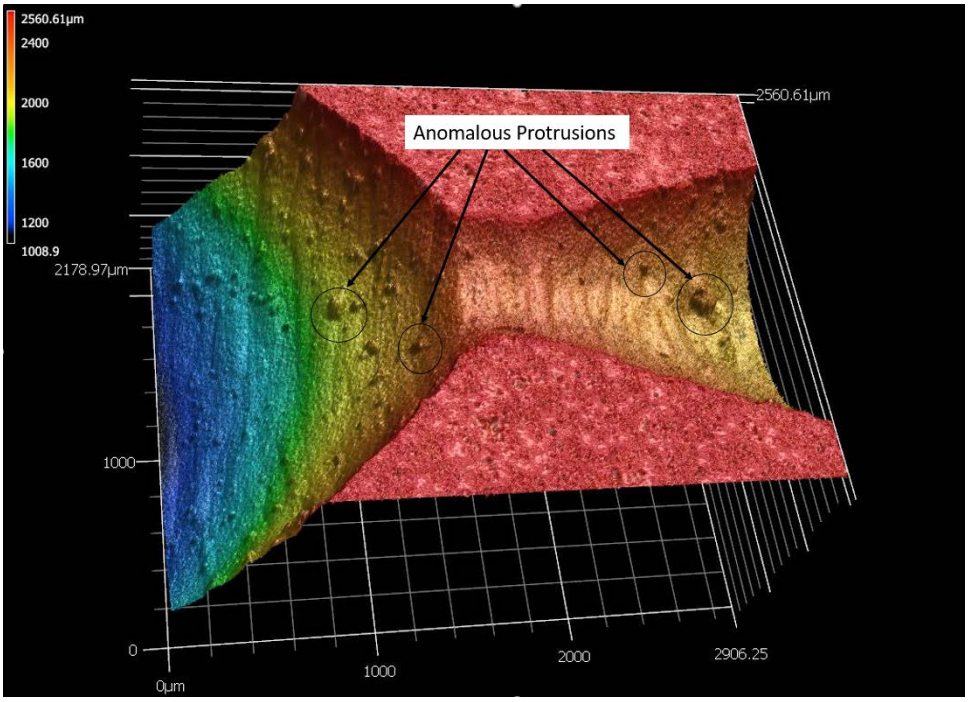

Figure 27: 3-D Mapping of Nozzle Cross-Section

Three nozzles were measured to determine the average roughness profiles of the DMLS and EDM nozzles. The three-dimensional images were flattened to a profile representing the nominal surface height. This allowed for the measurement of both the average and maximum surface roughness heights. Figure 28 is a flattened image of the nozzle cross-section and shows the surface areas sampled to provide the average roughness values for the first DMLS nozzle. Roughness sample areas were taken in the chamber, convergent, throat and divergent sections of the DMLS nozzles. The EDM nozzles were not sectioned. Therefore, roughness measurements were taken at multiple areas in the convergent section of the nozzle.

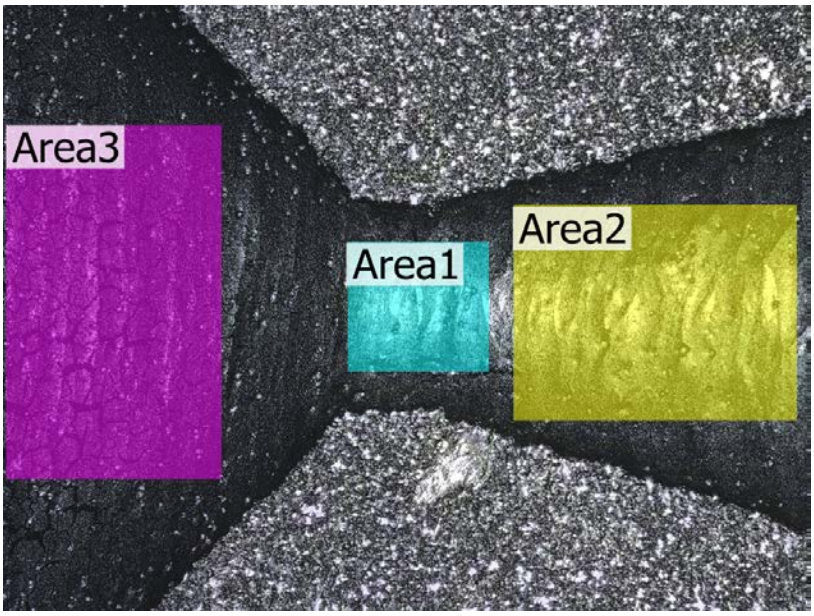

Figure 28: Measurement Areas in DMLS Nozzle

Table 10 provides a comparison of the roughness measurements taken for the two types of nozzles. The DMLS measurements are averaged over all area samples for two nozzles. The roughness values for the EDM nozzle are averaged over the two surface areas measured within the convergent section of the nozzle. The third parameter in the table is the absolute roughness, ε, required to solve for the friction factor. The calculation of this variable is detailed later in this section. The measurements for each nozzle and area are provided in Appendix A.

Table 10: Experimental Nozzle Roughness

Nozzle Type	**S_A (µm)**	**S_Z (µm)**	**ε (µm)**
EDM	6.3	66.4	36.8
DMLS	7.3	102.5	43

The first result of note is that there is only a 14% difference in the average surface roughness of the DMLS nozzles when compared to the EDM nozzle. Although the maximum height of the surface roughness in the DMLS nozzles, S_Z, is 35% larger than that of the EDM nozzle, these anomalous protrusions occur in low densities. Therefore, they have little effect on the average surface roughness of the surface profile. This result supports Krishnamurty's suggestion that defining an average surface roughness does not capture the true roughness profile of surfaces with distinct roughness features dispersed throughout the population [15]. This discrepancy poses a problem when quantifying the absolute roughness of the nozzle surface as required for calculation of the friction factor in the analytic model.

Research by Adams, Grant and Watson compared the efficacy of using the maximum roughness height in place of the average roughness height when calculating the absolute, or sand-grain, roughness [29]. The authors suggest that maximum roughness height may be more accurate in calculating the absolute roughness. However, inconsistency in measurement of S_Z led to conflicting experimental results when examining its use in determining the absolute roughness of the surface [29].

Additionally, use of the maximum height as the absolute roughness for the nozzles in this experiment would suggest that the additively manufactured nozzles exhibit the roughness of asphalted cast iron, with the EDM nozzles falling somewhere between wrought iron and asphalted cast iron per Moody's original sand-grain roughness definitions [22]. This would be a clear overestimation of the absolute roughness. Therefore, an alternate method to determine absolute roughness is needed.

Although Adams et al. found that use of the average roughness as the absolute roughness underpredicted the experimentally measured values, they found that use of a correction factor significantly increased the accuracy of this method. In their study, they used an algorithm to determine that Equation 57 may be used to provide an estimate of absolute roughness when given average surface roughness [29]. Because the average surface roughness is a mean profile roughness, they are used interchangeably in this research.

$$\varepsilon = 5.863R_a = 5.863S_A \tag{57}$$

Table 10 contains the absolute roughness of both the EDM and DMLS nozzles as calculated using Equation 57. These absolute roughness profiles place both nozzles near that of wrought iron or commercial steel in accordance with Moody's definitions [22]. This estimation is more appropriate than that formulated using the maximum height. However, the absolute roughness values of the machined and DMLS nozzles are nearly indistinguishable from one another. This suggests that any discrepancies between the performance of the EDM and DMLS nozzle in the experimental environment are likely driven by more complex compressible flow mechanisms than those incorporated in the analytic model described in the next section. These alternate mechanisms will be explored in the final section of this chapter.

4.2 Analytic Model Results

Prior to completion of the experimental phase of this research, the analytic model described in Chapter 3 was used to predict the effects of surface roughness on the thrust coefficient of nozzles like those tested experimentally. Before the experimental nozzle

roughness was analyzed, as described in the previous section, the model was run over a variety of experimentally plausible flow conditions to determine the losses expected in a nominally smooth nozzle. This nozzle was estimated to have an absolute roughness of 1.6 microns, corresponding closely to the absolute roughness of drawn tubing presented by Moody [22]. The analytic model covered flow conditions resulting in throat Reynolds numbers ranging from 500 to 25000 with nitrogen as the propellant gas and a nozzle with a 0.022-inch throat diameter and a 20° expansion half angle. This throat diameter was chosen because it falls approximately halfway between the two nominal throat diameters tested experimentally. Figure 29 is a plot of the thrust coefficient against expansion ratio for this test case in the style of the plots that Spisz produced in his original work [4].

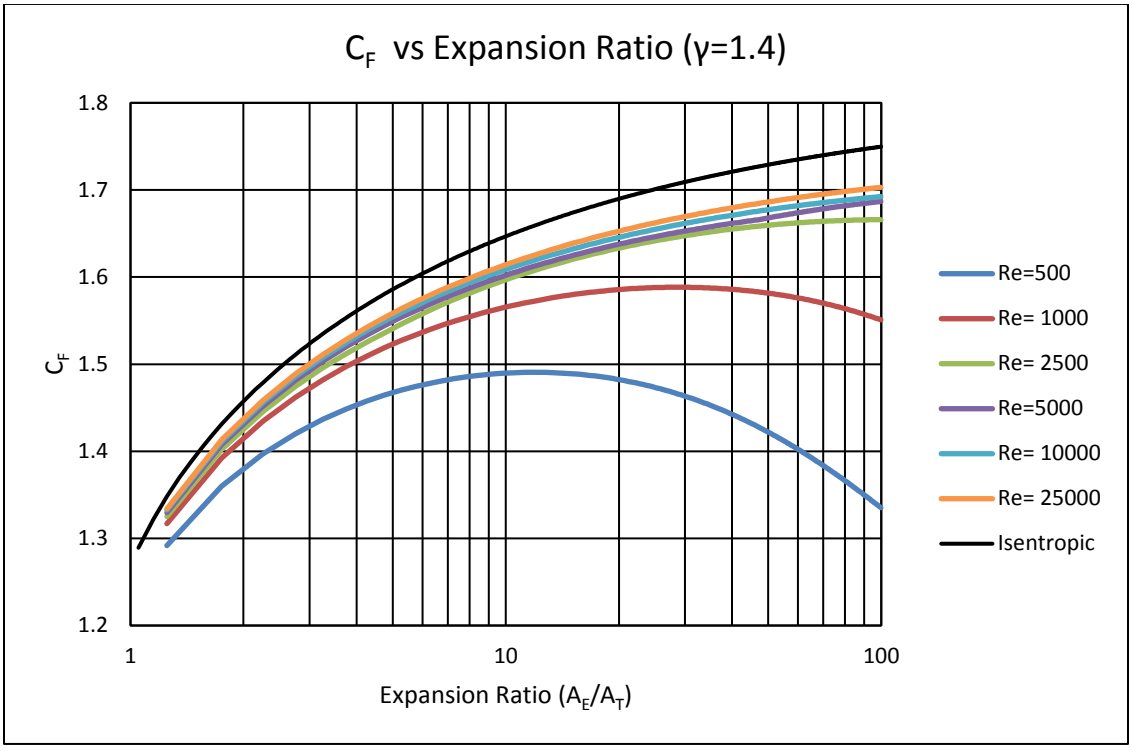

Figure 29: Thrust Coefficient in 0.022-in Throat Diameter Nozzle (ε=1.6 μm)

Figure 29 shows a clear decrease in thrust coefficient when compared to isentropic expectations over all Reynolds numbers. As described in Chapter 3, Reynolds numbers below 2000 were considered fully laminar. Therefore, the Re=500 and Re=1000 lines are independent of surface roughness. Still, it is predicted that viscous losses are maximized in this laminar regime. Losses are still present in the transitioning and fully turbulent regimes; however, the thrust coefficient losses are much less dependent upon Reynolds number across the range of expansion ratios investigated.

Spisz also suggested the alternative method of representing these results as thrust coefficient losses when compared to isentropic expectations as a function of throat Reynolds number and expansion ratio [4]. The primary benefit of this method is that it allows for investigation of the subtle differences in expected losses at fully turbulent Reynolds numbers. Figure 30 is a plot of the thrust coefficient losses for the same nozzle and flow conditions used in Figure 29.

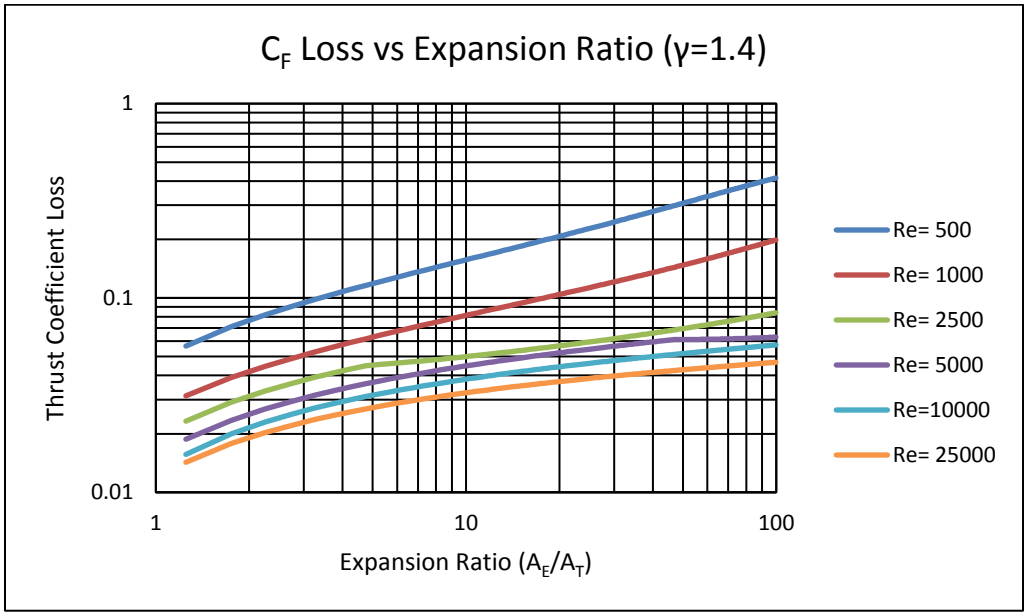

Figure 30: Thrust Coefficient Losses in 0.022-in Throat Diameter Nozzle (ε=1.6 μm)

Figure 30 once again indicates that losses are maximized at low Reynolds numbers and that, although viscous losses are expected to decrease with increasing turbulent Reynolds numbers, these loss terms are far less dependent upon Reynolds number in the turbulent regime over the range of expansion ratios studied. For instance, the difference in the loss terms between Reynolds numbers of 5000 and 10000 is less than 0.01 at an expansion ratio of 30.

The case of the throat Reynolds number of 2500 shows an interesting side effect of the choice of a Reynolds number of 2000 as the transition from fully turbulent to fully laminar flow. At low expansion ratios, it exhibits behavior more closely related to the fully turbulent test cases. This is because the flow reaches a turbulent Reynolds number at the throat and remains turbulent through the exit plane of the nozzle. However, at higher expansion ratios, the behavior profile more closely mirrors the laminar flow Reynolds numbers. This is because, for these test cases, viscous losses are building in the expansion cone, causing the Mach number to decrease, and, ultimately, causing the flow Reynolds number to decrease. With a long enough expansion cone, the flow will transition back to laminar flow prior to exiting the nozzle.

Because of difficulty in predicting the transition region between fully laminar and fully turbulent flow, this behavior will be exhibited in any flow conditions that exhibit both laminar and turbulent flow at different points in the thruster geometry. It is acknowledged that the lack of a transition region in the model oversimplifies the dynamics of the flow. However, this estimation is unavoidable to obtain a closed form solution. Ultimately, it was decided to keep the estimate of transition to fully turbulent flow at a Reynolds number of 2000 because it allows the model to consider the effects of

surface roughness over a larger range of Reynolds numbers. Experimental results, as described in the next section, support the conclusion that surface roughness plays a role in performance losses at throat Reynolds numbers at least as low as 2500.

After the results of the roughness evaluation were collected, the same test conditions above were run with the absolute roughness adjusted to match those of the experimental machined and DMLS nozzles. Additionally, the expansion half angle was adjusted to 15° to match those of the experimental nozzles. A nominal throat diameter of 0.022-in was still used to provide an estimate of behavior across all nozzle throat diameters. Analytic curves for nozzle geometries closely matching those of the experimental nozzles are provided later in this chapter for comparison to experimental results and in Appendix B. Figure 31 provides the same comparison as Figure 28 with the stated changes considered.

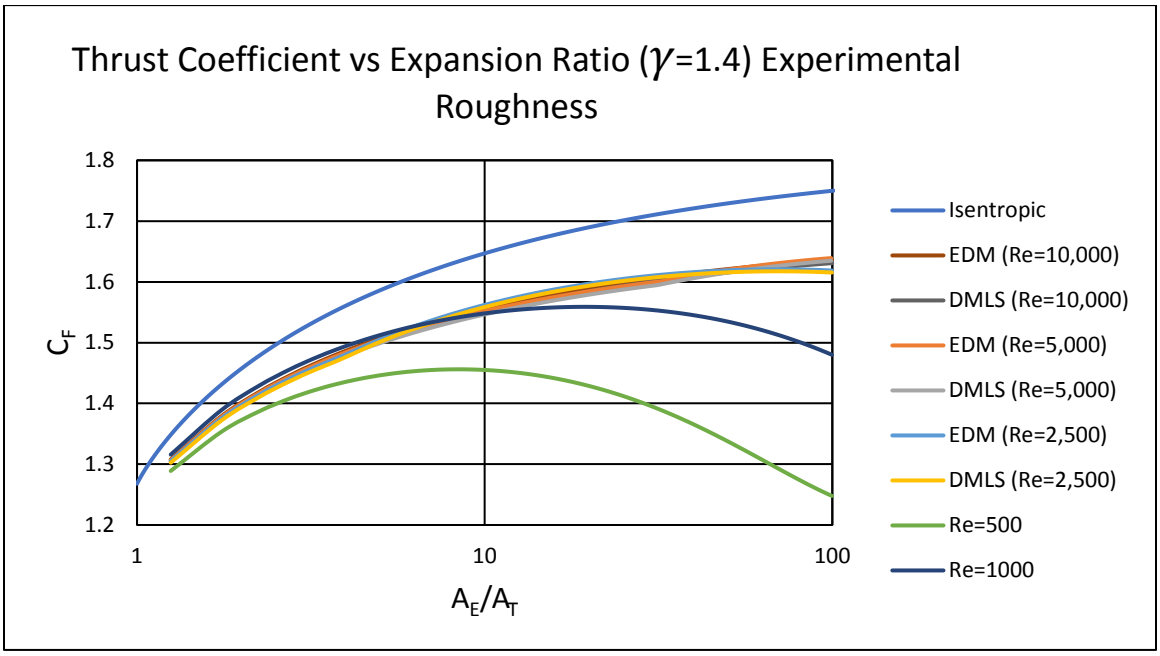

Figure 31: C_F in 0.022-in Throat Diameter Nozzle (Experimental Roughness)

Figure 31 shows that the analytical thrust coefficient is nearly identical for the EDM and DMLS nozzles. This is expected because of the similarity of their experimental absolute roughness values. In the plots comparing the analytic and experimental results, only the DMLS analytic data is presented to enhance chart clarity. Figure 32 is a plot of loss in thrust coefficient for the test case in Figure 31 and allows for better comparison of the impact of throat Reynolds number on expected performance.

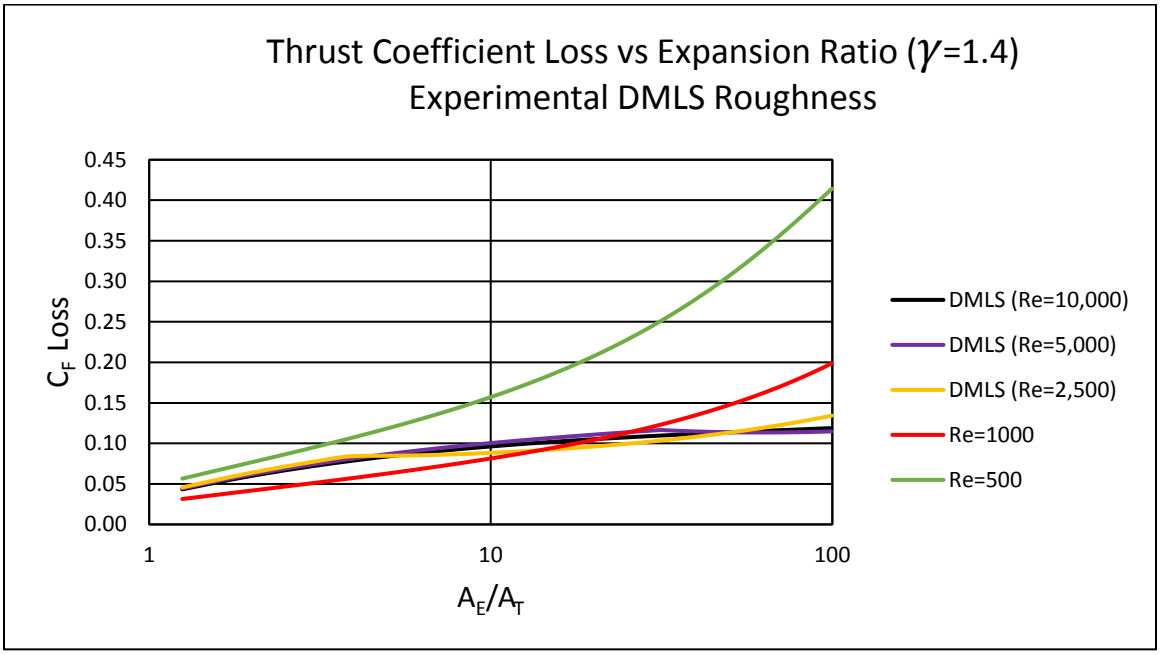

Figure 32: C_F Loss in 0.022-in Throat Diameter Nozzle (DMLS Roughness)

Figure 32 shows that, at low expansion ratios, flows at Reynolds numbers between 1000 and 2500 reduce losses in thrust coefficient due to viscous effects when compared to flows with throat Reynolds numbers considered to be fully turbulent. This suggests that, because the relative roughness of the experimental nozzles is high, it is advantageous to maintain flow in the upper range of laminar throat Reynolds numbers where viscous losses are minimized for laminar flow.

At fully turbulent Reynolds numbers, thrust coefficient losses are very similar over the range of expansion ratios investigated. In fact, at the experimental roughness investigated, the losses are nearly indistinguishable at throat Reynolds numbers of 5000 and 10000. This behavior is in line with the impact of relative roughness on friction factor as a function of Reynolds number in accordance with Moody's original theory and is best exemplified by a modified Moody diagram of Darcy friction factor versus Reynolds number as shown in Figure 33 [22].

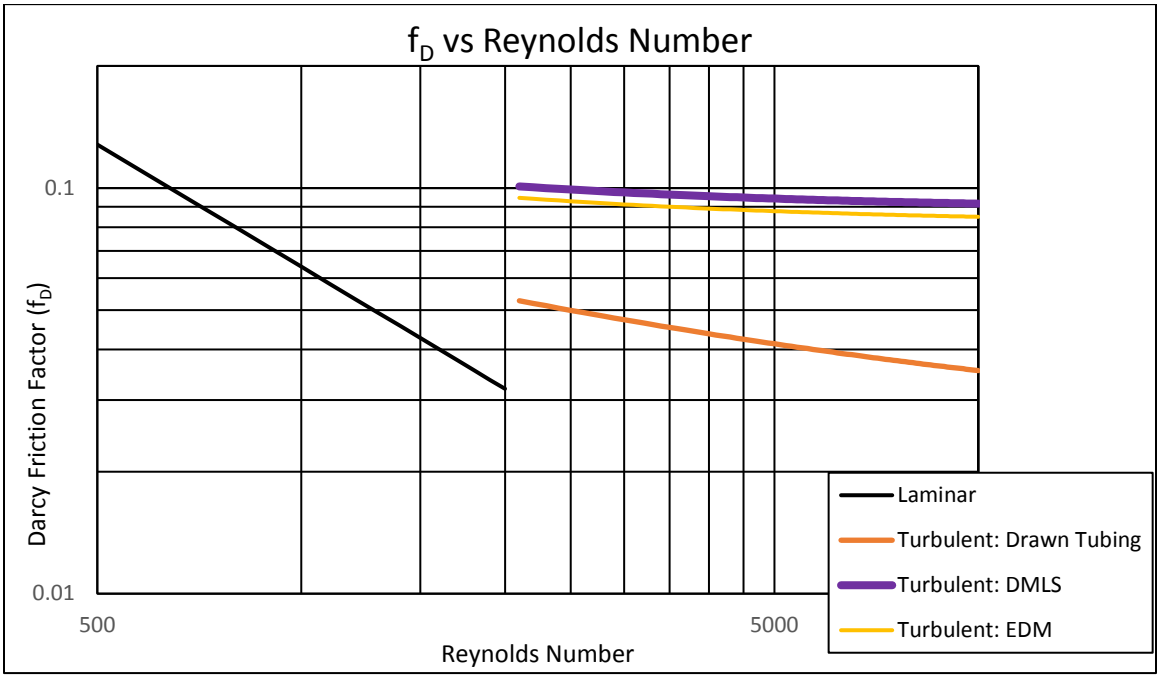

Figure 33: Friction Factor vs Reynolds Number for Varying Relative Roughness

Figure 33 clearly shows that for the experimental nozzles, the friction factor varies by less than 10% between the turbulent Reynolds numbers evaluated experimentally (2500-10000). It also shows, once again, that the characteristics of the EDM and DMLS nozzles are nearly indistinguishable from an analytic perspective.

Combining these results with those of Figures 31 and 32 suggests that nozzle

surface roughness differences between these manufacturing styles will not result in significant discrepancies in thruster performance. Experimental investigation in the next section evaluates this expectation against empirical data.

Figure 33 also raises two concerns over the methods used to develop the dynamics of the analytic model. First, the Darcy friction factors for the experimental nozzles exceed the maximum limits in Moody's original research [22]. Therefore, it is possible that, at these extremely high relative roughness values, the correlations used to develop the friction factor are less accurate. Additionally, if the laminar region were assumed to continue up to a Reynolds number of 4000, the friction factor would be nearly an order of magnitude lower at these Reynolds numbers than that predicted using 2000 as the laminar flow cut-off. These factors must be taken into consideration when evaluating the experimental data collected against the analytic results.

Plots of thrust coefficient as a function of expansion ratio and Reynolds number for all cases investigated experimentally form the basis of comparison used in the next section. These analytic plots are included in Appendix B. Because the expectations for the DMLS and EDM nozzles are nearly identical, these plots only include one experimental roughness term to aid in chart readability. This roughness term uses the absolute roughness calculated for the DMLS nozzles.

4.3 Experimental Results

This section contains the results of the experimental objectives of this research. Additively manufactured and machined nozzles were tested over a variety of flow conditions to determine the effects of Reynolds number, expansion ratio, nozzle throat

diameter and nozzle surface finish on the performance of micro-thrusters. Due to constraints of the experimental apparatus encountered during testing, the following limitations in scope were established:

1. Due to flow limits and accuracy of the mass flow controller, throat Reynolds numbers of 500 and 1000 were only reachable using helium as the propellant gas.

2. Throat Reynolds numbers of 2500 to 10000 were only tested using nitrogen and carbon dioxide because the ambient pressure in the vacuum chamber increased too rapidly at the mass flow rates required of helium, leading to a high probability of flow separation within the nozzle.

3. Resistance heater output limited the heater block temperature to between 500 and 650 degrees Fahrenheit. Because of this initial gas temperature, expansion ratios above 40 could not be tested for the 0.030-inch (nominal) throat diameter nozzles. The associated temperature drop during expansion for these nozzle variations created the likelihood of phase change in the flowing gas.

4.3.1 Laminar Flow Experimental Results

The first experimental results to investigate are those for low throat Reynolds number tests completed with helium as the propellant gas. Although, in keeping with the definitions in Chapter 2, all experimental flow cases are low Reynolds number flows, in this chapter, low Reynolds number flow cases are those that are likely, from an analytic perspective, to maintain laminar flow at all axial points along the test thruster. It is acknowledged that, in an experimental environment, it is likely that this behavior is not fully laminar. These tests were conducted targeting Reynolds numbers of 500 and 1000.

Prior to presentation of the thrust coefficient and thrust coefficient loss results from these tests cases, it is important to acknowledge concerns associated with the data collection. First, because of the mass flow rates required to achieve the desired Reynolds numbers for heated helium, the vacuum chamber's inability to maintain vacuum becomes a source of potential error. According to Sutton and Biblarz, if the exit pressure of the

nozzle is between 10% and 40% of the ambient pressure, separation in the nozzle exit cone becomes likely [2]. This flow separation results in a decrease in thrust when compared to expectations for optimum expansion. For experimental tests with Helium, theoretically calculated exit pressures regularly fell below 40% of the measured ambient pressure in the vacuum chamber. Therefore, it is likely that flow separation contributed a loss in thrust and that viscous losses are not the only loss mechanisms.

In addition to the possibility of flow separation, difficulty in defining steady state operating and offset thrust data increased the uncertainty in the data compared to higher Reynolds number flow tests. Figure 34 is a graph of the raw thrust data for helium at a Reynolds number of 500 through a nozzle with an expansion ratio of 5. The final steady state thrust begins to decline prior to flow shut-off. Additionally, there is no highly discernible final offset as described in Chapter 3. These characteristics are likely due to the magnitude of thrust being measured and to flow disturbances, like separation, developing in the nozzle.

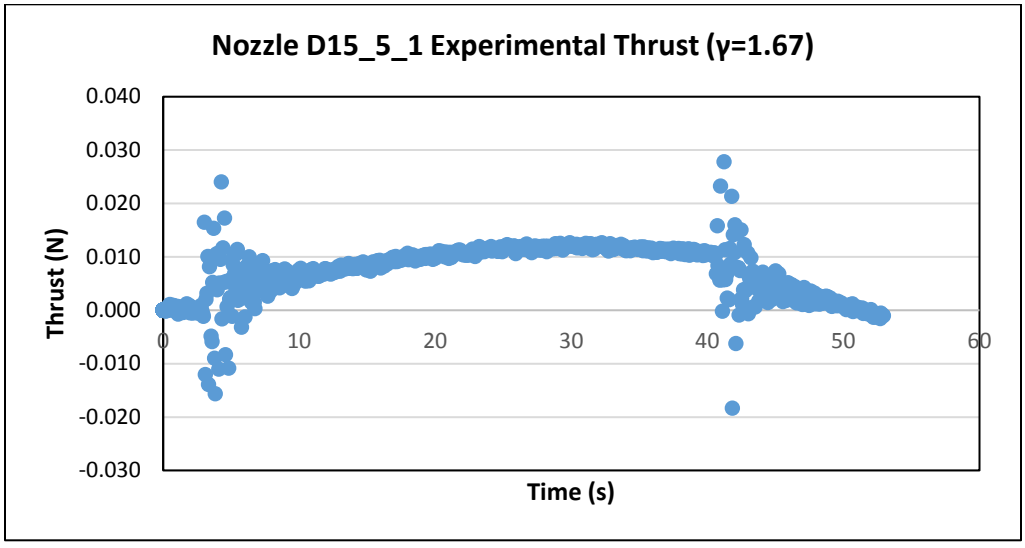

Figure 34: Typical Helium Thrust Data

Experimental data was collected for throat Reynolds numbers of 500 and 1000 for a variety of DMLS nozzles. Low expansion ratio nozzles were chosen for most tests to mitigate the risk of overexpansion, and therefore, separation of the flow within the expansion cone of the nozzle. Figure 53 is a plot of thrust coefficient as a function of expansion ratio for all nozzles targeting a throat Reynolds number of 500.

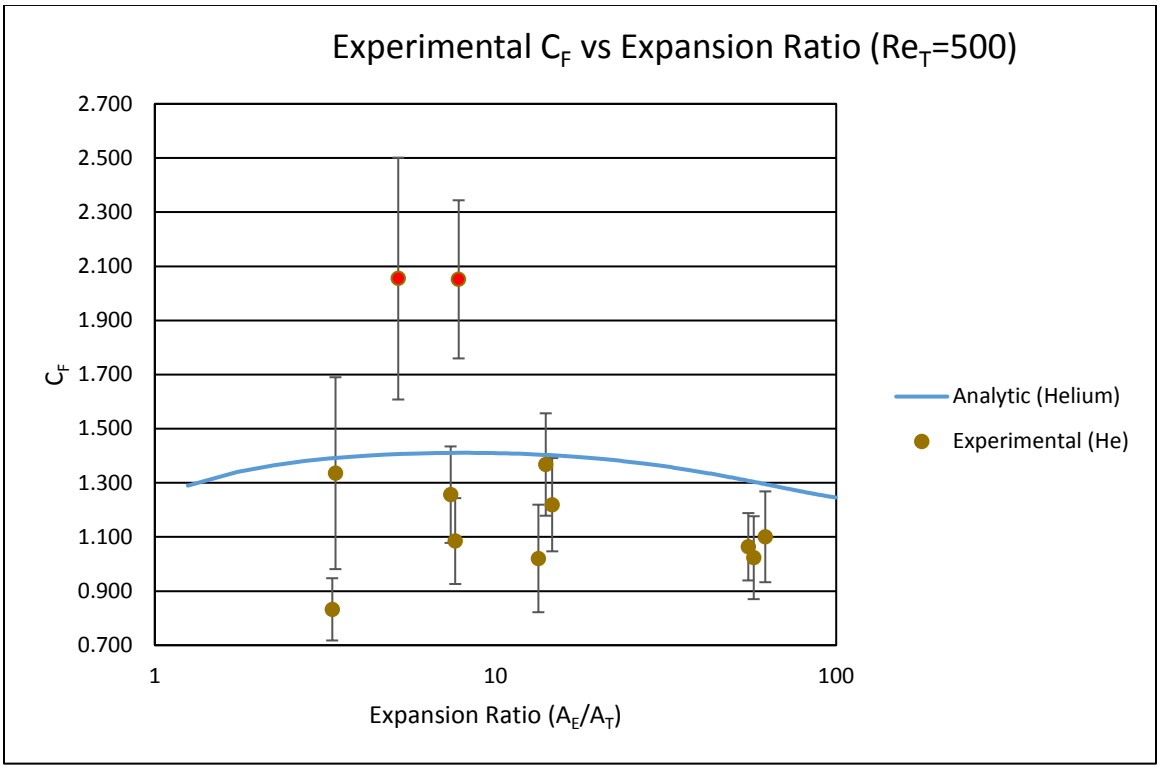

Figure 35: Re=500 Experimental C_F

Figure 35 clearly shows that the analytic prediction based on viscous losses formulated in the previous section overpredicts the performance of the experimental nozzles. The two data points highlighted in red exceed the theoretical expectations but the data used to formulate the thrust coefficients was irregular and it is expected that these data points are invalid.

Excluding these data points, the experimentally measured thrust coefficients averaged losses 2.5 times higher than those predicted by the analytic model. Also of note, over the spread of expansion ratios studied, there is little correlation between expansion ratio and measured thrust coefficient except at expansion ratios above 50 which see the highest loss terms as predicted by the analytic model. Figure 36 provides the same data represented as a loss in thrust coefficient.

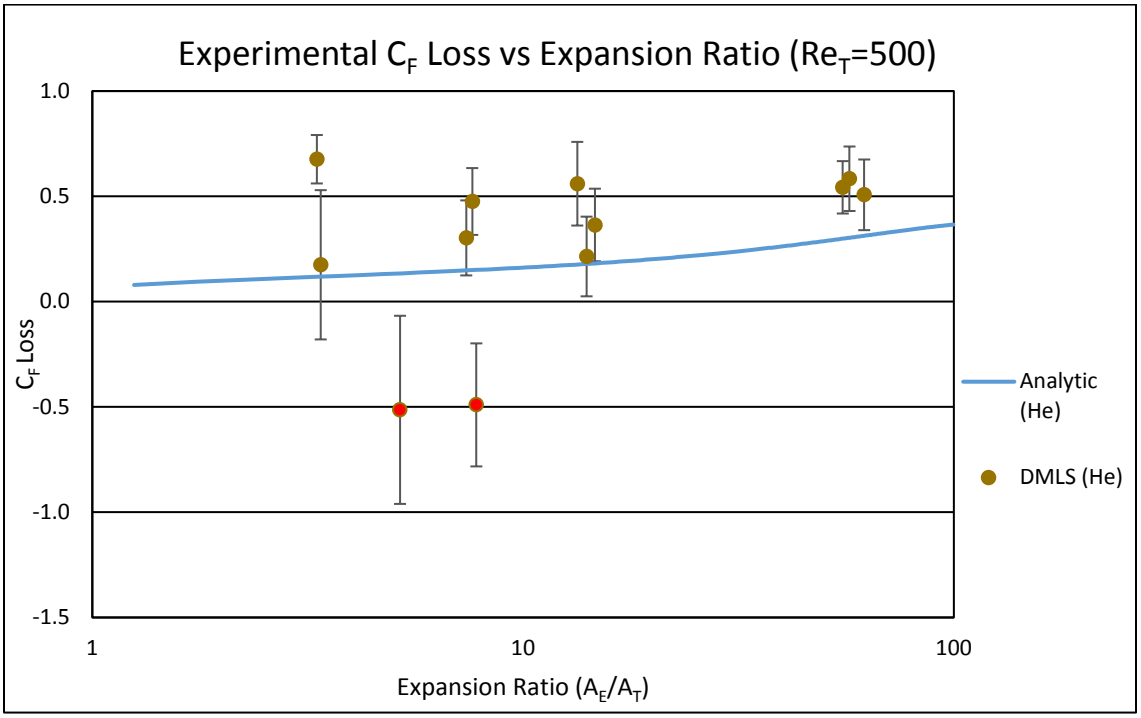

Figure 36: Re=500 Experimental C_F Loss

Experimental results for throat Reynolds numbers of 1000 also underperformed analytical expectations. Losses in thrust coefficient were 7 times higher than predicted by the analytic model. Measured thrust coefficients were of similar magnitude as those measured for the Re=500 tests. The analytic model predicts lower viscous losses, and therefore higher thrust coefficients, with increasing Reynolds number in the laminar

regime. Plots for the Re=1000 tests are provided in Appendix C. These results suggest that at fully laminar Reynolds numbers, losses in the DMLS nozzles are independent of Reynolds number and nearly independent of expansion ratio.

4.3.2 Turbulent Flow Experimental Results

This section presents the results of the experimental tests carried out with carbon dioxide and nitrogen as the tests gases. These gases were used to test at throat Reynolds numbers of 2500, 5000 and 10000 for a variety of machined and DMLS nozzles. The objectives of these tests were to compare the performance of the DMLS nozzles against that of machined nozzles and against analytic expectations.

The first case of interest under these test settings is the Re=2500 case. This case is expected to exhibit transitional flow behavior and was tested with two machined nozzles and six DMLS nozzles. The average throat diameter of the DMLS nozzles in this case is 0.018-inches and the average throat diameter of the machined nozzles is approximately 0.0225-inches. Therefore, the hydraulic diameters are similar enough that comparisons may be drawn between the performance of the nozzles. Figure 37 presents the experimentally measured thrust coefficients for these test cases. For comparison, third analytic line in Figure 37 is reconstructed from the analytic data from Spisz's original NASA research [4].

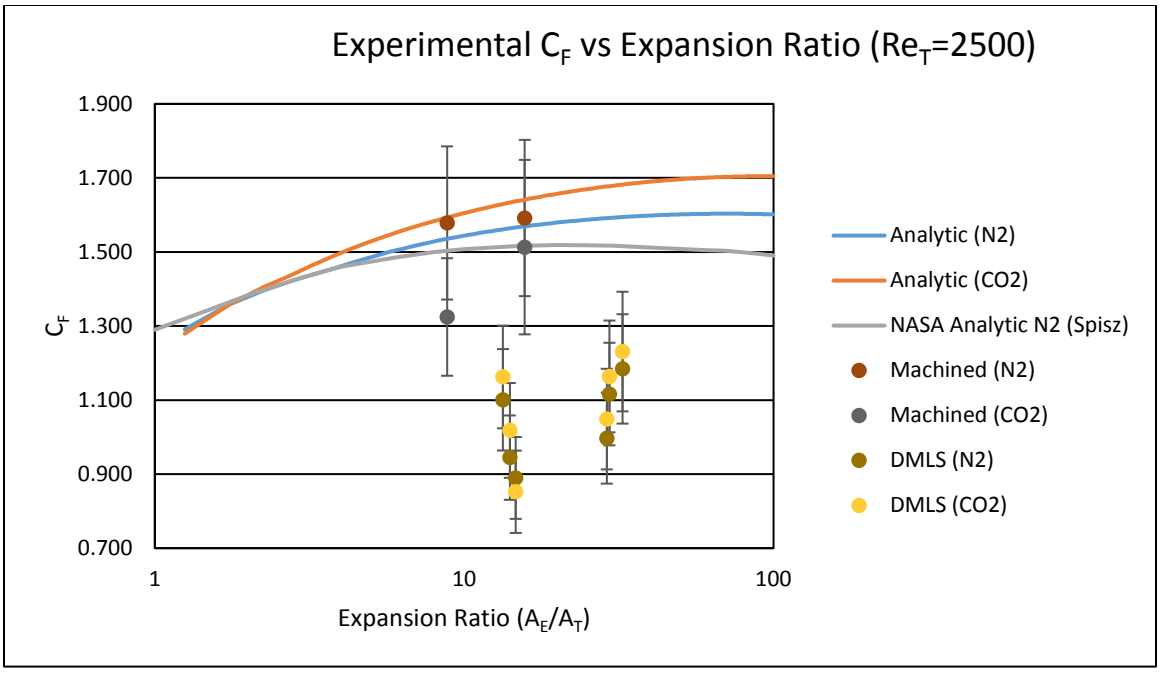

Figure 37: Re=2500 Experimental C_F

First, Figure 37 offers a clear distinction between the performance of the DMLS and machined nozzles. For both gases, the machined nozzles exceed the performance of the DMLS nozzles at similar expansion ratios. Additionally, for both machined nozzles, their respective analytic results are within, or very nearly within, experimental uncertainty of the measured values. All DMLS nozzles exhibit higher than expected losses well outside of the analytic expectations. The thrust coefficient shows a slight trend upward with increasing expansion ratio. A figure of the loss in thrust coefficient with respect to expansion ratio is included in Appendix C.

Experimental results for tests at Reynolds numbers of 5000 and 10000 for nozzles of these throat diameters with additional expansion ratios support the distinction in performance between machined and DMLS nozzles. However, the results do not show a clear trend with regards to expansion ratio. Figure 38 is a plot of thrust coefficient as a

function of expansion ratio for the Re=10000 case. In this case, it is also clear that the machined nozzles outperform the DMLS nozzles. However, the analytic expectations are well outside of the uncertainties in both cases. Therefore, the modeling of viscous effects in the analytic model is not sufficient to predict the performance of either nozzle type. Plots of all other results are included in Appendix C.

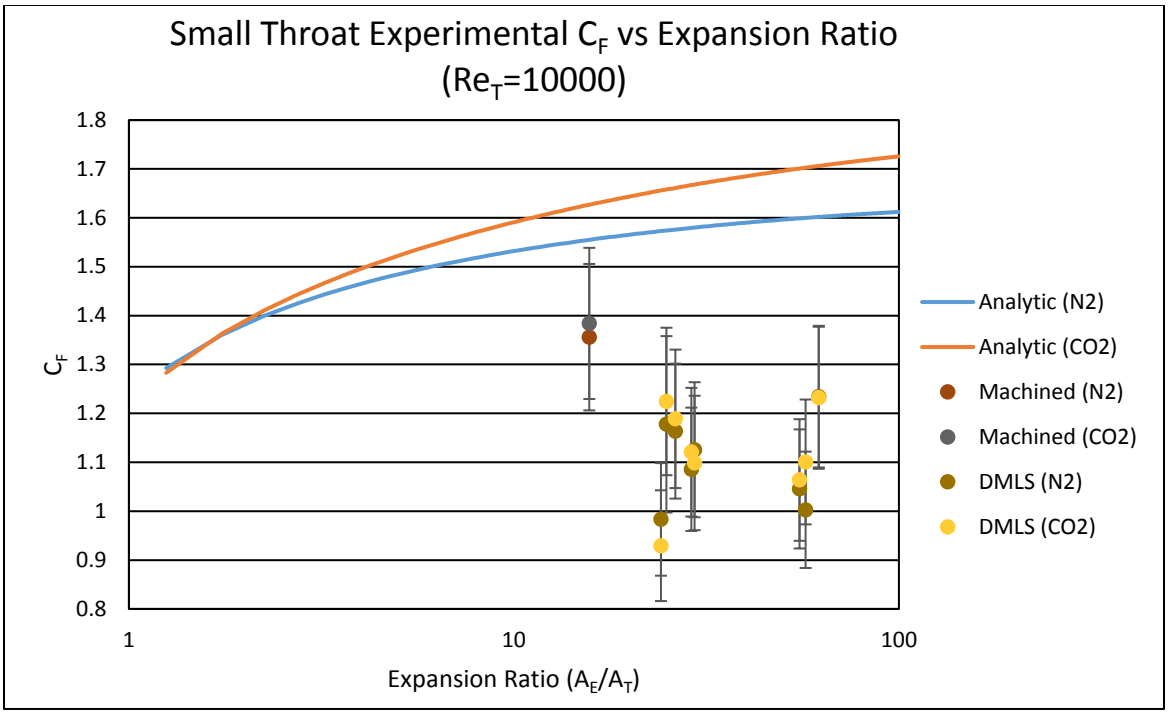

Figure 38: Re=10000 Experimental CF (Small Throat)

Additional tests at throat Reynolds numbers of 5000 and 10000 were conducted using DMLS nozzles with a nominal throat diameter of 0.030-inches. Increasing the throat diameter increases the hydraulic diameter of the throat and decreases the relative roughness of the orifice. Therefore, the analytic model predicts lower losses in performance due to viscous effects. Figure 39 is a plot of results for a Reynolds number of 10000 with the larger nozzle throat conditions.

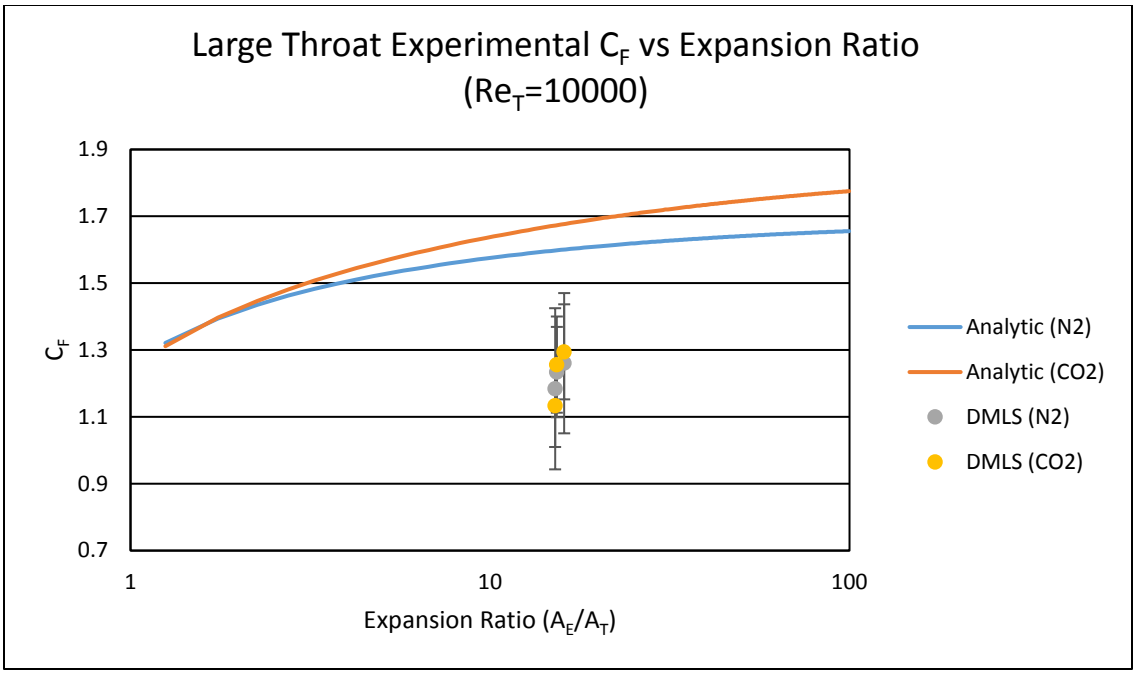

Figure 39: Re=10000 Experimental C_F (Large Throat)

Comparing the Re=5000 and Re=10000 experimental data for the small and large throat DMLS configurations shows that, although the analytic model still overpredicts performance per Figure 39, the experimental thrust coefficients are slightly higher in the large throat than in the small throat configurations at similar expansion ratios. This suggests that, although viscous loss terms are present, additional loss mechanisms unpredicted by the analytic model are likely driving performance loss. This theory is explained in detail in the final section of this chapter. Comparisons between the Re=5000 and Re=10000 tests cases are shown in Figures 40 and 41.

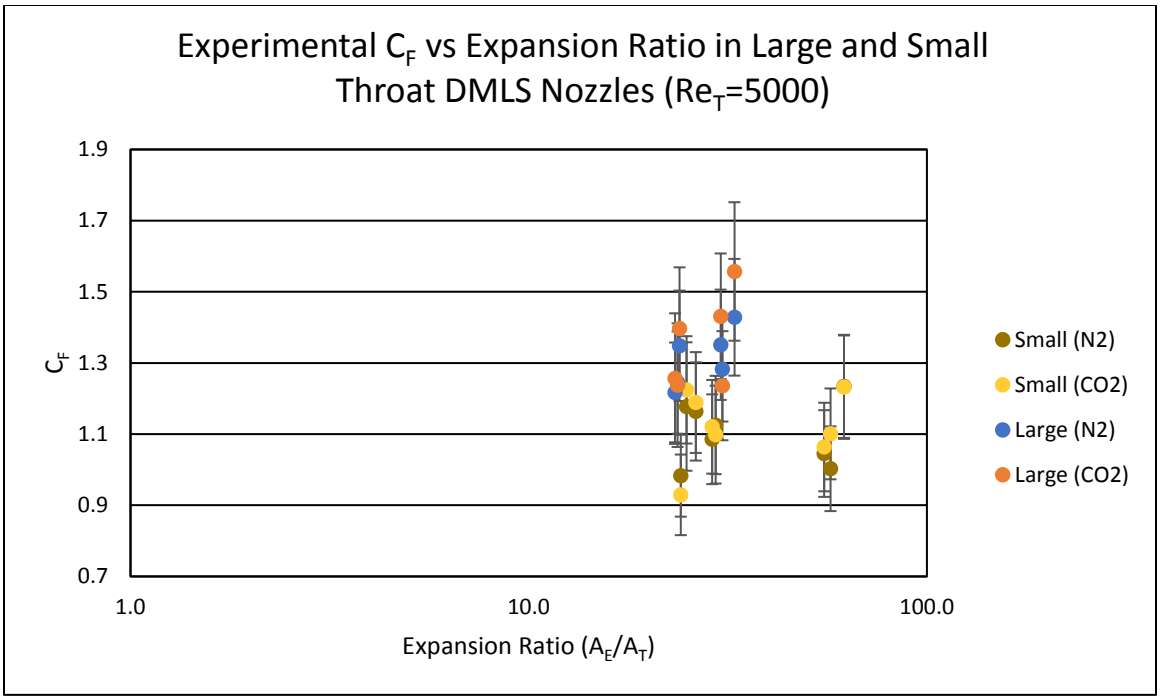

Figure 40: Performance Comparison Between Small and Large Throat Nozzles

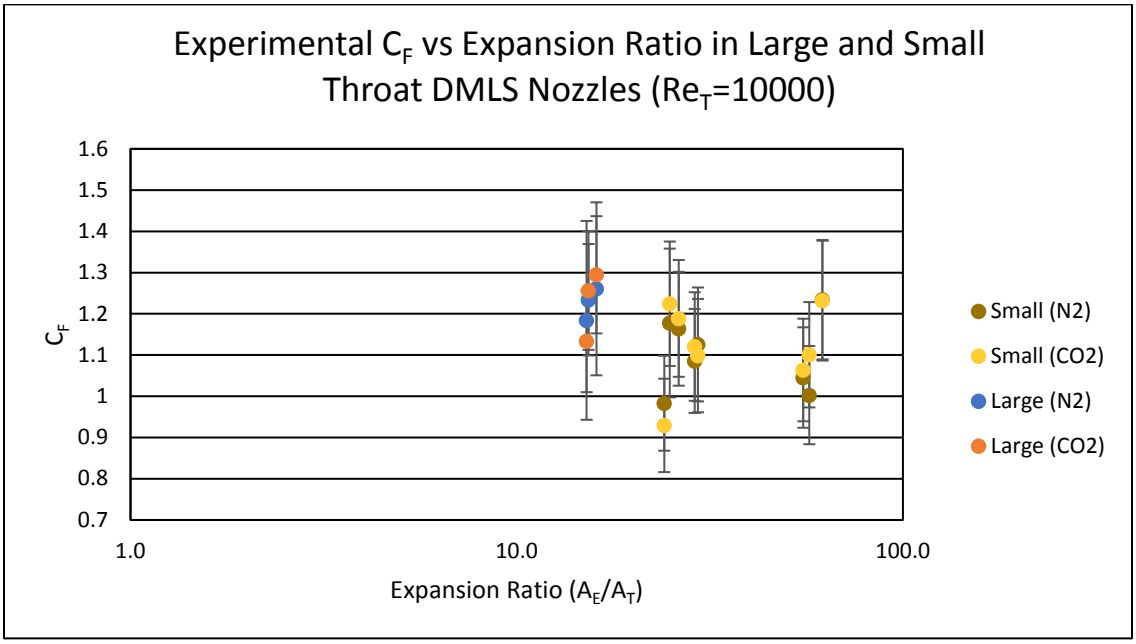

Figure 41: Performance Comparison (Re=10000)

4.4 Summary of Results

This section relates the results described in this chapter to the research objectives outlined in Chapter 1. First, the comparison between machined and additively manufactured nozzles is summarized. Simultaneously, the accuracy of the analytic model in predicting variations in thrust coefficient is addressed. Second, the effects of Reynolds number and expansion ratio on experimentally measured loss in thrust coefficient are investigated and compared to the analytic model. Additionally, explanations for any discrepancies between analytic and experimental results are presented.

4.4.1 Comparison of Machined and DMLS Nozzles

As discussed earlier in this chapter, the performance of DMLS and machined nozzles were compared at Reynolds numbers of 2500, 5000 and 10000. The absolute surface roughness of the two nozzle varieties was nearly indistinguishable when calculated using the average surface roughness. Therefore, the viscous losses predicted by the analytic model are nearly identical for the additively manufactured and machined nozzles.

However, experimental results showed a clear distinction between the performance of machined and DMLS nozzles of similar throat hydraulic diameters. Figure 42 plots the average experimentally measured percentage loss in thrust coefficient when compared to isentropic conditions for all three Reynolds numbers. Admittedly, because only two machined nozzles were manufactured, the sample size for the machined nozzles is much smaller than that of the DMLS nozzles. However, there is a very clear

delineation between the performance of the DMLS and machined nozzles. The DMLS nozzles average a 39% loss in thrust, while the machined nozzles average a 15% loss.

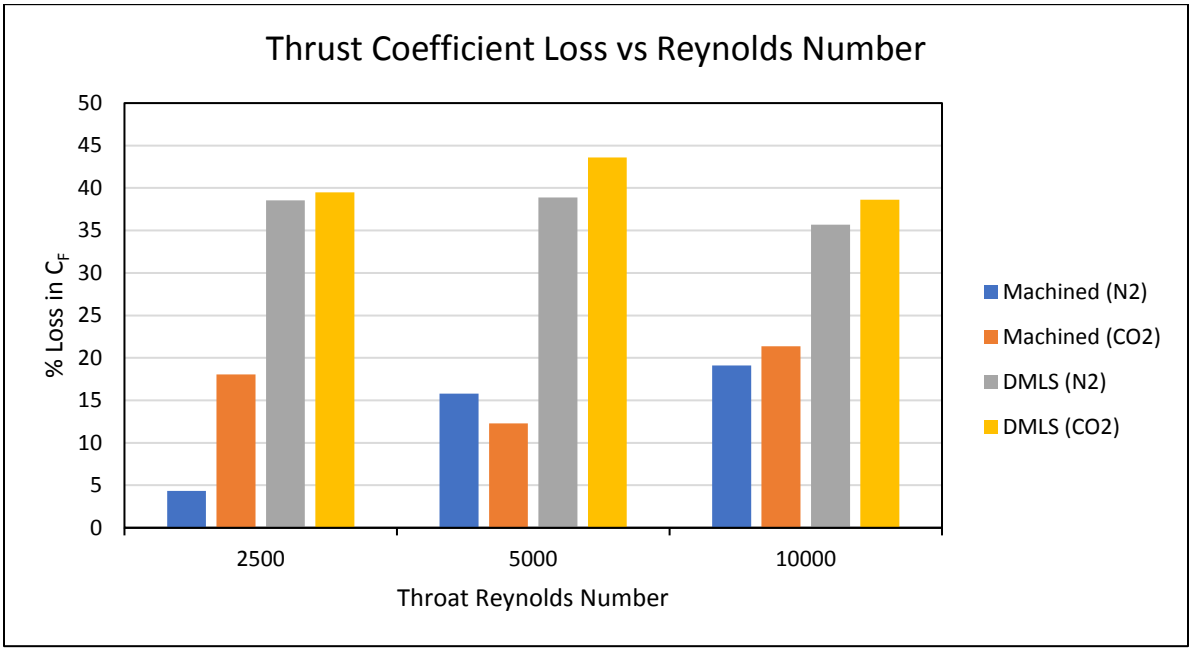

Figure 42: Machined vs DMLS Nozzle Performance Comparison

4.4.2 Effects of Reynolds Number and Expansion Ratio on Performance Losses

While the analytic model predicted very little difference in performance between the DMLS and machined nozzles, it did predict a distinct correlation between expansion ratio and losses as shown in Section 4.2. Additionally, the analytic model predicted distinct behavior between throat Reynolds number flow above and below 1000. At throat Reynolds numbers of 2500 and above, the analytic model predicted little correlation between Reynolds number and performance losses under the experimental conditions evaluated.

To evaluate these analytic expectations against the experimental results, Figure 43 plots the thrust coefficient loss against expansion ratio for all experimental data collected

for DMLS nozzles with the 0.015-in nominal throat diameter. These losses are calculated with respect to the isentropic expectations for the specific gas used for each test case. Error bars have been omitted from this plot to aid in visualization.

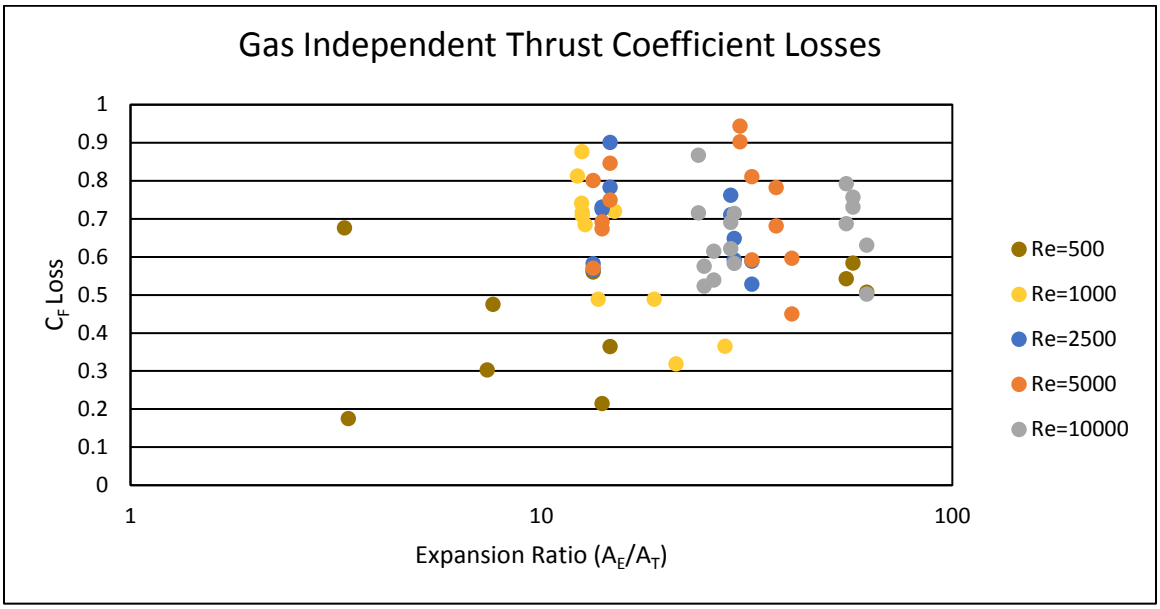

Figure 43: Thrust Coefficient Losses in Small Throat DMLS Nozzles

First, it is clear in Figure 43 that there is very little correlation between Reynolds number and loss in thrust coefficient over the entire range from 500 to 10000. Although the analytic model predicted this for Reynolds numbers above 2500, it was expected that distinct behavior would be noticeable between tests at throat Reynolds numbers above and below 1000.

Second, there is not a distinguishable trend between expansion ratio and loss in thrust coefficient at any Reynolds number. The analytic model predicts a decrease in loss until reaching an optimal expansion ratio before increasing. Admittedly, apparatus and constraints limited the number of expansion ratios tested at each Reynolds number. This

hampers the ability to draw strong conclusions from the experimental data regarding the effects of expansion ratio on thrust coefficient losses.

4.4.3 Causes of Inconsistency Between Experimental and Analytic Results

The previous sections of this chapter have shown that calculation of performance losses utilizing a model based upon one-dimensional, adiabatic compressible flow with viscous losses is insufficient in predicting the magnitude of losses observed in an experimental setting. Furthermore, the analytic model fails to predict the substantial difference between losses in DMLS and machined nozzles. At the same time, results have shown that the analytic model attributes unrealistic correlations between performance loss and both expansion ratio and Reynolds number.

It has been acknowledged that, by utilizing traditional methods of determining absolute roughness, the roughness used in the analytic model provides little distinction between the DMLS and machined nozzles. Therefore, the analytic model underestimates the performance differences between the two nozzle varieties. Returning to the research of Krishnamurty, it is likely that traditional absolute roughness simplifications are insufficient in determining the true effects of roughness in nozzles of this size [15].

Anomalous structures observed in the three-dimensional mapping of sectioned nozzles exhibited extremely variable and localized differences in maximum roughness height. Furthermore, these anomalous protrusions reached heights significant in comparison to the hydraulic diameters of various axial locations within the nozzles. Therefore, in accordance with Krishnamurty's research it is likely that additional loss mechanisms such as turbulent vortices creating drag at the tips of the protrusions and reflection of shock waves within the nozzle are contributing additional loss terms [15].

The propagation of these loss mechanisms in experimental nozzles helps to explain the large difference in performance losses observed between the DMLS and machined nozzles despite nearly identical average surface roughness. Although losses in the machined nozzles are not predicted perfectly by the analytic model, they are much closer than the predictions for the DMLS nozzles as shown in Figure 42. Imaging of the machined nozzle also showed far fewer anomalous protrusions, and those present were of lower heights than those observed in the DMLS nozzles. Therefore, it is expected that the losses caused by these protrusions would be much higher in the DMLS nozzles. Experimental results support this conclusion.

The presence of drag and shock reflection within the nozzle would certainly lead to inaccurate performance loss predictions by the analytic model used in this research. Furthermore, this would help to explain the relative independence of performance losses with respect to Reynolds number and expansion ratio. Because both drag and shock wave reflections will be highly dependent on the number of protrusions present in any nozzle, it is difficult to model this behavior as a function of any one Reynolds number or expansion ratio.

V. Conclusions

This chapter concludes this body of work and evaluates the effectiveness of this research in accomplishing the objectives laid out in Chapter 1. An analytic model was designed and used to estimate the impacts of surface roughness on the thrust coefficient of micro-nozzles by incorporating viscous losses in one-dimensional, adiabatic flow through a converging-diverging nozzle. This research assumed that viscous losses would be the dominant loss terms in additively manufactured and machined micro-nozzles. An experiment was then conducted to test 32 nozzles of varying geometry and surface roughness to evaluate the accuracy of the analytic model's predictions and the assumptions guiding its design.

5.1 Summary of Research Objectives

First, it is necessary to re-state the original objectives of this research as laid out in Chapter 1. These objectives are listed below:

1. Experimentally measure thrust and stagnation pressure of additively manufactured and machined micro-nozzles, with controlled mass flow.

2. Calculate thrust coefficients of both nozzle configurations using experimental measurements.

3. Develop an analytic model to predict the effects of surface roughness on viscous losses during thruster operation.

4. Compare experimental results to the analytic model to determine whether traditional viscous loss theory alone can accurately predict performance losses in machined and DMLS nozzles.

5. Compare thrust coefficients of additively manufactured nozzles against those of the machined nozzles to quantify performance impacts caused by surface roughness.

The first two objectives were met during the experimental phase of this research. An experiment was conducted to measure the thrust and stagnation pressure of two machined and 30 additively manufactured micro-nozzles of varying throat and exit area configurations. Tests were conducted to target throat Reynolds numbers between 500 and 10000. The thrust and pressure data collected was then used to calculate an experimental thrust coefficient and thrust coefficient loss when compared to isentropic expectations for each nozzle test. The final objective was also met during this stage of the research. Tests were designed to allow for comparison between the performance of machined and DMLS nozzles of similar geometries at similar conditions. Doing so allowed for the evaluation of the impact of surface roughness on nozzle performance.

The third objective was met by designing an analytic model in MATLAB to incorporate viscous losses in one-dimensional adiabatic compressible flow using the methods of Oosthuizen and Carscallen [19]. Although this was a departure from Spisz's methodology, using this method allowed for the inclusion of nozzle surface roughness in the calculation of the viscous loss term [4]. Objective four was met by running the analytic model at conditions approximating those of the experimental conditions and calculating the associated thrust coefficient and thrust coefficient loss predictions.

5.2 Summary of Results

Comparison of experimental and analytical results leads to the following conclusions. First, the analytic model consistently overpredicted the experimentally measured thrust coefficients for the DMLS and machined nozzles. However, the model was much closer in the case of the machined nozzles. This was likely caused in part by

the absolute roughness values used for the DMLS and machined nozzles in the analytic model being nearly indistinguishable from one another.

Roughness measurements showed that the average roughness of both nozzle varieties was nearly the same although the maximum roughness height of anomalous protrusions in the DMLS nozzles was significantly higher than the maximum height of irregularities in the machined nozzles. The analytic model's inability to account for this difference likely contributed to its ineffectuality in estimating losses in the DMLS nozzles. Experimental results confirmed a disparity in performance between the nozzle types. The average thrust coefficient losses were 24% higher in DMLS nozzles than in EDM nozzles.

Experimental results showed very little correlation between throat Reynolds number, expansion ratio and performance losses. This is likely because of the effects of turbulence, drag and shock reflection within the nozzles [15]. The presence of these loss terms would make performance loss predictions based upon Reynolds number and expansion ratio difficult to quantify because they would be highly specific to the roughness profile of each nozzle. Additionally, because the analytic model does not account for these loss terms, this explains the disparity between the analytic model and experimental results.

5.3 Future Work

The results of this research suggest that there are multiple avenues for future research in this subject area. First, it is acknowledged that the analytic model used in this research oversimplifies the dynamics of compressible flow through micro-nozzles with

significant variation in roughness profile. A computational fluid dynamics approach is likely necessary to properly investigate the presence of additional turbulent phenomena in compressible flow through micronozzles. Specifically, it is suggested that the roughness profile of DMLS nozzles be treated as individual protrusions into the flow and that the effects of drag and shock wave reflection be investigated.

Second, there is room to improve upon the experimental investigation undertaken in this research. First, improvement of the vacuum chamber or pump to eliminate the effects of pump vibration on thrust measurement and to allow for pumping to a lower vacuum pressure would increase the range of flow options available. Additionally, modifying the heater block to heat gas to higher temperatures would increase the range of expansion ratios and geometries that may be studied without the risk of saturation of the propellant gas.

The experimental procedure may also be modified to evaluate the theory that drag and shock wave reflection contribute significantly to performance loss. Because the supersonic flow in the divergent section of the nozzle will produce the combined shock wave and drag effects, post-processing to smooth the exit cone could be accomplished without significant increase in cost and schedule in the production of the nozzles. Additionally, appropriate scaling of the flow conditions and nozzle dimensions may allow for the use of optical methods, such as a Schlieren system, to directly observe gas density changes induced by these effects in the nozzle exit cone.

5.4 Final Conclusions

Additive manufacturing of micro-nozzles for low thrust applications allows for significant cost and schedule flexibility. However, additional research remains to be performed to accurately quantify the performance impacts associated with supersonic compressible flow through micro-nozzles exhibiting similar roughness profiles. Post-processing of the nozzle surface may significantly reduce performance losses but must be verified experimentally. Investigation of the exact mechanisms and dynamics causing these losses will require the use of computational fluid dynamics.

Appendix A. Nozzle Diameter and Roughness Measurements

Table 11: DMLS Nozzle Measurements

Nozzle Name	Throat a (in)	Throat b (in)	Throat Area (in^2)	Exit a (in)	Exit b (in)	Exit Area (in^2)	ε
15_5_1	0.0151	0.0146	0.000173	0.0338	0.0338	0.00090	5.2
15_5_2	0.0187	0.0187	0.000275	0.0343	0.0338	0.00091	3.3
15_5_3	0.0177	0.0182	0.000253	0.0323	0.0338	0.00086	3.4
15_10_1	0.0177	0.0167	0.000232	0.048	0.048	0.00181	7.8
15_10_2	0.0177	0.0172	0.000239	0.0474	0.0474	0.00176	7.4
15_10_3	0.0162	0.0167	0.000212	0.0449	0.0459	0.00162	7.6
15_20_1	0.0177	0.0182	0.000253	0.0651	0.0661	0.00338	13.4
15_20_2	0.0172	0.0177	0.000239	0.0666	0.0671	0.00351	14.7
15_20_3	0.0192	0.0172	0.000259	0.0676	0.0686	0.00364	14.0
15_30_1	0.0167	0.0172	0.000226	0.0826	0.0838	0.00544	24.1
15_30_2	0.0162	0.0162	0.000206	0.0838	0.0823	0.00542	26.3
15_30_3	0.0162	0.0172	0.000219	0.0833	0.0833	0.00545	24.9
15_40_1	0.0162	0.0172	0.000219	0.0954	0.0949	0.00711	32.5
15_40_2	0.0177	0.0177	0.000246	0.0944	0.0959	0.00711	28.9
15_40_3	0.0182	0.0167	0.000239	0.0944	0.0949	0.00704	29.5
15_50_1	0.0202	0.0182	0.000289	0.106	0.1055	0.00878	30.4

15_50_2	0.0177	0.0177	0.000246	0.1075	0.1085	0.00916	37.2
15_50_3	0.0162	0.0172	0.000219	0.107	0.106	0.00891	40.7
15_80_1	0.0182	0.0177	0.000253	0.1358	0.1358	0.01448	57.2
15_80_2	0.0192	0.0172	0.000259	0.1343	0.1358	0.01432	55.2
15_80_3	0.0177	0.0167	0.000232	0.1353	0.1353	0.01438	61.9
30_20_1	0.0353	0.0338	0.000937	0.1358	0.1348	0.01438	15.3
30_20_2	0.0343	0.0338	0.000911	0.1368	0.1363	0.01464	16.1
30_20_3	0.0343	0.0353	0.000951	0.1358	0.1353	0.01443	15.2
30_30_1	0.0343	0.0343	0.000924	0.1656	0.1656	0.02154	23.3
30_30_2	0.0338	0.0338	0.000897	0.1645	0.1661	0.02146	23.9
30_30_3	0.0343	0.0338	0.000911	0.1656	0.1656	0.02154	23.7
30_40_1	0.0343	0.0348	0.000937	0.1918	0.1908	0.02874	30.7
30_40_2	0.0348	0.0353	0.000965	0.1933	0.1928	0.02927	30.3
30_40_3	0.0333	0.0338	0.000884	0.1933	0.1913	0.02904	32.9
30_50_1	0.0313	0.0308	0.000757	0.216	0.215	0.03647	48.2
30_50_2	0.0333	0.0313	0.000819	0.215	0.2135	0.03605	44.0
30_50_3	0.0348	0.0318	0.000869	0.216	0.215	0.03647	42.0
30_100_1	0.0343	0.0343	0.000924	0.3044	0.3034	0.07254	78.5
30_100_2	0.0343	0.0353	0.000951	0.3044	0.3034	0.07254	76.3
30_100_3	0.0353	0.0338	0.000937	0.3028	0.3023	0.07189	76.7

Table 12: EDM Nozzle Measurements

Nozzle Name	Throat a (in)	Throat b (in)	Throat Area (in^2)	Exit a (in)	Exit b (in)	Exit Area (in^2)	ε
M15_20	0.0217	0.0227	0.000387	0.0656	0.0661	0.003406	8.8
M15_40	0.0227	0.0237	0.000423	0.0914	0.0924	0.006633	15.7

Table 13: Nozzle Roughness Measurements

Nozzle	D30_50	
Section	**Average Roughness (µm)**	**S_z (µm)**
Chamber	7.29	109.13
Convergent	11.37	156.29
Throat	7.68	101.98
Divergent	10.14	149.13
Total	9.12	129.1325
Nozzle	M30_100	
Section	**Average Roughness (µm)**	**S_z (µm)**
Area 1	6.12	60.58
Area 2	6.45	72.25
Total	6.285	66.415
Nozzle	D30_100	
Section	**Average Roughness (µm)**	**S_z (µm)**
Chamber	7.49	102.05
Convergent	4.45	66.69
Throat	4.18	50.76
Divergent 1	3.75	57.2
Divergent 2	7.99	102.75
Total	5.572	75.89

Appendix B. Analytic Model Graphs

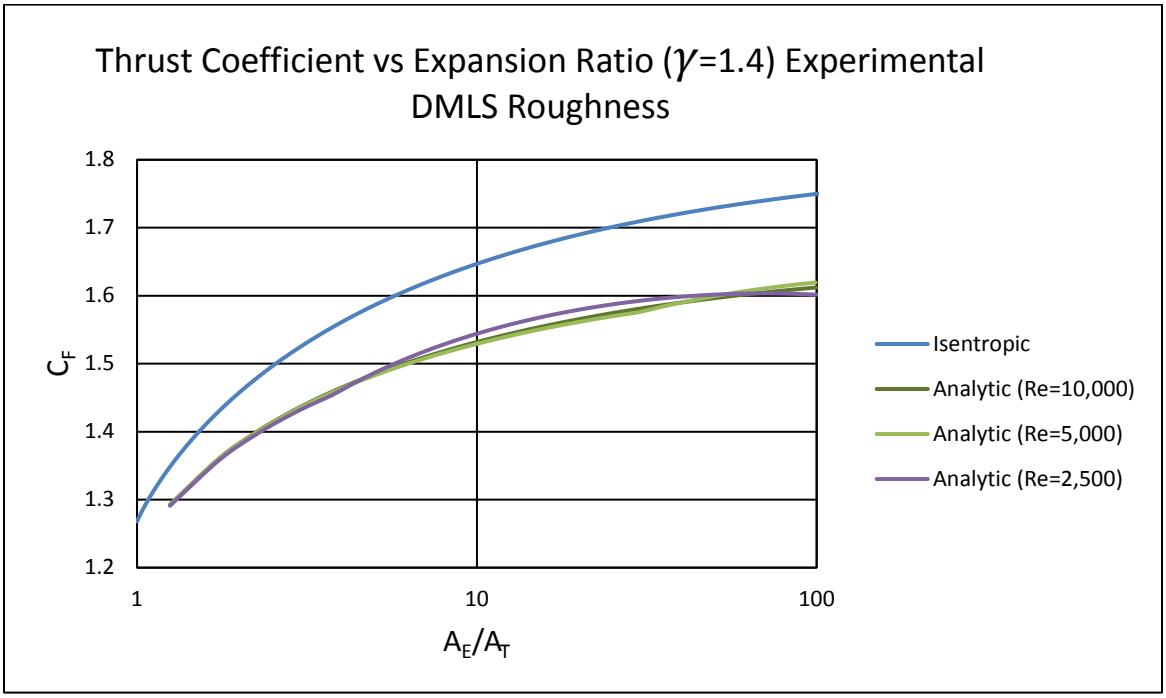

Figure 44: C_F in 0.017-in Throat Diameter Nozzle (Nitrogen)

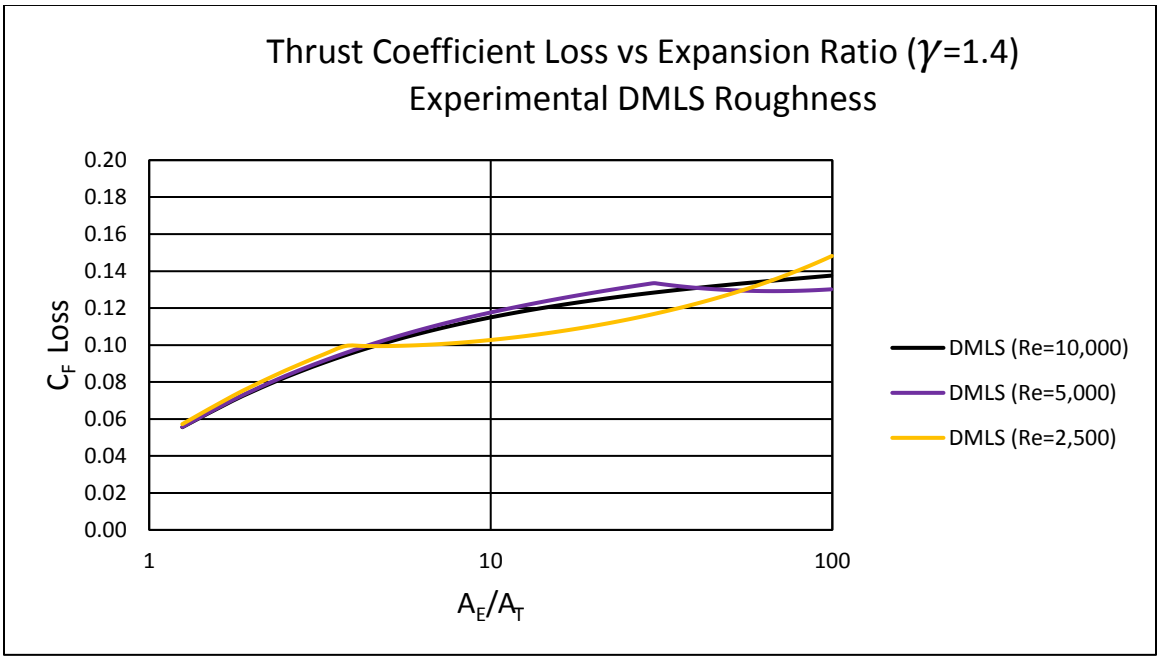

Figure 45: C_F Loss in 0.017-in Throat Diameter Nozzle (Nitrogen)

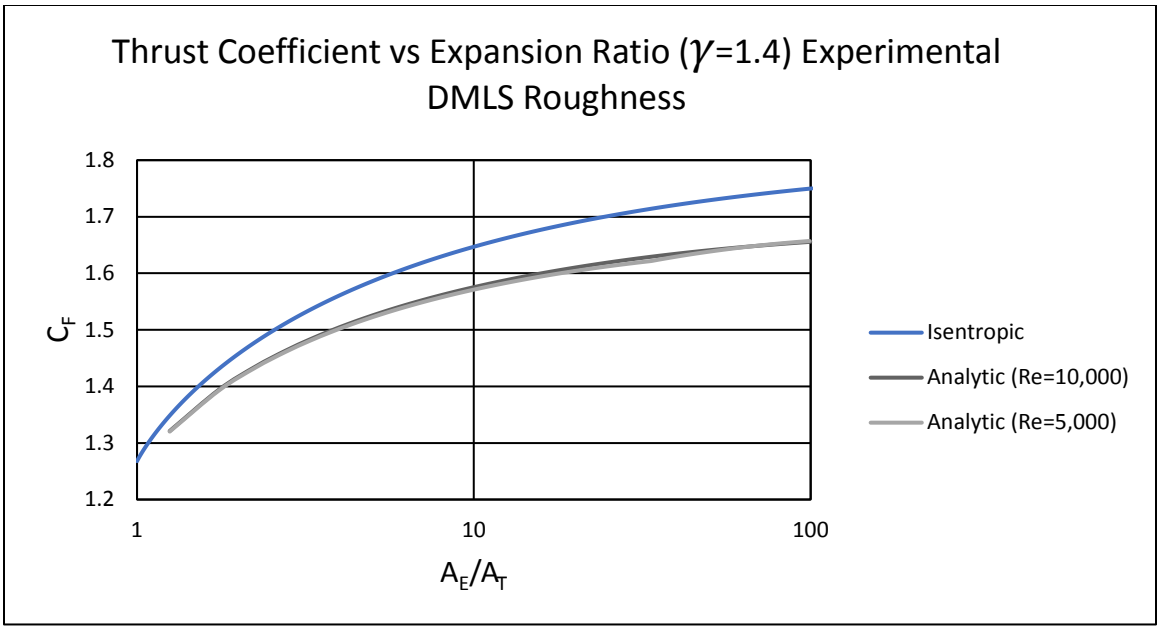

Figure 46: C_F in 0.034-in Throat Diameter Nozzle (Nitrogen)

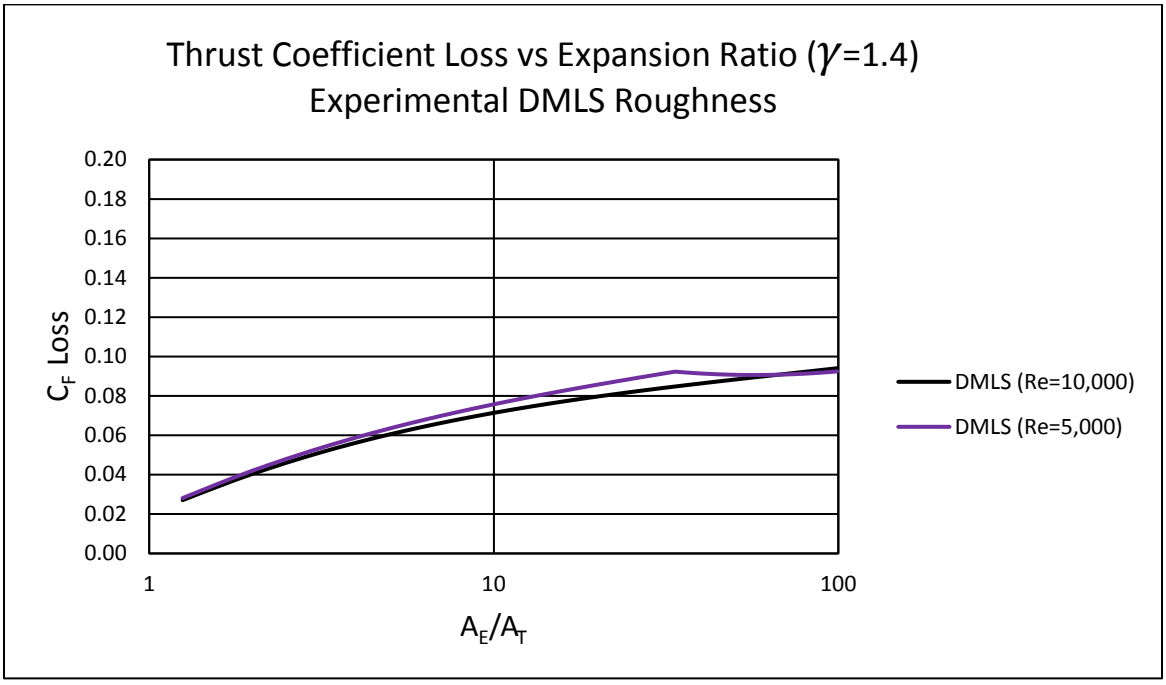

Figure 47: C_F Loss in 0.034-in Throat Diameter Nozzle (Nitrogen)

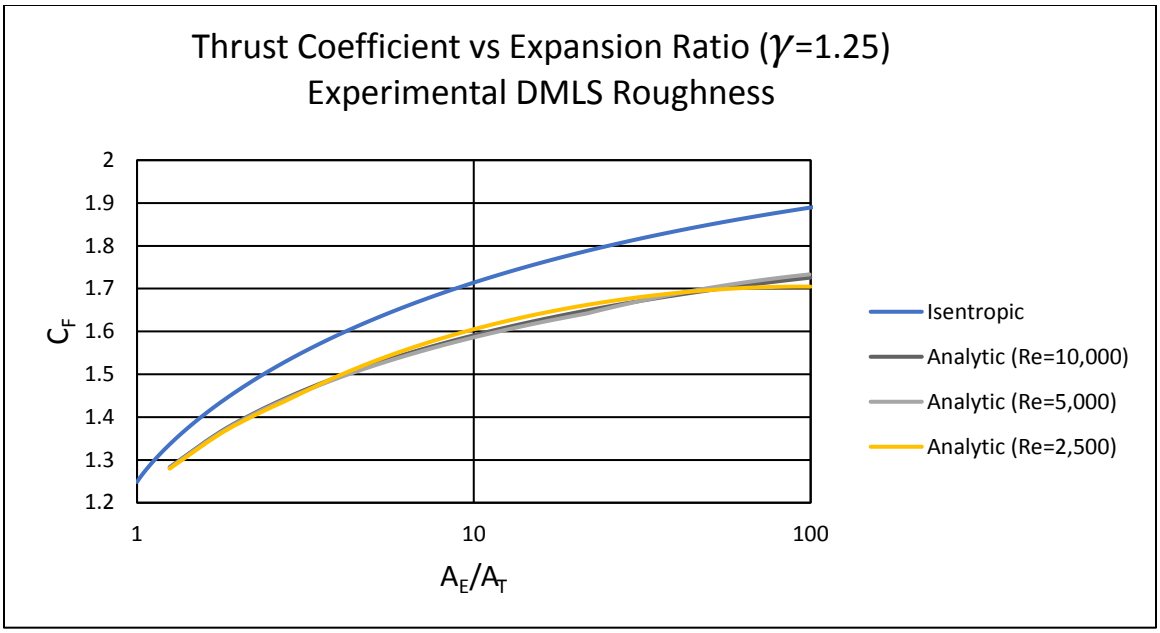

Figure 48: C_F in 0.017-in Throat Diameter Nozzle (Carbon Dioxide)

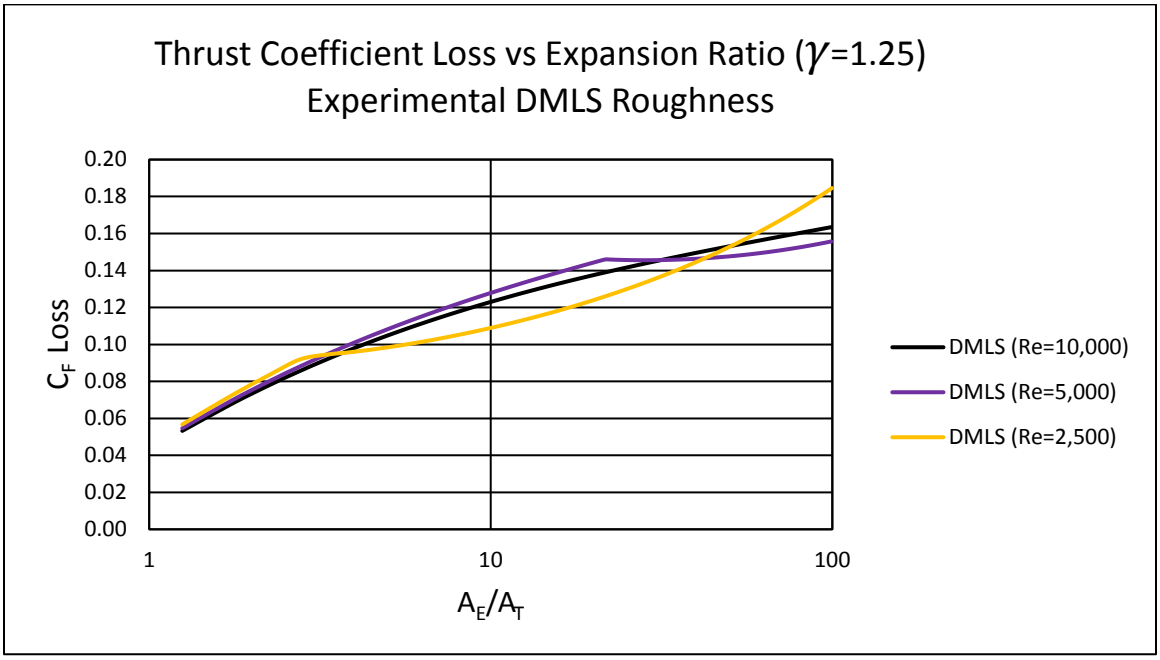

Figure 49: C_F Loss in 0.017-in Throat Diameter Nozzle (Carbon Dioxide)

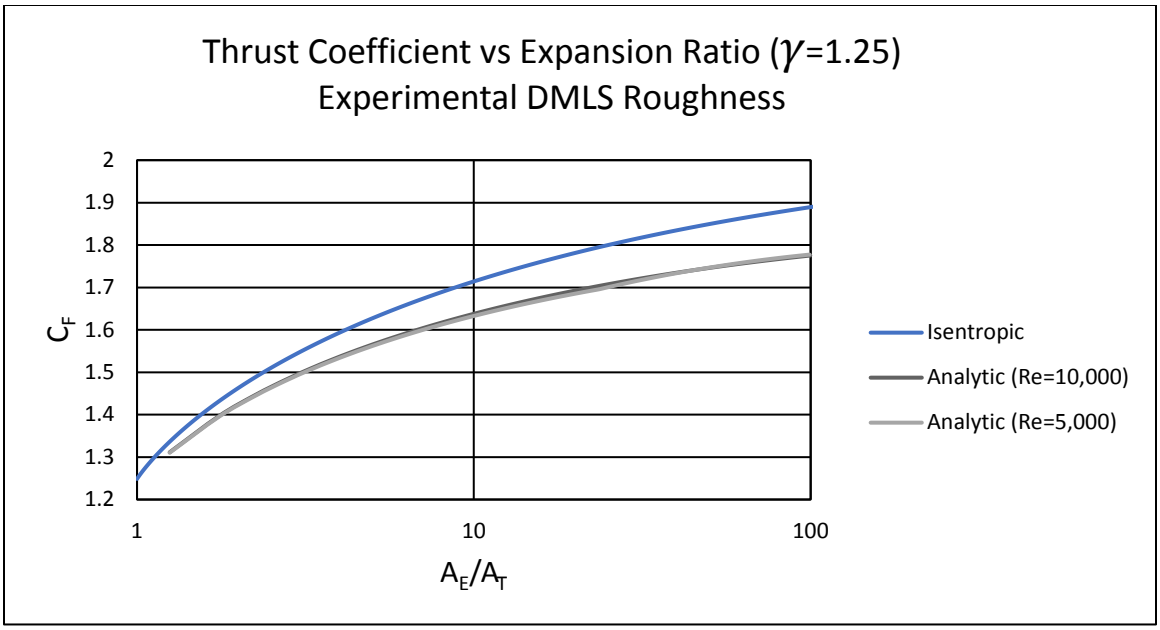

Figure 50: C_F in 0.034-in Throat Diameter Nozzle (Carbon Dioxide)

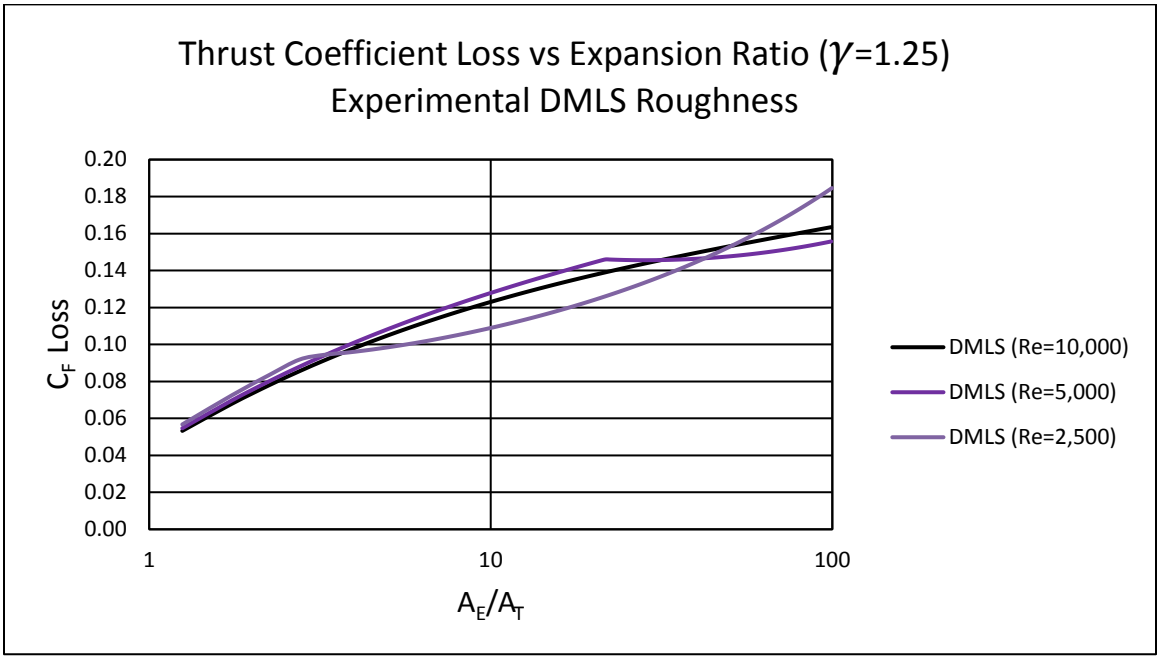

Figure 51: C_F Loss in 0.034-in Throat Diameter Nozzle (Carbon Dioxide)

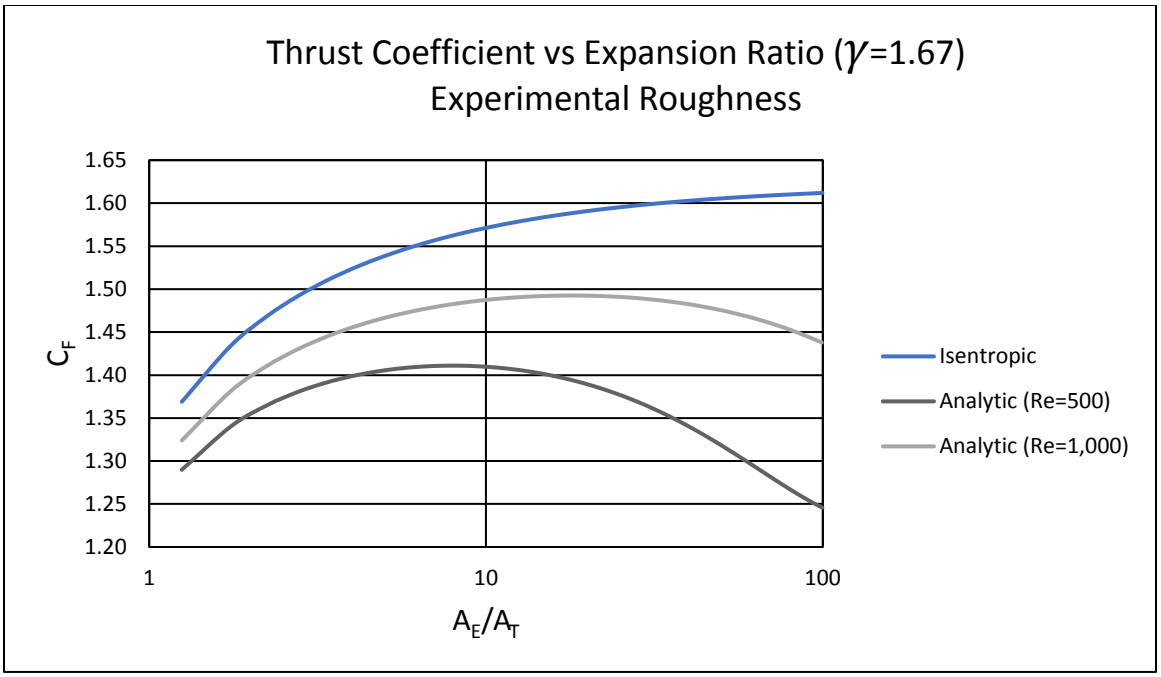

Figure 52: C_F in 0.017-in Throat Diameter Nozzle (Helium)

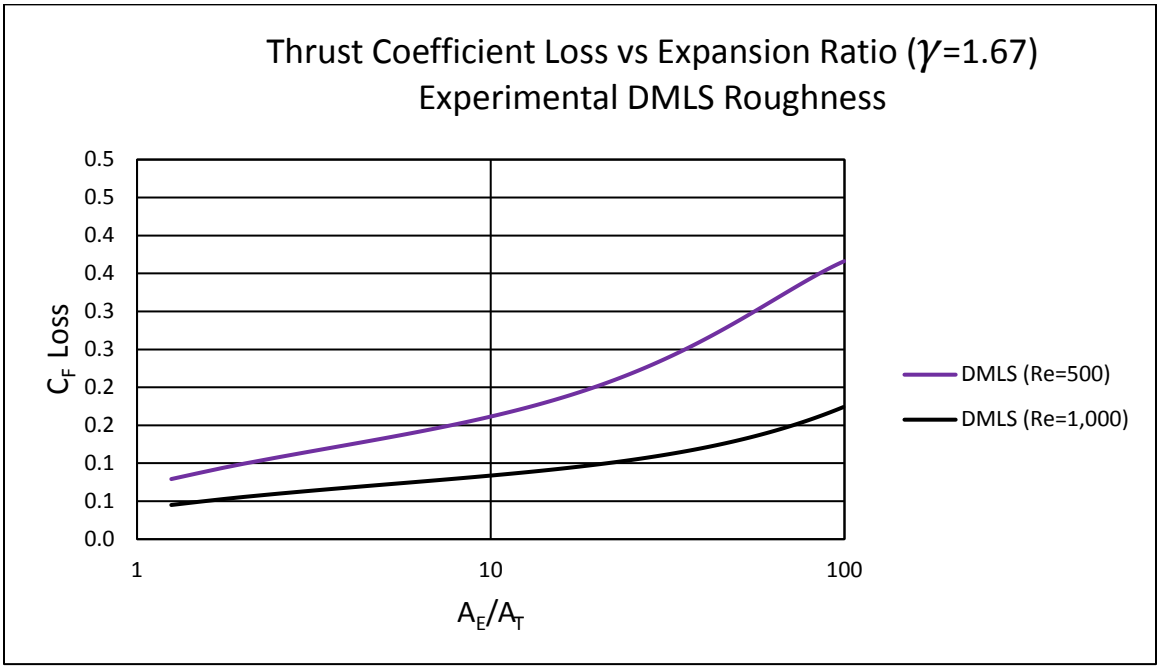

Figure 53: C_F Loss in 0.017-in Throat Diameter Nozzle (Helium)

Appendix C. Experimental Result Graphs

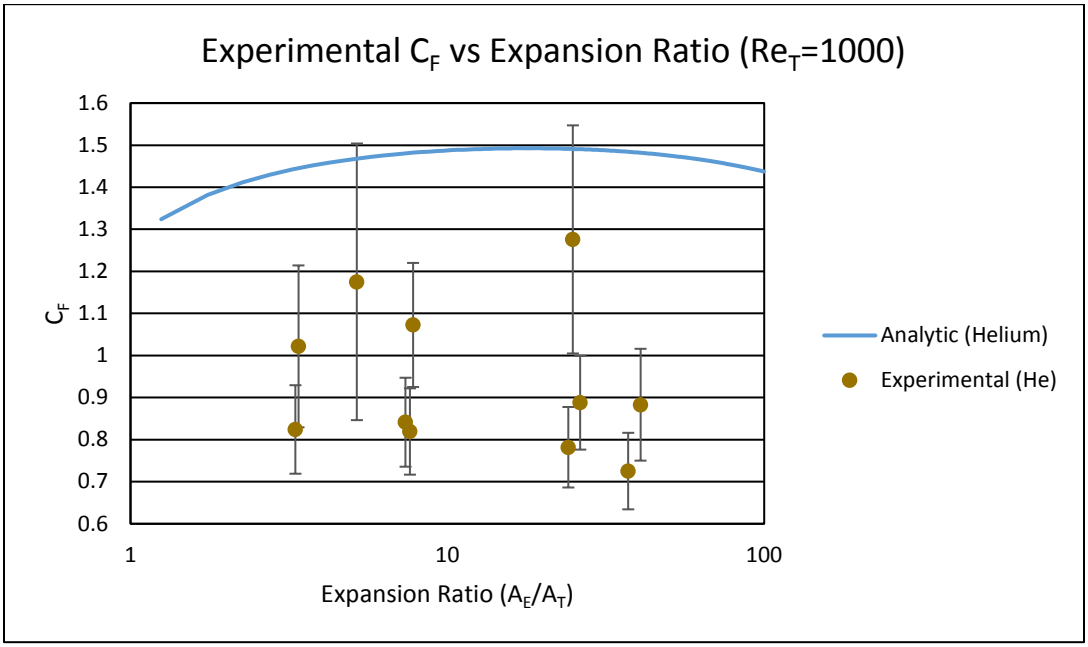

Figure 54: Re=1000 Experimental C_F

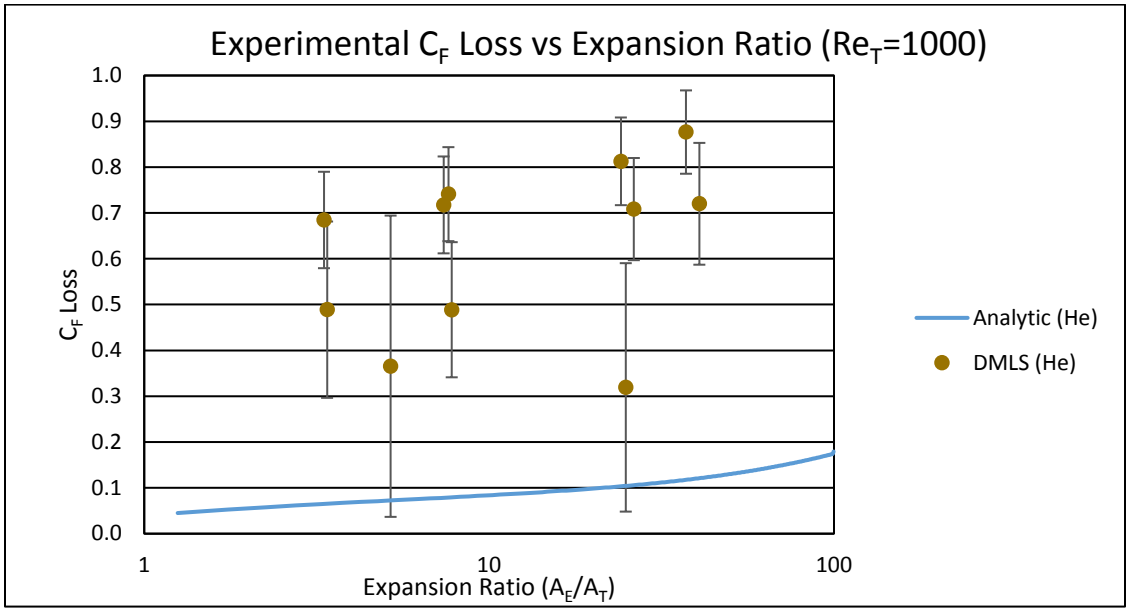

Figure 55: Re=1000 Experimental C_F Loss

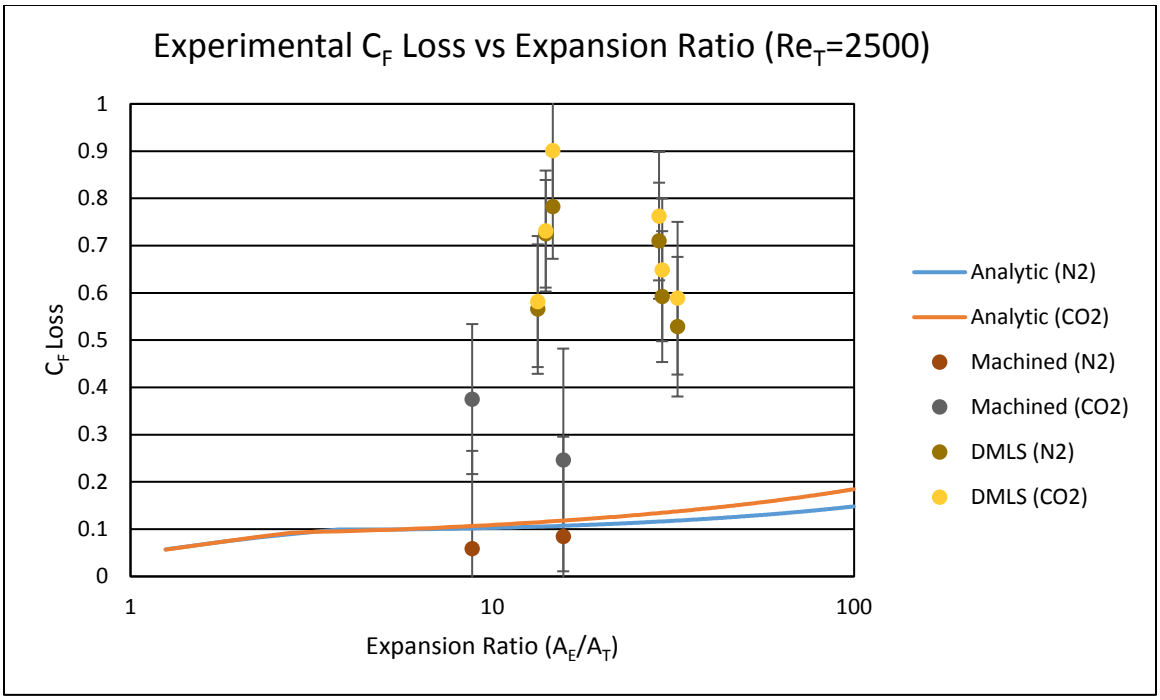

Figure 56: Re=2500 Experimental CF Loss

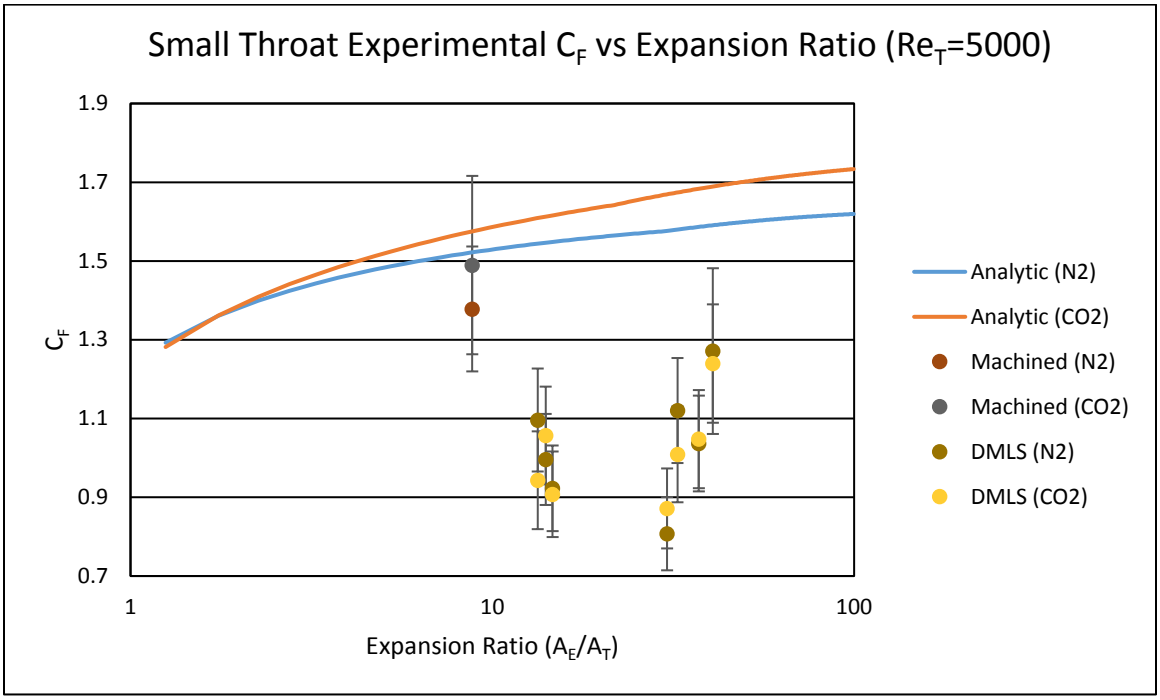

Figure 57: Re=5000 Experimental C_F (Small Throat)

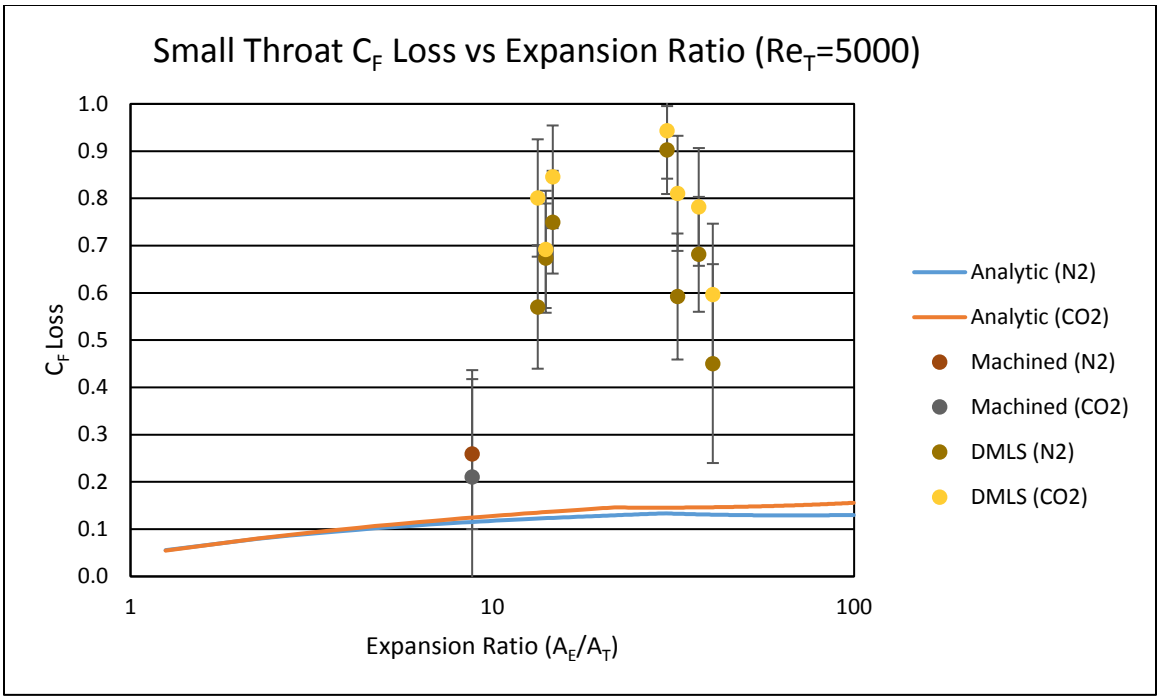

Figure 58: Re=5000 Experimental C_F Loss (Small Throat)

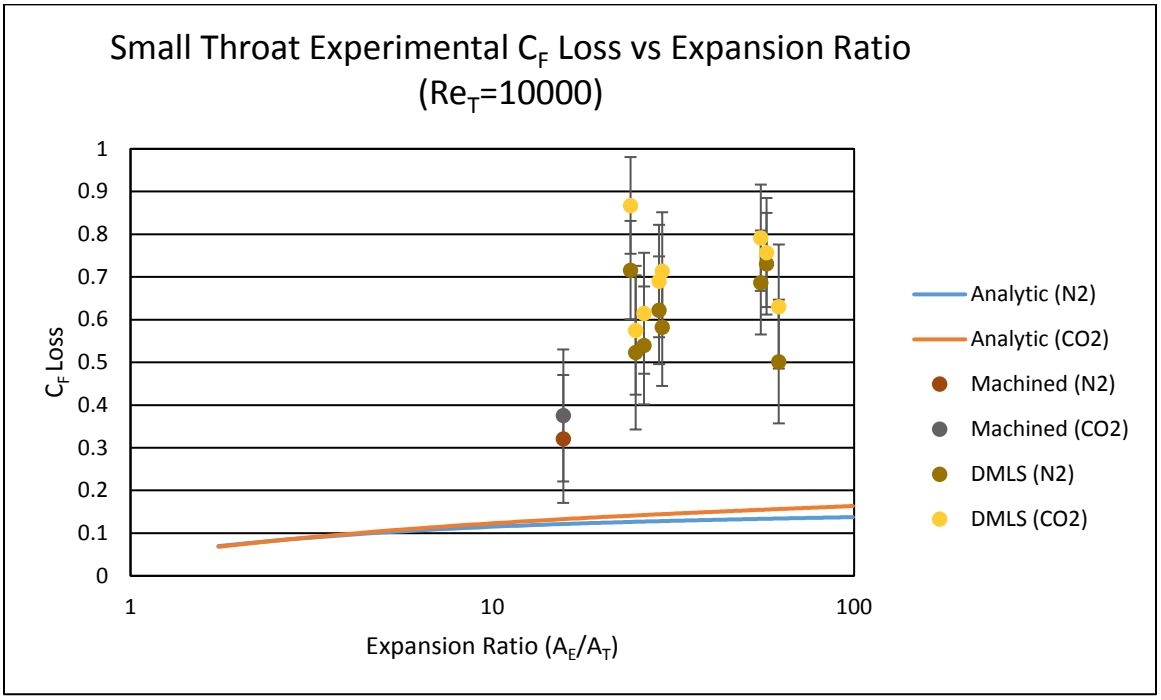

Figure 59: Re=10000 Experimental C_F Loss (Small Throat)

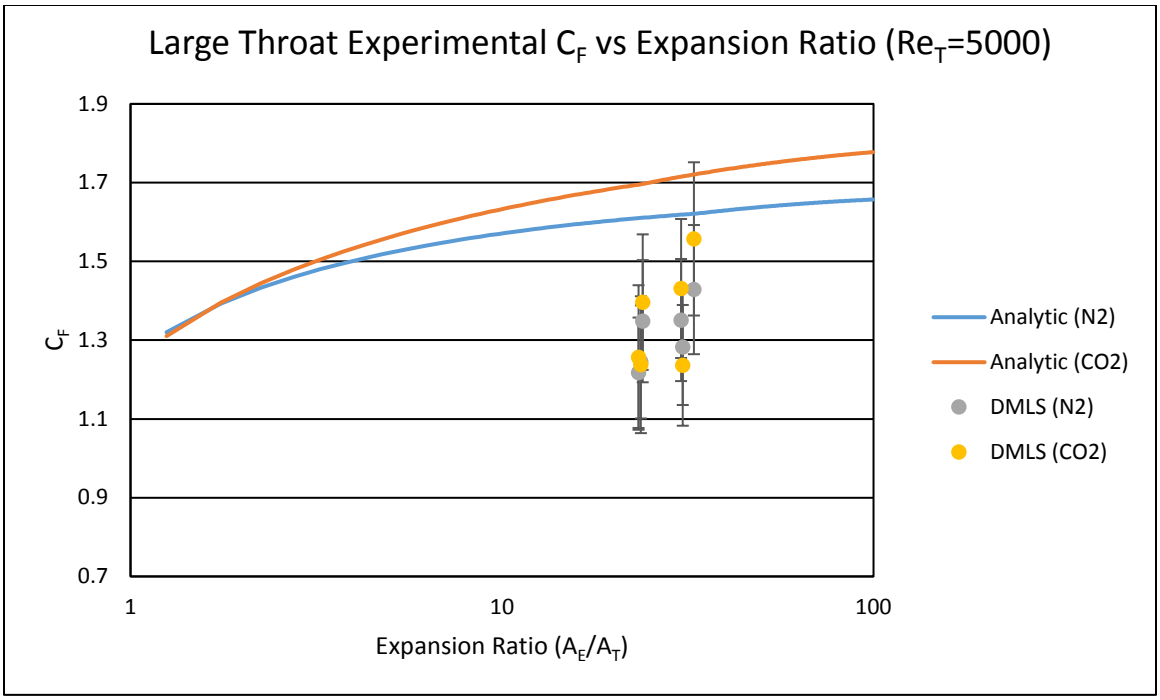

Figure 60: Re=5000 Experimental C_F (Large Throat)

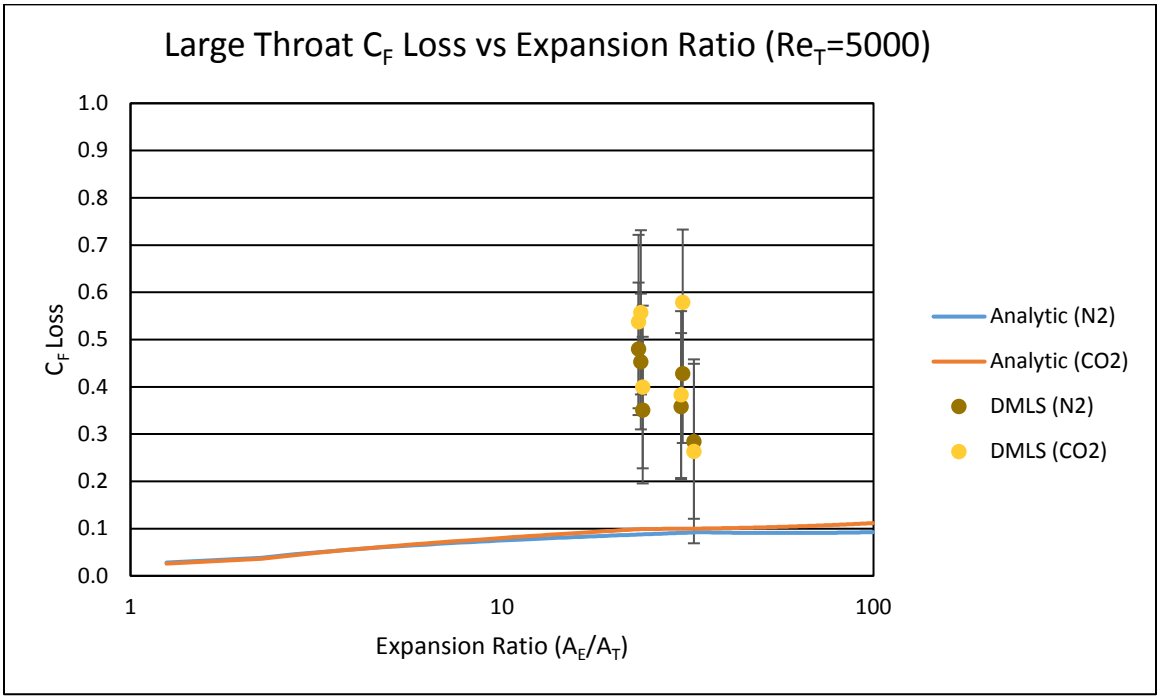

Figure 61: Re=5000 Experimental C_F Loss (Large Throat)

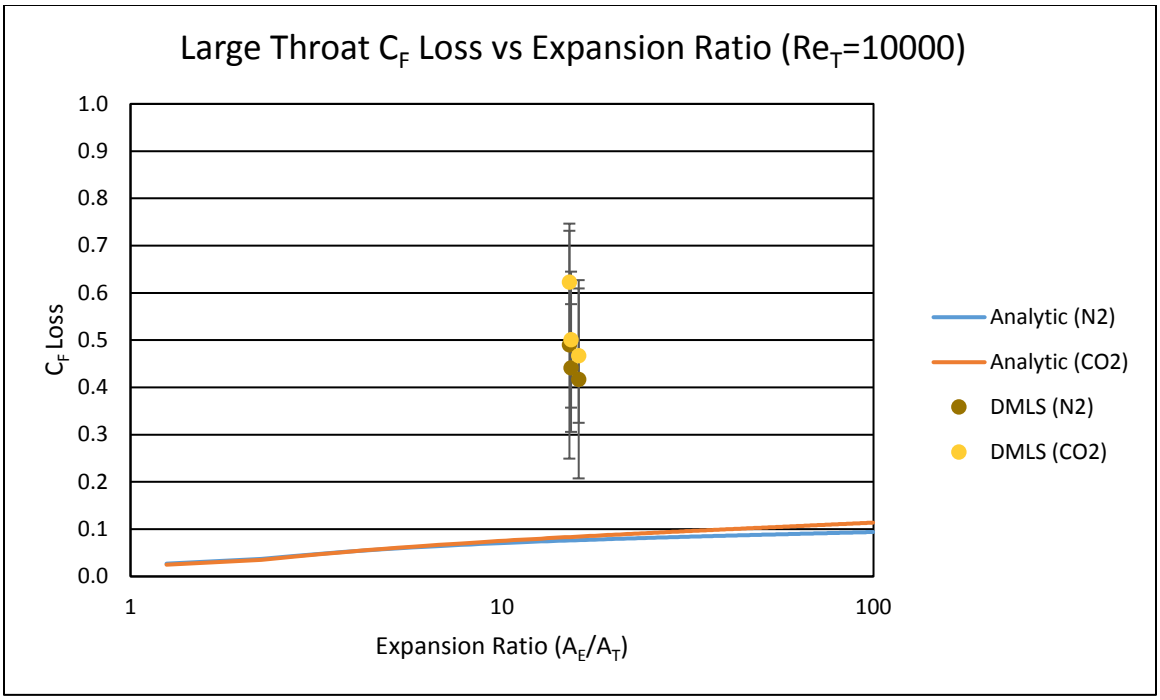

Figure 62: Re=10000 Experimental C_F Loss (Large Throat)

Bibliography

[1] A. D. Ketsdever and J. Miller, "Systems considerations and design options for microspacecraft propulsion systems," in *35th AIAA/ASME/SAE/ASEE Joint Propulsion Conference and Exhibit*, Los Angeles, CA, 1999.

[2] G. P. Sutton and O. Biblarz, Rocket Propulsion Elements, 8th ed., Hoboken, NJ: John Wiley and Sons, Inc., 2010.

[3] C. Murch et al., "Low-thrust nozzle performance," in *6th Aerospace Sciences Meeting*, New York, NY, 1968.

[4] E. W. Spisz et al., "Thrust coefficients of low-thrust nozzles," NASA, Cleveland, OH, TN D-3056,1965.

[5] S. P. Grisnik et al., "Experimental study of low Reynolds number nozzles," NASA, Cleveland, OH, NASA-TM-89858, 1987.

[6] M. V. Whalen, "Low Reynolds number nozzle flow study," NASA, Cleveland, OH, NASA-TM-100130, 1987.

[7] J. Lind et al., "Rapid manufacturing with direct metal laser sintering," in *Materials Research Society Symposium*, Boston, MA, 2002.

[8] W. M. Marshall et al., "Using additive manufacturing to print a CubeSat propulsion system," in *51st AIAA/SAE/ASEE Joint Propulsion Conference, Propulsion and Energy Forum*, Orlando, FL, 2015.

[9] N. Gimelshein et al., "Surface roughness effects in low Reynolds number channel flows," in *25th International Symposium on Rarefied Gas Dynamics*, Saint-Petersburg, Russia, 2006.

[10] J. S. Sovey et al., "Vacuum chamber pressure effects on thrust measurements of low Reynolds number nozzles," NASA, Cleveland, OH, NASA-TM-86955, 1985.

[11] P. H. Oosthuizen and W. E. Carscallen, Compressible Fluid Flow, Graphics Press, 1997.

[12] M. F. Osborn et al., "Overcoming low nozzle efficiency: a test-correlated numerical investigation of low reynolds number micro-nozzle flow," in *51st AIAA/SAE/ASEE Joint Propulsion Conference*, Orlando, FL, 2015.

[13] M. J. Moran and H. N. Shapiro, Fundamentals of Engineering Thermodynamics, 6th ed., Hoboken, NJ: John Wiley and Sons, Inc., 2008, p. 48 & 53.

[14] J. C. Williams III, "Viscous compressible and incompressible flow in slender channels," *AIAA Journal,* vol. 1, no. 1, pp. 186-195, 1962.

[15] V. S. Krishnamurty, et al., "Effect of wall roughness on the flow through converging-diverging nozzles," in *35th AIAA Aerospace Sciences Meeting and Exhibit* , Reno, NV, 1997.

[16] C. P. Jones et al., "Additive manufacturing a liquid hydrogen rocket engine," NASA Marshall Space Flight Center, Huntsville, AL, 2012.

[17] B. R. McKinght et al., "Design and testing of an additively manufactured advanced hybrid rocket motor propulsion unit for CubeSats (PUC)," in *51st AIAA/SAE/ASEE Joint Propulsion Conference*, Orlando, FL, 2015.

[18] T. Zhang and C. M. Miyamoto, "3D printing: A cost effective and timely approach to manufacturing of low-thrust engines," in *50th AIAA/ASME/SAE/ASEE Joint Propulsion Conference*, Cleveland, OH, 2014.

[19] P. H. Oosthuizen and W. E. Carscallen, Introduction to compressible fluid flow, Boca Raton, FL: Taylor and Francis Group, LLC, 2014.

[20] L. Shampine and M. Reichelt, "The MATLAB ODE Suite," *SIAM Journal on Scientific Computing,* vol. 18, pp. 1-22, 1997.

[21] F. P. Incropera and D. P. DeWitt, Fundamentals of Heat and Mass Transfer, New York: J. Wiley, 2002.

[22] L. F. Moody, "Friction factors for pipe flow," *Transactions of the A.S.M.E,* vol. 66, pp. 671-677, 1944.

[23] Haynes International Inc., *HAYNES 282 alloy data sheet.*

[24] Omega Engineering Inc., *FMA 5400/ FMA 5500 Mass Flow Controllers User's Guide*, Stamford, CT, 2001.

[25] Kurt J. Lesker Company, *Series 979 Atmosphere to Vacuum Transducer: Operation and Maintenance Manual*, Clairton, PA, 2003.

[26] A. J. Wheeler and A. R. Ganji, Introduction to Engineering Experimentation, Englewood Cliffs, NJ: Prentice-Hall Inc., 1996.

[27] T. G. Beckwith, R. D. Marangoni and J. H. Lienhard V, Engineering: ME310 Instrumentation and Theory of Experiments, Boston, MA: Pearson, 2011.

[28] Keyence, *Laser Scanning Microscope User Manual*, Japan, 2015.

[29] T. Adams, C. Grant and H. Watson, "A simple algorithm to relate measured surface roughness to equivalent sand-grain roughness," *International Journal of Mechanical Engineering and Mechatronics*, vol. 1, no. 1, pp. 66-71, 2012.

REPORT DOCUMENTATION PAGE

Form Approved
OMB No. 074-0188

PLEASE DO NOT RETURN YOUR FORM TO THE ABOVE ADDRESS.

1. REPORT DATE *(DD-MM-YYYY)*	**2. REPORT TYPE**	**3. DATES COVERED** *(From – To)*
23-03-2017	Master's Thesis	March 2016 – March 2017

TITLE AND SUBTITLE

PERFORMANCE LOSSES IN ADDITIVELY MANUFACTURED LOW THRUST NOZZLES

5a. CONTRACT NUMBER

5b. GRANT NUMBER

5c. PROGRAM ELEMENT NUMBER

6. AUTHOR(S)

Tommila, Christopher D., Captain, USAF

5d. PROJECT NUMBER

5e. TASK NUMBER

5f. WORK UNIT NUMBER

7. PERFORMING ORGANIZATION NAMES(S) AND ADDRESS(S)
Air Force Institute of Technology
Graduate School of Engineering and Management (AFIT/ENY)
2950 Hobson Way, Building 640
WPAFB OH 45433-8865

8. PERFORMING ORGANIZATION REPORT NUMBER

AFIT-ENY-MS-17-M-295

9. SPONSORING/MONITORING AGENCY NAME(S) AND ADDRESS(ES)
Intentionally left blank

10. SPONSOR/MONITOR'S ACRONYM(S)

11. SPONSOR/MONITOR'S REPORT NUMBER(S)

12. DISTRIBUTION/AVAILABILITY STATEMENT
DISTRUBTION STATEMENT A. APPROVED FOR PUBLIC RELEASE; DISTRIBUTION UNLIMITED.

13. SUPPLEMENTARY NOTES

14. ABSTRACT

The goal of this research is to evaluate, both analytically and experimentally, the suitability of additive manufacturing in the production of small scale thruster nozzles for low thrust orbital propulsion applications. Current high temperature metallic additive manufacturing processes, like Direct Metal Laser Sintering, typically result in untreated part surfaces with higher roughness than traditional machining processes. For large scale rocket applications, nozzle wall roughness, and the associated boundary layer effects, may safely be ignored. However, in nozzles with throat diameters on the order of ten-thousandths of an inch, any viscous effects originating at the nozzle walls must be considered.

It is likely that, even at the low flow Reynolds numbers exhibited in low thrust applications, the effects of viscous losses at the nozzle walls are affected by an increase in nozzle surface roughness. The first phase of this research focuses on the design and implementation of an analytic model to predict losses in thrust coefficient due to viscous effects. During the second phase, a variety of nozzle configurations are tested in a laboratory environment to determine the accuracy of the analytic model and to identify additional modes of performance loss associated with increased surface roughness.

15. SUBJECT TERMS					
16. SECURITY CLASSIFICATION OF:			**17. LIMITATION OF ABSTRACT**	**18. NUMBER OF PAGES**	**19a. NAME OF RESPONSIBLE PERSON** Dr. Carl Hartsfield, AFIT/ENY
a. REPORT	**b. ABSTRACT**	**c. THIS PAGE**			**19b. TELEPHONE NUMBER** *(Include area code)*
U	**U**	**U**	**UU**	128	(937) 785-3636, ext 4667 (carl.hartsfield@afit.edu)

Standard Form 298 (Rev. 8-98)
Prescribed by ANSI Std. Z39-18